Universitat de Barcelona

Customizing a low temperature system for microwave transmission measurements. Quantum transport in thin TiN films and Nanostructures

Carla Carbonell Cortés

Customizing a low temperature system for microwave transmission measurements. Quantum transport in thin TiN films and nanostructures

Carla Carbonell Cortés

Departament de Física Fonamental, Universitat de Barcelona
Programa: Nanociències

Thesis supervisors:
Antoni García Santiago and Joan Manel Hernàndez Ferràs

May 2012

Als meus pares,
per ser-hi sempre.

Πάντα ῥεῖ καὶ οὐδὲν μένει

(Tot flueix, res s'està quiet)

Heràclit d'Efes

Contents

Preface

Since the summer of 2004, after my second year exams I started prying around the lab of Grup de Magnetisme of Universitat de Barcelona. I knew immediately I will be doing a PhD in experimental research. Although my first interest had been in theoretical physics, as I went forward in the studies I saw it more and more clear.

When I finally got the chance of doing this thesis under the direction of Antoni García Santiago and Joan Manel Hernàndez the answer was obvious. The project was perfect because it combined a technical development with the experimental research.

The main aim of the first part of this thesis was to prove the development and improvement of a new equipment built to study magnetic and electrical properties, specially applying microwaves in reflection and transmission conditions. For this purpose different probes were designed, built and tested.

The second part consists of transport measurements of TiN thin films in order to prove the existence and observation of the superconductor-insulator transition and a new state of matter called superinsulator dual to superconductor.

Another extra value of this research project is the fact of working with two unusual measurement equipments. Most of the experimental research of our group is performed on a SQUID magnetometer so the possibility of measuring with a completely new cryostat and a dilution refrigerator that had been stopped for years was a very interesting challenge.

Agraïments

Agraïment: Acció d'agrair.

Agrair: Correspondre amb gratitud.

Gratitud: Sentiment afectuós que hom té envers el que li ha fet un bé, un servei o un favor.

Sempre he pensat que tenim el mal costum de donar poc les gràcies i fa temps que ho intento corregir, per allò que: "per canviar les coses algú ha de començar".

La cruïlla en què em trobo ara mateix és que si hagués de citar cada una de les persones a qui jo voldria mostrar el meu agraïment l'extensió de la Tesi es doblaria. Per tant, encara que no trobis el teu nom aquí escrit pots estar ben segur que hi és perquè pel simple fet d'estar llegint aquestes ratlles, d'alguna manera o altra, tu en formes part.

Gràcies, primer de tot, al Javier Tejada per obrir-me les portes del laboratori quan jo tot just acabava els meus exàmens de segon.

Gràcies al seu equip d'aleshores, Alberto, Anna, Roger, Ferran, Marta, per fer-me la millor rebuda possible.

Gràcies als meus directors, Antoni García Santiago i Joan Manel Hernàn-

dez, ja que sense la seva insistència, discussions i meticuloses correccions això encara seguiria a la carpeta de coses pendents.

Gràcies, thanks to Dr. Tatyana Baturina and Dr. Valerii Vinokour for introducing me to the world of superinsulators. Tatyana, for the samples, for your always good advice in what concerns experimental research and a warm reception in Novosibirsk with your team and family. To Valerii for sharing your interesting stories and experiences with me.

Gràcies als meus companys de despatx per la paciència amb les preguntes incoherents o amb els renecs quan el LaTeX feia de les seves.

Gràcies, en especial, a la Cris i al Gian pel seu suport incondicional i els ànims fos l'hora que fos i per la inestimable ajuda en la cerca d'articles aquests darrers dies.

Gràcies als meus pares, Xavi i Deli, per ser, segurament, els que més han aguantat els estirabots fruits dels nervis o el sentiment d'impotència d'alguns moments. Perquè no hi ha suport més sincer i important que aquell que et donen sense necessitar saber per què.

Gràcies a aquells que, durant aquests darrers anys, m'heu mostrat i acollit en un món nou. Jordi, Edu, Lali, David, Alfred, Àlex..., que en algun moment o altre m'heu donat el que necessitava rebre, que m'heu mostrat el que necessitava veure i que m'heu dit el que necessitava sentir.

Gràcies, JP, per donar-me un motiu. De vegades només cal saber cap on vols anar per trobar l'equilibri necessari per desencallar una situació i perseguir un objectiu amb tanta perseverància, tenacitat, audàcia i aplom com sigui possible, però sobretot, amb un bon sentit del ritme. Així, i només així, t'assegures arribar al premi final.

Gràcies, finalment, als meus estimats amics i companys d'aventures, Blues i K. Si es comptessin les hores que heu passat desperts per culpa de la Tesi aquestes últimes nits, n'hauríeu de ser coautors.

Que sigueu molts no us fa menys importants. Cadascun de vosaltres es mereixeria una o vàries pàgines per si sol. Això només em fa ser molt més afortunada.

Gràcies,
Carla
Barcelona, 30 d'abril del 2012

Part I

Customizing a low temperature system for microwave transmission measurements

Chapter 1

Introduction

The first years of my work focused on the development and improvement of a new equipment built to study magnetic and electrical properties, particularly applying microwaves in reflection and transmission conditions. The sample space in conventional cryostats with superconducting magnets is usually smaller than 10-mm-diameter. Our equipment consists of a hollow cylindrical cryostat having a 33-mm-diameter hole all along its vertical axis. [1] These characteristics enable the measurement of large samples and the use of big resonant cavities to get to a wider microwave (MW) range, particularly in transmission measurements.

The cryostat has a superconducting magnet made of a solenoid that applies a magnetic field from -5 T to 5 T, and a temperature controller that works in the range 1.8 - 300 K. The system is cooled down with nitrogen and helium and the temperature can be controlled with the precision required by each experiment using a heater and a needle valve.

1.1 Description of the equipment

The equipment is a cylindrical cryostat with a length of 1576 mm and a maximum external diameter of 500 mm. It has a vacuum chamber for thermal isolation that allows an optimal work below 10^{-5} mbar. As it can be seen in Fig. 1.1 there is a space for liquid nitrogen, with a volume of 25 litres, and another for liquid helium, of 16 litres. In order to cool the sample from 300 K down to 1.8 K a rotary pump is connected to the top and bottom part of the cryostat. The magnet is in contact with the helium bath. Homogenity of the magnet has been measured at 5 T (see Fig. 1.2). Table 1.1 summarizes some magnet specifications.

The helium flow through the sample space is controlled by opening or

MAGNET SPECIFICATIONS	
H_{max}	5.0 T at 4.2 K
Cold bore	84.0 mm
Homogeneity	0.1 % over 10 mm
Persistance	5 parts in 10000 per hour
Current	< 100 A
Switch type	Persistent

Table 1.1: Magnet specifications.

closing the needle valve, as it is sketched in Fig. 1.3. This operation can be done manually or using the temperature controller, ITC503 (Oxford Instruments). A motor system runs the needle valve and the heater to stabilize the temperature around the desired value. The needle valve regulates the helium flow entering the sample space and the heater warms the system by applying a small electrical current. The equipment has two inner thermometers, one at the sample holder in case the dummy probe is being used, and the second one near the heat exchanger. The dummy probe is a basic measurement system designed by Oxford Instruments to be used in this equipment. Besides that, different probes have been built in order to increase the range of experiments performed. When one of the newly designed probes is used an extra thermometer near or in contact with the sample is added as the experiment requires.

The upper part of the cryostat with all its connections can be seen in Fig. 1.4 and Fig. 1.5, and different pictures of the equipment are shown in Fig. 1.6. The probe is inserted into the cryostat through an entrance that is located at the center (see label N in table 1.2 and Fig. 1.5). Next to it, there is the needle valve motor connected to the inner part in order to move it mechanically (label D). There are two connections for the rotary pump, one for the vacuum chamber and the other for cooling down (see label G in Fig. 1.5 and table 1.2). On the outer part of the top we find two ports that connect to the nitrogen space (labels L and M). The quench valve has a security purpose (label P).

The magnet will only work properly if all the conductors remain in the superconducting state. If any part of the windings goes resistive, the current passing through will cause ohmic heating, and this will start a transition of part of the magnet that is in a superconducting state to a normal state. All the stored energy in the magnet will dissipate rapidly,making the liquid helium to boil very quickly and often warming the magnet to a temperature significantly above 4.2 K. This helium gas goes out the system through the

quench valve. There is also a one way valve connected to the helium space, from where the helium gas evaporates (label R). Next to the quench valve we find the coaxial current lead that connects the power supplier with the magnet (label J). The current source applies a maximum of 98.175 A corresponding to 5 T. We can change the rate of the magnetic field applied as it is needed in the experiment. For a more detailed description the legend of Fig. 1.5 is presented in Table 1.2. Pictures of different connections of the magnet are shown in Fig. 1.7.

No	DESCRIPTION	QTY/SIZE
A	O.V.C pressure relief valve	50 mm
B	Lifting eye bolt	M8
C	Wiring for helium level probe	4 pin Fischer
D	V.T.I. Auto needle valve	Auto
E	Wiring for auto needle valve heater & sensor	10 pin Fischer (orange)
F	Wiring for V.T.I	10 pin Fischer (green)
G	O.V.C. vacuum valve	NW25
H	Wiring for S/C switch	10 pin Fischer (yellow)
J	120 AMP co-axial current lead	
K	Helium syphon entry	9.5 mm
L	N_2 fill / vent port	
M	N_2 level probe & safety valve	
N	Dummy insert - NW40	10 pin Fischer (blue)
P	Quench valve	NW25
Q	Helium recovery port	NW25
R	One way valve	NW25

Table 1.2: Legend of Fig. 1.5.

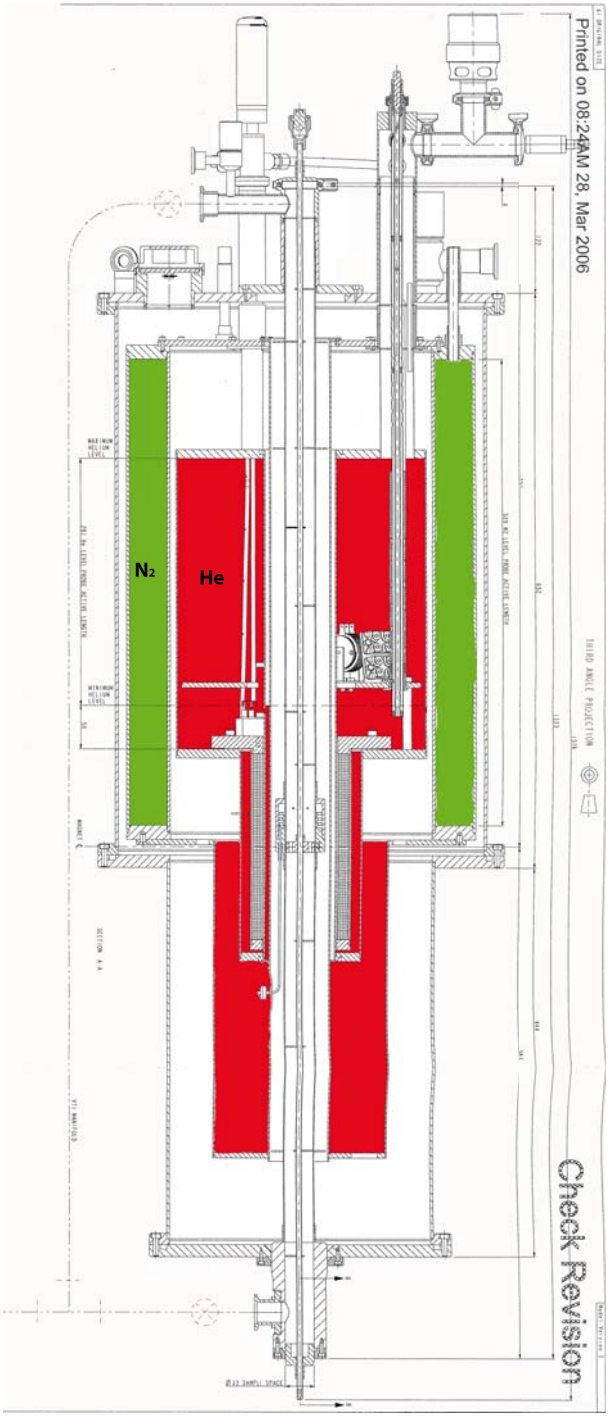

Figure 1.1: Sketch of the cryostat as a whole. The vacuum chamber, the nitrogen space and the helium space are colored respectively in white, green and red.

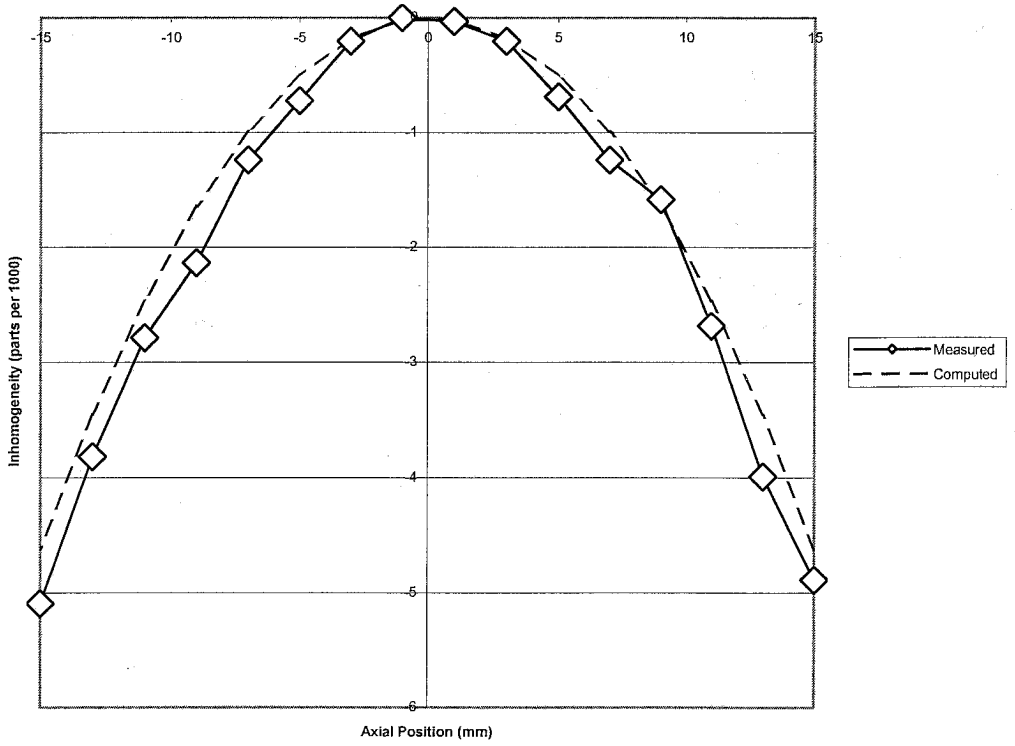

Figure 1.2: Homogenity of the magnetic field at 5 T from the center of the sample space. The signal of the magnet was studied with a Hall probe installed in the sample space with the temperature controller operating at 300 K.

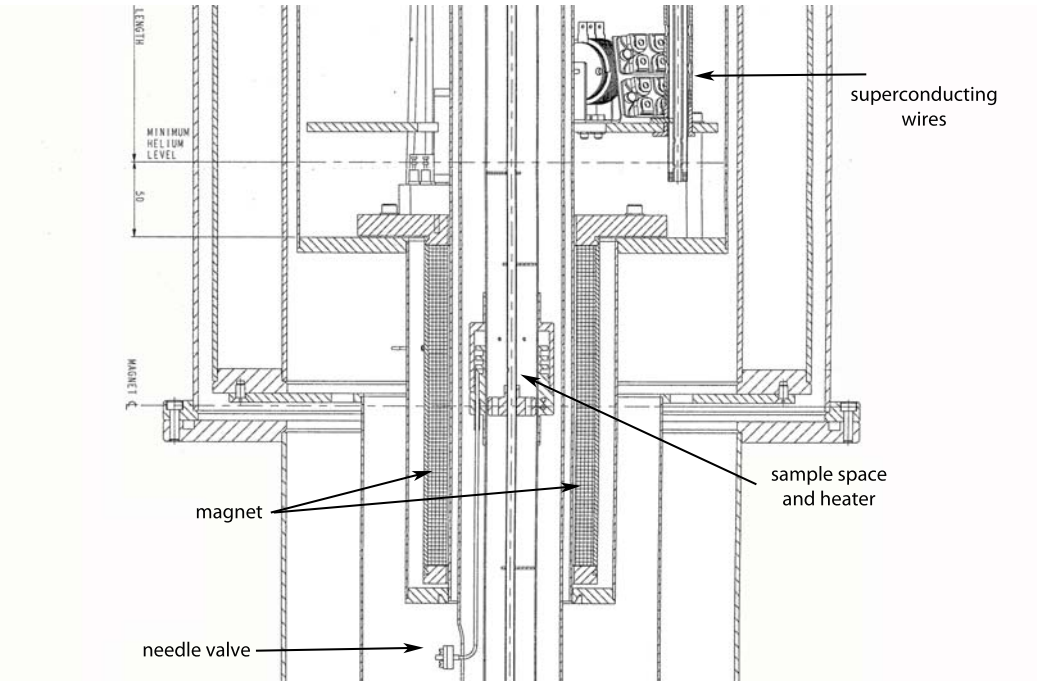

Figure 1.3: Sketch of the inner part of the cryostat where the magnet is placed.

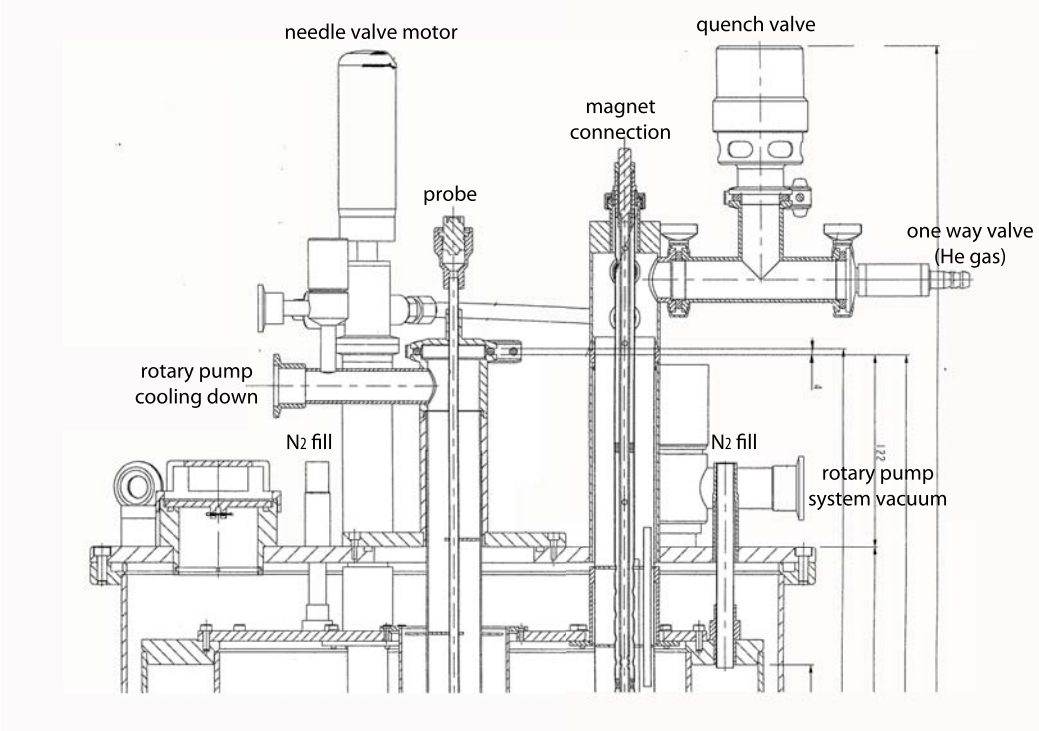

Figure 1.4: Sketch of the upper part of the cryostat.

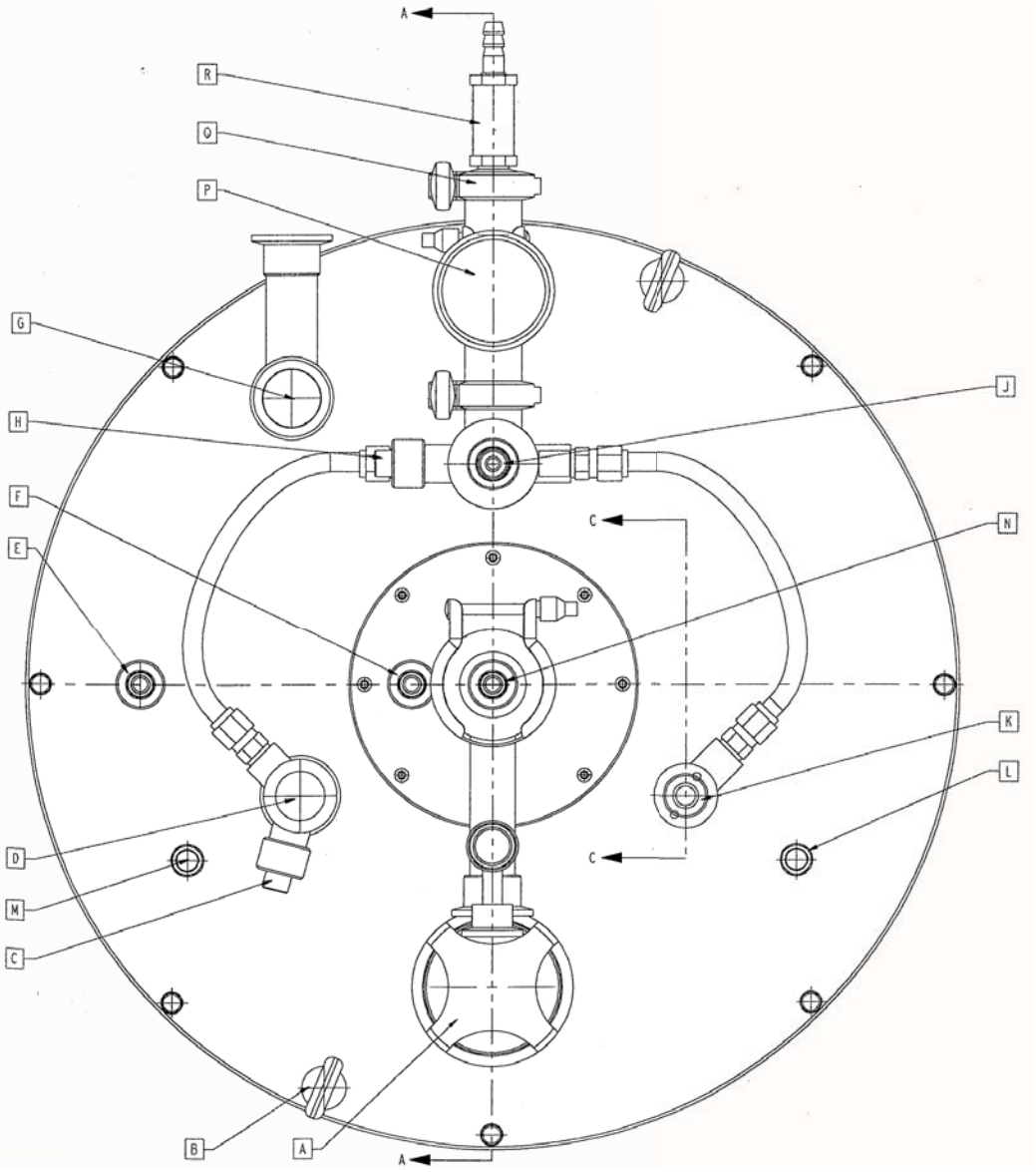

Figure 1.5: Sketch of the upper part of the cryostat, as seen from top. See table 1.2 for legend details.

Figure 1.6: Different pictures of the cryostat.

Figure 1.7: Different pictures of the connections between the magnet and the power supply source.

1.2 Starting up and running the equipment

The equipment is in the Grup de Magnetisme of Universitat de Barcelona since May 16th 2006. After building and placing it on spot a vacuum of 10^{-5} mbar has to be reached before starting operation. To this end, the rotatory pump is turned on. When high vacuum is reached the helium space is then purged. This procedure consists in filling this space with helium gas and pumping it away with the rotatory pump, repeating the process at least three times. In the last place the space is over-pressurized with helium gas (see Fig. 1.8.b). After that, pre-cooling with nitrogen is started, filling both spaces, helium and nitrogen, with cryogenic liquid (see Fig. 1.1). In Fig. 1.8.c. liquid nitrogen is being transferred to the helium space which is connected to the nitrogen space by a plastic tube in order to fill both spaces for pre-cooling.

Once the system has been cooled down to nitrogen temperature, the helium space is emptied and the liquid nitrogen recovered. Next the helium space is purged at least twice and then the transfer of helium is started as in Fig. 1.8.a. When there is enough helium inside the cryostat to reach the minimum level the magnet can be turned on. The equipment is connected to ground and the heater is set to 68 mA and the magnet to 98.175 A, a value that corresponds to 5 T. When the helium transfer is concluded the pump is turned on, the valves are opened and the cooling procedure starts. The descending temperature rate depends on the aperture of the needle valve. Opening it around a 25% allows to reach 2 K in 20 minutes approximately without wasting much helium. The ITC can be operated from a computer, allowing a temperature sweep to be programmed and performed automatically, by controlling the heater and the needle valve. This can be done together with a magnetic field sweep so that a set of experimental results can be taken while the system is unattended.

When the system needs to be stopped, the magnet, the heater and the pump are turned off, and the needle valve is opened slightly to let the temperature rises freely.

Next, the procedure to introduce or change the probe at any time of the experiment will be described. In case of being at low temperature, the first step is closing the needle valve, turning off the pump and setting the temperature at 300 K. This will turn on the heater and start a fast temperature increase. When a temperature of 300 K is reached the sample space is over-pressurized with helium gas. Then the heater is turned off and the needle valve is fully opened to avoid freezing. At this point everything is ready to loosen the bottom part that fixes the probe and to open the bridle on the top. When the probe is out the cryostat the lids are put at the bottom and

at the top.

When the experiment is changed and the probe has to be introduced back in the cryostat, the same procedure is followed. To reopen the system high temperature and overpressure are needed in the sample space. When everything is set again the system is ready to be cooled down.

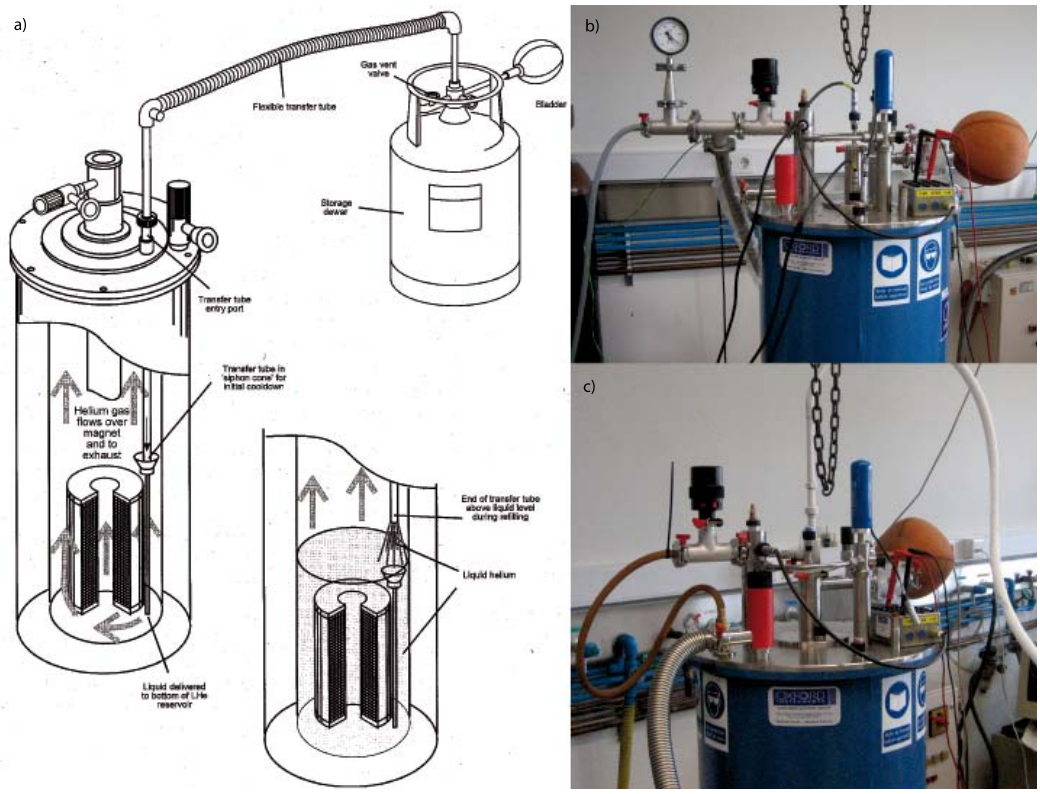

Figure 1.8: a) Sketch of helium transfer from the dewar to the cryostat. **b)** and **c)** Different pictures of helium transfer.

1.3 Probe development and testing

Different types of probes for a wide range of experiments in our cryostat have been developed in order to be as versatile as possible. Following this idea each one has been divided in two halves so they can be combined as it is preferred in each experiment. The three different halves and the parts these are made of can be found in Fig. 1.9.

Each probe is made of a 8-to-10-mm-diameter stainless steel tube that is used to protect and to give some stiffness to the measuring device. The

dimensions of the probe can be seen in the sketch of Fig. 1.10. Some rings (red piece in Fig. 1.11) have been welded all along the probe in order to reflect radiation and to center the probe inside the cryostat. The lid to seal the vacuum of the sample space and a 16 pin Fischer connector have been placed at the top of the upper part. The yellow piece shown in Fig. 1.11 fastens the sample holder and connects the two parts of the probe.

Two different designs of the lower part of the probe are presented in Fig. 1.9. The first one is only the stainless steel tube with the radiation rings and a piece to seal the vacuum at the bottom part (see the light grey piece in Fig. 1.11). In the second one a 16 pin Fischer connector is added at the bottom in order to be able to perform resistance experiments.

A coaxial cable and different waveguides are added to these stainless steel jackets, so we end up having nine halves, four upper parts that can be combined with five lower parts. There are three waveguides working in ranges 33-50 GHz (WR22), 50-75 GHz (WR15) and 75-110 GHz (WR22), and a coaxial cable that maintains the fundamental mode at a frequency of 60 GHz.

Different sample holders have been designed and built according to the needs in each experiment. The sample holder is placed inside two semi-cylindrical pieces attached to the yellow piece and connected directly to the coaxial cable or the waveguide. A sketch of the yellow piece can be seen in Fig. 1.12 and two pictures of the sample holder appear in Fig. 1.13.

Once the probes have been built, they have been tested to make sure the system is able to reach high vacuum and to be cooled down. Problems found along the way have been solved and now all the probes work properly. At the same time wires are added to all the probes in order to measure with the Fischer connector. To make this job easier and to be able to change samples faster some small connectors have been attached to the probe as it is shown in Fig. 1.13.

Two thermometers calibrated in a MPMS-QD and a box of connections are ready to use. The box has been specially designed for this system in order to enable simultaneous measurements with two Fischer connectors (lower and upper part) in the same box in case is needed.

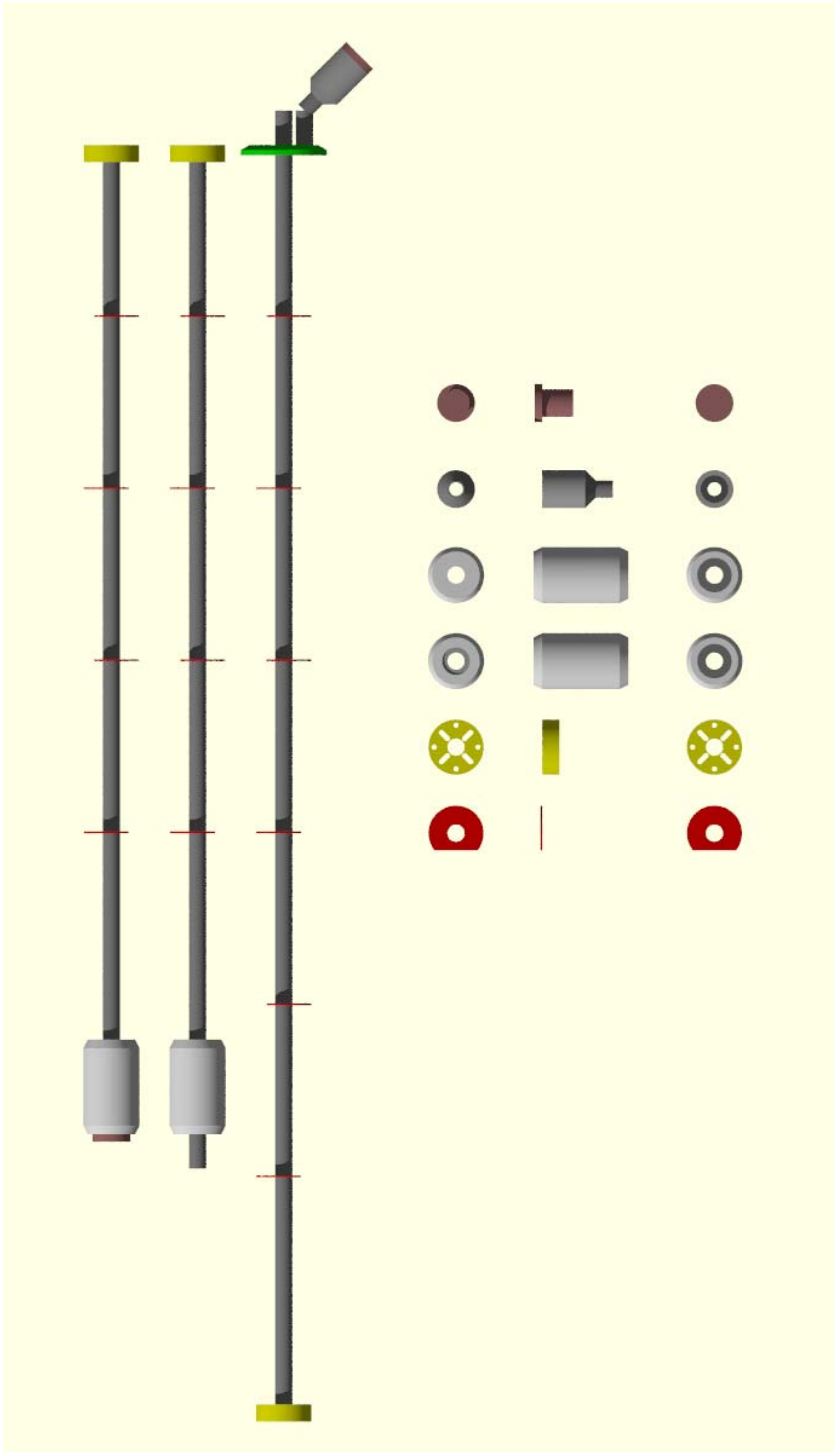

Figure 1.9: Sketch of a probe and the pieces is made of.

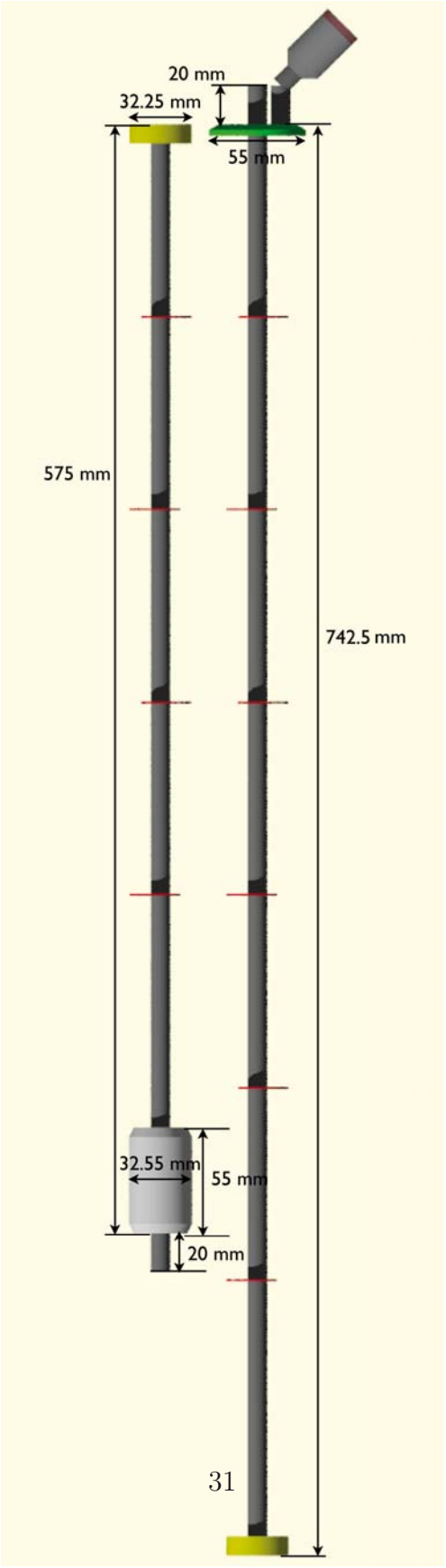

Figure 1.10: Dimensions of the measuring probe.

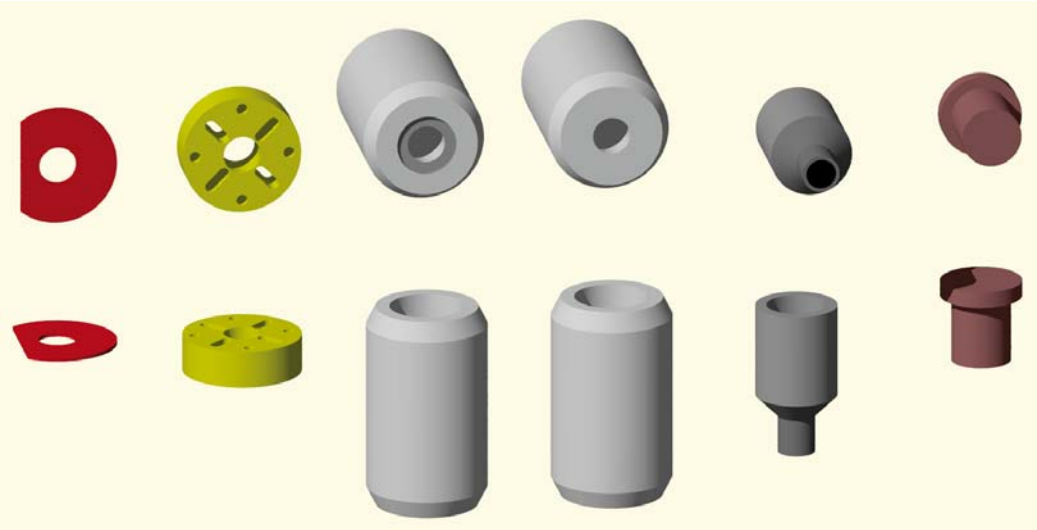

Figure 1.11: Pieces from the probes. From left to right: radiation rings, to stop radiation through the probe hole; the piece that fixes the sample holder; two designs for the piece that closes the vacuum in the lower part of the probe when it is set inside the cryostat; two pieces that hold the Fischer connector.

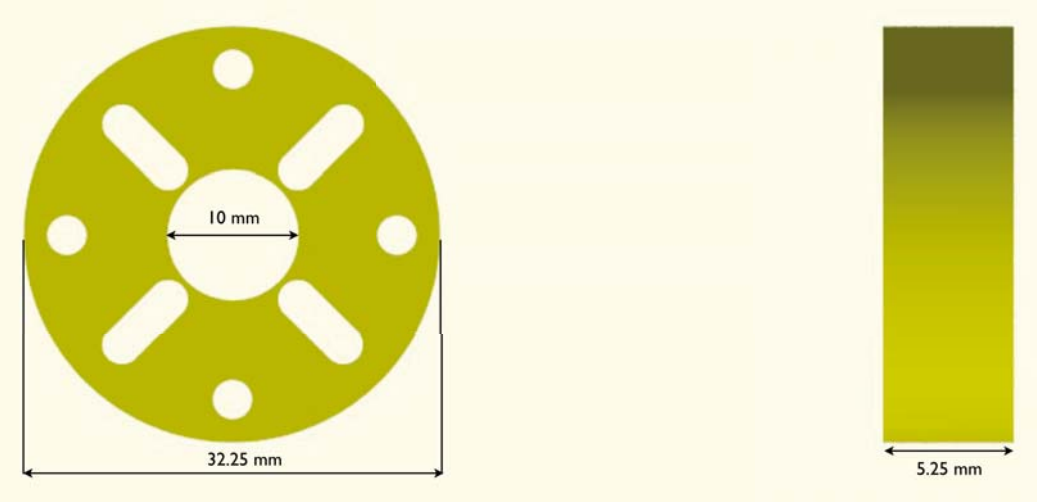

Figure 1.12: Dimensions of the piece that fastens the sample holder.

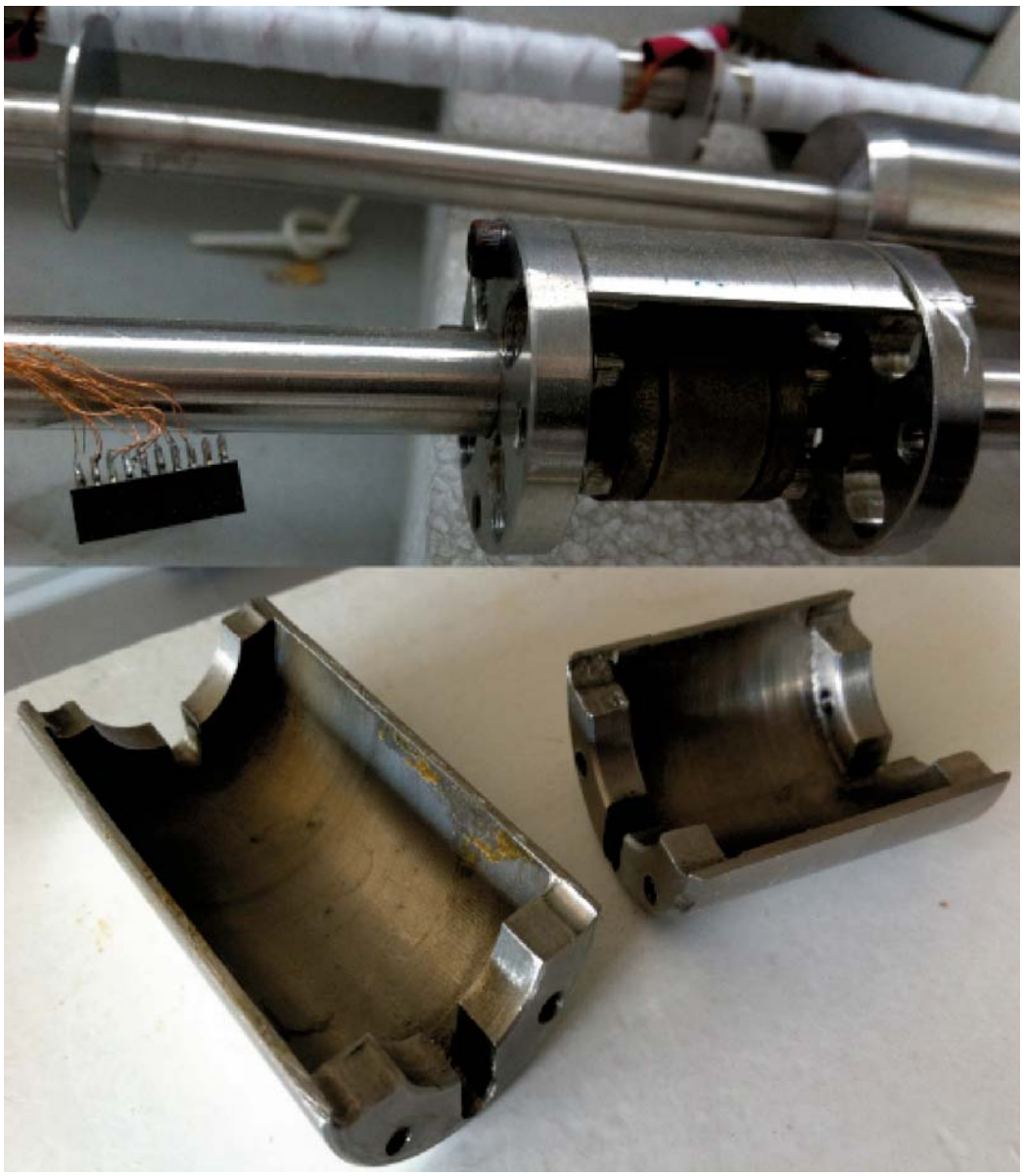

Figure 1.13: Pictures of sample holders of two different sizes.

Chapter 2

Test measurements

In this chapter I will present different measurements that have been performed in order to test and improve the system. The importance of these experiments lies not in the results but in the need of testing the equipment to ensure proper operation. The physics of some of these experiments has been extensively discussed in Alberto Hernández thesis [2]. MW measurements in TiN thin films open a new research line that should be developed in the future.

2.1 Mn_{12}-acetate measurements

Single Molecule Magnets (SMMs) consist of a core of strongly exchange-coupled transition metal ions that have collectively a large magnetic moment per molecule. SMM crystals have a number of advantages over other types of magnetic nanostructures. Most importantly, they are monodisperse: all the molecules in the crystal have the same spin, orientation, magnetic anisotropy and atomic structure. This fact enables fundamental studies of intrinsic properties of magnetic nanostructures that have previously been beyond reach. One of the most important results obtained on these compounds is the observation of quantum tunneling between different states of the magnetization of the molecule, leading to a stepwise hysteresis magnetization curve with acceleration of the magnetic relaxation [3, 4]. From a technological point of view, these systems have several new potential applications. As an example, SMMs have been proposed for use in quantum computing and quantum information storage [5, 6].

Mn_{12}-acetate, first synthesized in Poland by Lis [7] in 1980, is one of the most important SMMs. It is characterized by a spin $S = 10$ with a ground state possessing a huge Ising-type magnetic anisotropy with an energy barrier

in zero magnetic field of $U(H = 0) \approx 60$ K. The magnetization relaxes very slowly at low temperature (for instance, at 2 K the relaxation time of the magnetization becomes of the order of months) following a thermally activated behavior according to the Arrhenius law,

$$\Gamma = \Gamma_0 \exp\left[-U(H)/k_B T\right], \tag{2.1}$$

where $U(H)$ is the anisotropy barrier, Γ_0 is a prefactor that for Mn_{12}-acetate is $\Gamma_0 \approx 10^7$ Hz and Γ is the rate of the barrier transition, which is the relaxation probability per unit of time, or the relaxation velocity.

This means that below a certain temperature, known as blocking temperature T_B, the spins cannot overcome the anisotropy barrier on the time scale of a measurement and become blocked. It is then when the sample can be prepared in a non-equilibrium state, the magnetization dynamics towards equilibrium can be studied and magnetic hysteresis of molecular origin is observed. The spin-dependent part of the Hamiltonian of the molecule in the first approximation is

$$\mathcal{H} = -DS_z^2 - \mathbf{H} \cdot \mathbf{S}, \tag{2.2}$$

where $\mathbf{H}$ is the magnetic field and D is the anisotropy constant of order 0.6 K [8, 9]. It results in the spin energy levels shown in Fig. 2.1.a. When $H_z = 0$, the spin levels at both sides of the anisotropy barrier with $m' = -m$ are in resonance. For $H_z \neq 0$ these resonances disappear, but for certain values, $H_z = kH_R$ ($k = 1, 2, 3, ...$), they are recovered for levels m at the left side of the barrier and $m' = -m - k$ at the right allowing spin tunneling, see Fig. 2.1.a. This leads to the stepwise hysteresis curve of a Mn_{12}-acetate crystal [3, 4], with $H_R = 0.48$ T, see Fig. 2.1.b.

Crystals of molecular magnets also exhibit another outstanding effect: magnetic avalanches [10, 11]. They correspond to the fast spontaneous reversal of the magnetic moment of the crystal within the time of a millisecond [12]. It has been demonstrated that a magnetic avalanche is equivalent to the burning of a chemical substance, a process which is known as deflagration [13]. In molecular magnets, the role of the chemical energy is played by the Zeeman energy. Further studies of magnetic deflagration revealed effects due to quantization of spin levels [14]. A detailed theory of the ignition and propagation of magnetic avalanches has been developed [15].

2.1.1 Experimental setup

The first experimental setup used to test the equipment was a device built in the Paul Drude Institut (Berlin), by Paulo Santos group. It consists in a

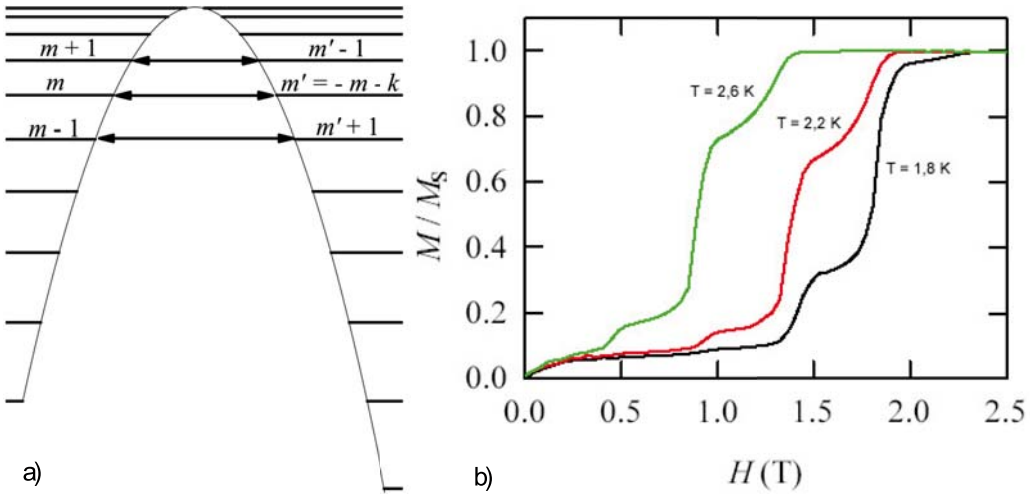

Figure 2.1: a) Energy levels of a Mn_{12}-acetate molecule. **b)** First magnetization curves at different temperatures.

transducer containing nine Hall probes in a row, to which current is applied through the corners and voltage is measured in order to detect the change in the magnetization of the sample. The small transducer is set on a stamped circuit board where the contacts have been welded (see Fig. 2.2). The board is stuck on a plastic piece in order to fit the sample holder shown in Fig. 1.13.

As it has been previously described, the probes used in this cryostat have two separate parts. For the upper part we use the probe with the coaxial cable, that has also been welded to the device, while the lower part is the one that contains an extra Fischer connector. With the lower part we measure Hall probes from 1 to 4 and with the upper part probes 5 to 9.

Besides the thermometer in the cryostat, an extra one (Lakeshore RX-102A-BR) is held near the sample and connected by 4 wires, in order to have a better estimation of the sample temperature.

A small Mn_{12}-acetate crystal is placed centered on the Hall probes with its easy axis parallel to the row of nine contacts.

2.1.2 Experimental results

After cooling down and setting the equipment ready to measure, the proper running of the Hall probes at low temperature is tested. It is observed that the best signal corresponds to probes 6 and 9. To start the measurements, a sequence of hysteresis cycles has been performed on the sample, applying

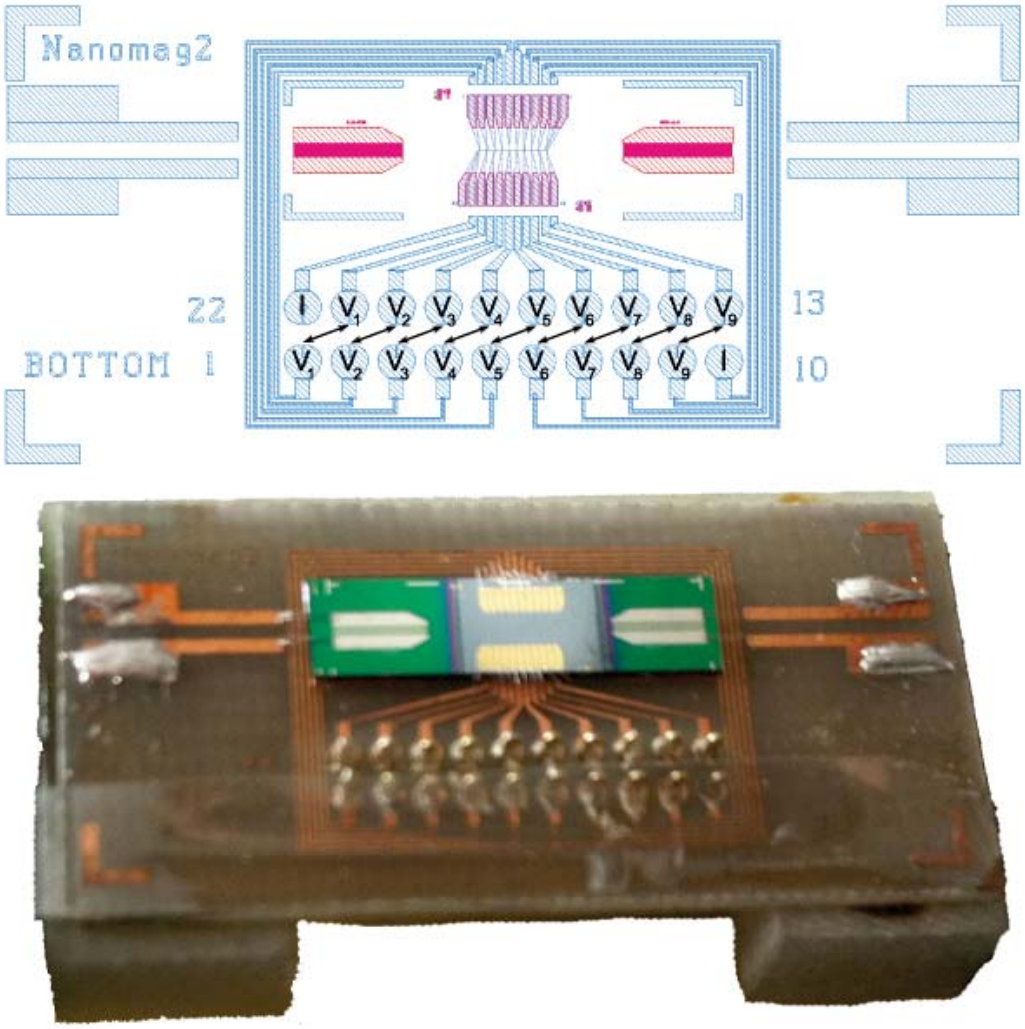

Figure 2.2: Sketch and picture of the transducer used in the first experiments performed in the cryostat.

a sweep of magnetic field from +3 T to -3 T or vice versa, and registering simultaneously the changes in magnetization. A similar cycle is obtained for each Hall probe. The result corresponding to probe 9 is shown in Fig. 2.3.

As it has been explained before, the sample presents resonances for certain values of $H_z = kH_R$ ($k = 1, 2, 3, ...$), where $H_R = 0.48$ T, leading to a stepwise hysteresis curve. These measurements were repeated several times in order to test the system and the probes. No spontaneous avalanches were observed in this experiments. After that, some tests were performed with a network analyzer to detect the transducer resonant frequencies. The result obtained

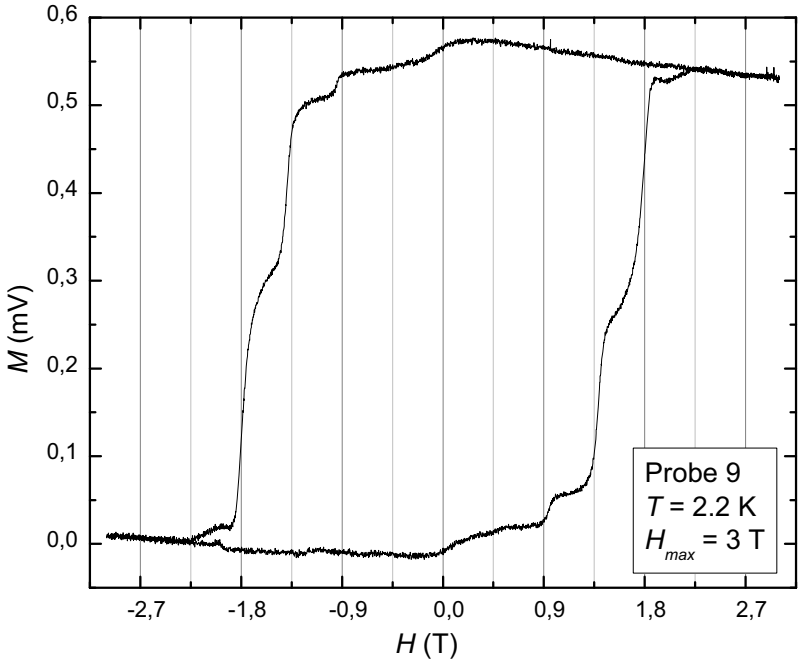

Figure 2.3: Magnetization curve of the Mn_{12}-acetate sample measured at 2.2 K with probe 9. Magnetization is presented in mV because it is proportional to the direct electrical signal detected by the Hall probes.

is presented in Table 2.1. This means that for these frequencies part of the radiation applied to the system reaches the transducer and is not reflected but transformed into surface acoustic waves (SAW) that propagate through the transducer and get to the sample causing the crystal lattice to vibrate. SAW provide the sample with the energy necessary to change the magnetization, and perhaps, ignite a magnetic avalanche.

f (MHz)	width (MHz)	height (mU)
261.58	0.5	100
784.20	0.5	140

Table 2.1: Table of the transducer resonant frequencies. The height of the peak is presented in mU (milliUnits) that corresponds to transmission. 100 mU and 140 mU correspond to a transmission of the 10% and 14%, respectively.

Different measurements as a function of time have been performed for the two resonant frequencies for temperatures from 2 K to 30 K and applying pulses from 0.1 ms to 500 ms, with $P = 15$ dBm and $H_z = 1$ T. Finally, and after doing some system improvement, some avalanches were repetitively detected for short pulses at 2 K, as it is presented in Fig. 2.4. The procedure that has been followed is described below:

1. A temperature $T < T_B$ is fixed.
2. A magnetic field H_z = -3 T is applied to saturate the sample.
3. The magnetic field is swept from -3 T to 1 T. It is important to notice here that if the magnetic field reaches a certain value, a spontaneous avalanche could be ignited and when the SAW pulse is applied the system would already be in an equilibrium state.
4. When H_z is stable a pulse is applied and the signal is registered as a function of time, as it can be seen in Fig. 2.4.

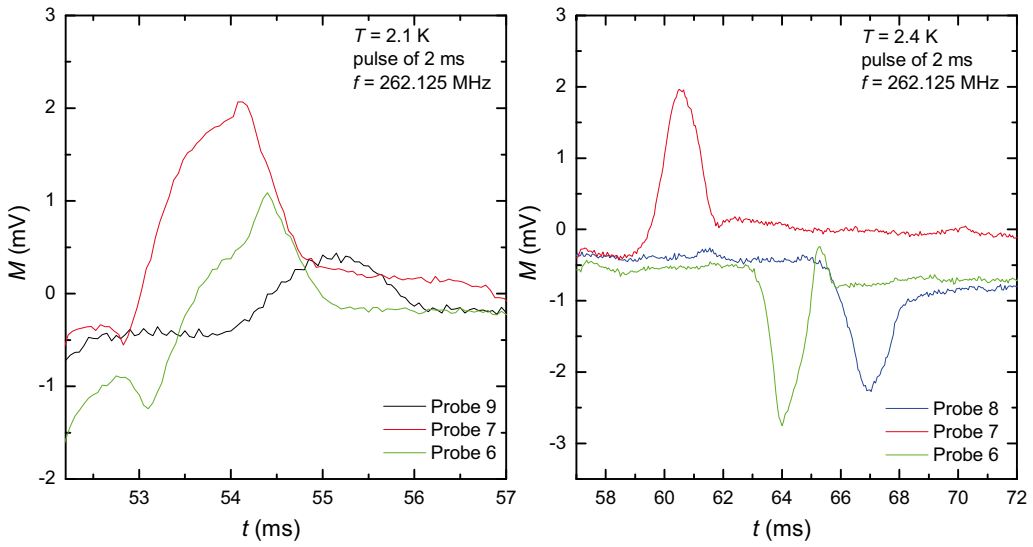

Figure 2.4: Avalanches in a Mn_{12}-acetate crystal applying pulses for two different temperatures.

In Fig. 2.4 phonon-induced avalanches are observed for several Hall probes. The measurement has been performed by applying a 2 ms MW-pulse and detecting the signal of each probe at a time. After the first pulse,

all the procedure explained above has to be repeated in order to be able to ignite another avalanche which is recorded by another probe. Considering the order of the peaks, it can be assumed that the avalanche is ignited at the point where probe 7 is placed and spreads toward the edges of the sample. The height of the peaks is affected by the sensitivity of the probes.

The width of the peaks represents the time the avalanche takes to cross the sample during deflagration, detected by every single probe at a time. As it has been published, the propagation velocity depends on temperature [16]. For lower temperatures the propagation accelerates and this fits the results presented, where thinner peaks and shorter ignition time for 2.1 K than for 2.4 K can be observed.

The aim of this experiment has been achieved. On the one hand, results extensively studied in Alberto Hernández thesis [2] have been reproduced. On the other hand, the capacity of a new transducer for measuring magnetic avalanches has been proved and it has been used to test the system for further improving.

By the end of this experiment the proper operation of two of the measuring probes designed has been validated. The system worked perfectly well cooling down to low temperature and applying magnetic fields up to 3 T. Several problems were detected, as some bad welding at the connection box and too much noise in some measurements. Both have been solved by repeating the welding and isolating the wires. It has been noticed that, as the measuring probe is in a vertical position, the sample slips when the temperature increases if it is fixed to the transducer with vacuum grease. The problem can be solved by using another material as GE-varnish to fix the sample, being always careful to avoid damaging the Hall probes.

2.2 Measurements using Hall probes

In this chapter, some results measured with Hall probes built at the Physics Department of the University of Central Florida, Orlando, are presented. These Hall probes are the result of a collaboration with Enrique del Barco's Group. The set has been placed on a printed circuit board where the bondings have been welded in order to protect them and have an easier manipulation. Each Hall probe has eight contacts for measuring voltage and two to inject current.

2.2.1 Experimental setup

For this experiment a special assembly has been designed. The probe set is fixed with GE-Varnish to a small teflon plate and this is placed inside the sample holder as it is shown in the sketch in Fig. 2.5. A wire connection is built to link the Hall probe with the upper and lower parts of the probe, dividing the measurements in two blocks. The upper part allows to measure the thermometer, the current and probes 1 to 4. The lower part allows to measure probes 5 to 8. Everything is controlled through the connection box and is directly plugged to the measuring instruments. A multichannel card has been used, to be able to measure the eight probes simultaneously.

All experiments have been performed on three different Hall probes with similar properties. All of them have been previously checked at room temperature in order to detect a possible malfunction with the bondings or connections. All problems have been solved during the development of experiments.

A small Mn_{12}-acetate crystal is placed with its easy axis parallel to the row of Hall probes. The crystal is shifted slightly upwards so that the latest probes are not in contact with it (5 to 8 approximately).

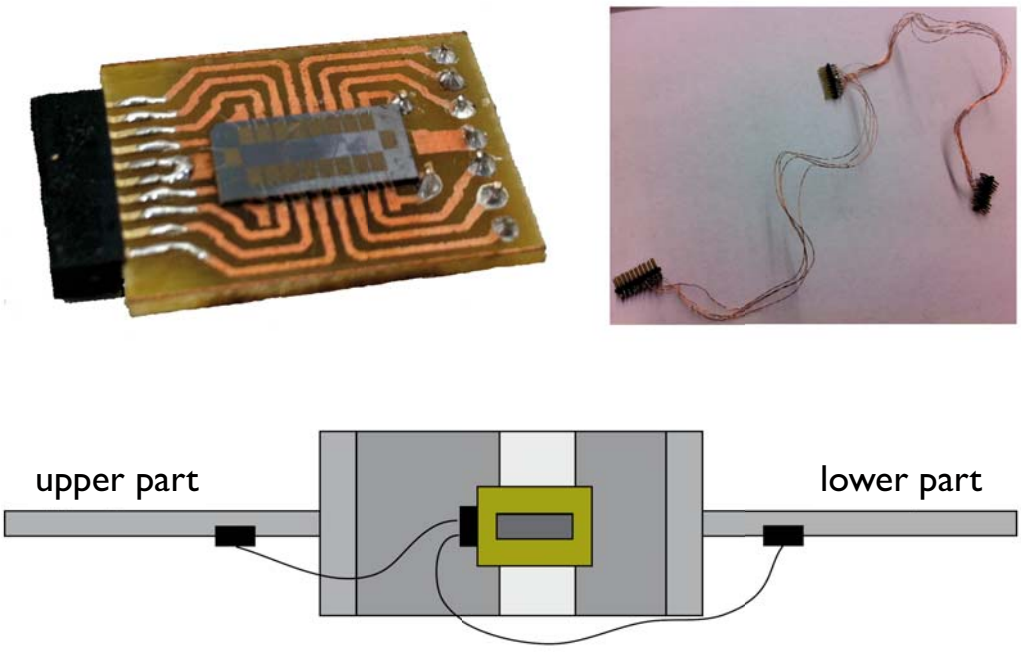

Figure 2.5: Top: Hall probe set tested in the system and wire connection to link the set with the upper and lower parts of the measuring probe. Bottom: sketch of the experimental assembly.

2.2.2 Experimental results

First, all Hall probes have been tested at room and low temperature. The purpose of these experiments is to detect spontaneous avalanches in a Mn_{12}-acetate crystal while applying a sweep of magnetic field at different rates. The experiment has been performed with three different Hall probes.

First the temperature desired is set between 1.6 K and 2.5 K. Next, a high magnetic field is applied to the sample, for some crystals over 3 T and for some others over 4 T, in order to saturate it. After that the magnetic field is swept back to zero and its polarization is changed. At this moment the chosen rate is applied and the field is increased again to high values. The signal is registered as a function of the magnetic field. In the last step, if conditions are appropriate, a spontaneous magnetic avalanche should ignite.

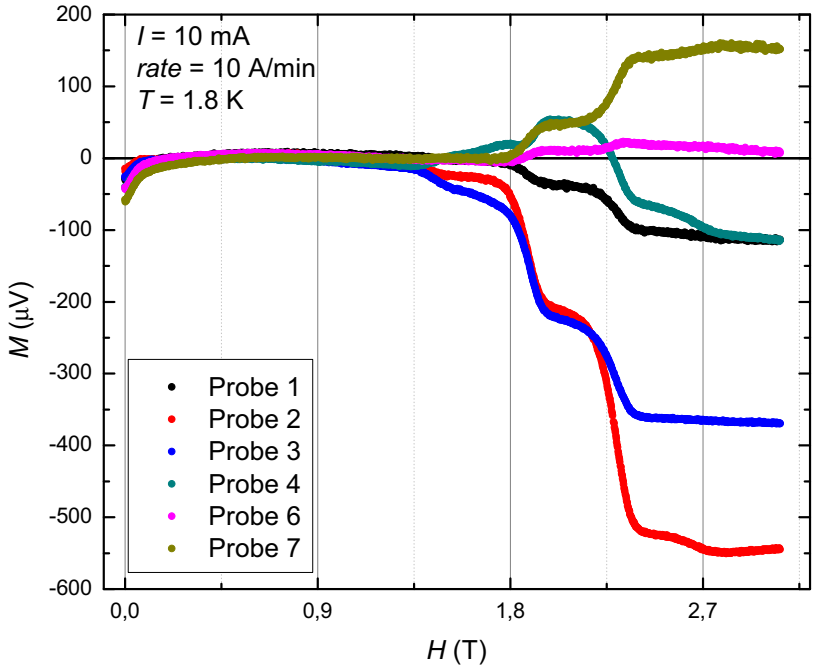

Figure 2.6: Magnetization of a Mn_{12}-acetate crystal detected by six of the nine contacts of the Hall probe as a function of the magnetic field. Relaxations at the forth and fifth resonances can be observed.

Experiments have been performed for several temperatures and different

rates of the sweep of the magnetic field. An example of the signal registered is shown in Fig. 2.6. No spontaneous magnetic avalanches have been observed in any measurement. This can be explained as follows. To ignite an avalanche the temperature inside the sample should be raised enough by the magnetic energy released as phonons. This induces the acceleration of the magnetic relaxation. The reason why this is not happening could be either that the sample is very small and there is more surface than inner mass, or because the system is too well thermalized. Contrary to the experiments performed on a SQUID magnetometer, where spontaneous avalanches have been measured [14,17], in our equipment the sample is in permanent contact with the helium flow and this may make the ignition of the avalanche more difficult.

The steps shown in Fig. 2.6 correspond to the forth and fifth resonances following $H_z = kH_R$ ($k = 1, 2, 3, ...$), as it has been already explained. The plot shows a negative increase of the magnetization for probes 1, 2 and 3 and a positive change for probes 6 and 7. This means that 6 and 7 are at the right of the midpoint of the sample and 1 to 3 at the left. This would fit the setup described in the previous section. Probe 2 sees a huge change of the magnetization compared to the other ones, because probably it matches one of the edges of the sample and this adds an odd behavior.

Probe 4 should see nothing considering the scheme described because it matches the center of the sample. As it can be observed in Fig. 2.6 the magnetization instead first increases and then decreases. That a probe in the middle of the sample detects a signal can be explain in two ways:

1. Any imperfection in the shape of the sample could affect the signal of the centered probes.

2. It could happen that the relaxation would either start first at one edge and would propagate to the other, or start at both edges and propagate to the center, causing an inhomogeneous variation of magnetization and then a signal on the midpoint probes.

   The differences in the dipolar field at the center and the corners of the sample should make the field at the edges larger and would make the relaxation begin there.

We can also discuss the change of magnetization as a function of the sweep rate of the magnetic field, as it is shown in Fig. 2.7. Measurements with rate 2 A/min and 3 A/min have the expected behavior found in other publications [18], but the jump at rate 10 A/min appears at a magnetic field value smaller than expected. Two possible explanations can be proposed here:

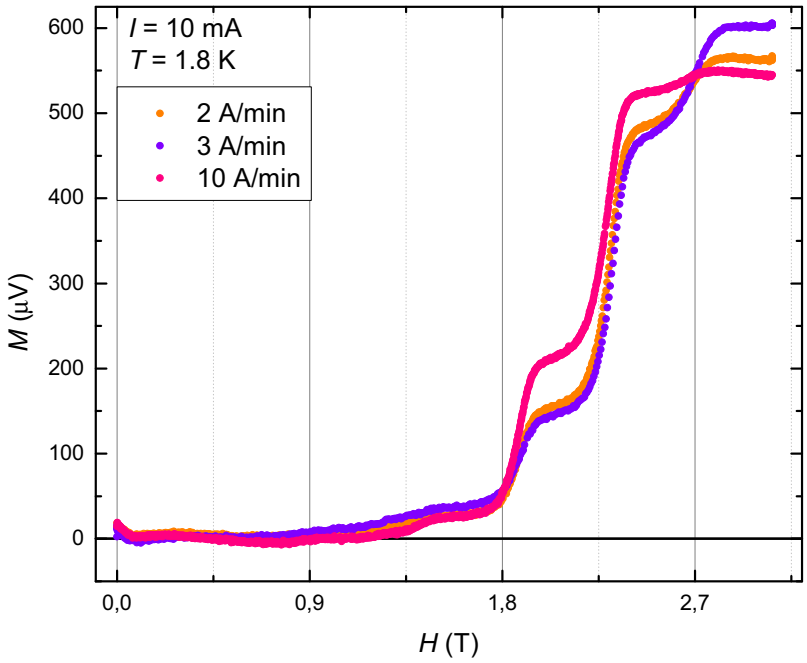

Figure 2.7: Stepwise hysteresis curve of a Mn_{12}-acetate crystal for different sweep rates of the magnetic field.

1. The easiest one would be that the temperature is not stable enough and this affects the relaxation. Checking the temperature, in all cases it oscillates between 1.6 K and 1.7 K. This should not be considered unstable enough to explain the anomaly at 10 A/min.

2. Analyzing the result at the resonance, jumps should appear in order from low to high rate, 2, 3 and 10 A/min, and so on. The higher the rate the less time has the system to relax and the smaller the variation should be, as it can be seen between 2 and 3 A/min. In the result for 10 A/min, the effect of phonon heating in the sample, that in more adiabatic conditions would lead to an avalanche, causes an increase in the relaxation rate. The sample is then close to ignite an avalanche but not enough. Perhaps we might talk of a slow avalanche or a fast relaxation (faster than normal relaxations at 2 and 3 A/min) that would explain these results.

It is important to notice that there is a second change in the order of the jumps at the end of the measurement. This has no relation with the sample but with the sensitivity of the Hall probes, since the sample has already relaxed completely.

2.3 Microwave measurements on a TiN thin film

As a result of a collaboration with V.M. Vinokur (Materials Science Division, Argonne National Laboratory, Chicago, USA) and T.I. Baturina (Institute of Semiconductor Physics, Novosibirsk, Russia) titanium nitride (TiN) thin films have been studied as it will be extensively presented in the second part of this thesis. TiN is a ceramic material that presented as a thin film has a superconductor behavior.

Although the main idea was to perform transport measurements in a dilution refrigerator, it turned interesting to use the new equipment to study the interaction of MWs with the samples in transmission conditions, due to the special characteristics of the system. In this case, MW measurements were performed on a plain sample, as the one shown in Fig. 5.1, but with a width of 500 nm and a transition temperature around 2.2 K.

2.3.1 Experimental setup

The sample has been placed between two MW coaxial SMA panel connectors in order to perform the transmission measurements. In order to prevent the sample from crushing, the perimeter of its cross-section was rolled up with an indium filament. The two connectors are fixed by teflon screws leaving a space of 0.86 mm between them. The assembly is shown in Fig. 2.8.

The measuring probes used in this experiment are the two half parts with the coaxial cable. The assembly is connected to the coaxial cables and set into the sample holder in order to fix the probes in the same way as it is presented in the upper part of Fig. 1.13.

When this is done, the probe is set inside the cryostat and connected to a network analyzer, that will be the radiation source and will measure the transmission coefficient (S_{12}). All electrical connections have been previously checked and an extra thermometer measures the sample temperature.

Figure 2.8: Experimental sample assembly for MW measurements on a thin TiN film.

2.3.2 Experimental results

All experiments have been performed with an automated LabVIEW program developed specially for these experiments. In the first place, transmission measurements as a function of the temperature were registered in zero magnetic field. The range of temperature studied is from 1.95 K to 2.80 K, taking the sample from the normal (N) to the superconducting (SC) state. For every step of temperature 14 different frequencies from 1 GHz to 67 GHz have been registered. The results of these measurements can be observed in Fig. 2.9.

Data information has been normalized to high and low temperature in order to be able to observe behavioral changes more easily. This has been done following the expression

$$\frac{S_{12}(\mathrm{N}) - S_{12}(T)}{S_{12}(\mathrm{N}) - S_{12}(1.8\ \mathrm{K})}, \tag{2.3}$$

where $S_{12}(\mathrm{N})$ is the value at the normal state, $S_{12}(1.8\ \mathrm{K})$ corresponds to the SC state and $S_{12}(T)$ is the signal registered at every temperature. Starting at high T, for every value of the temperature all the frequencies in study are registered, and so on until the lowest T value.

As it can be observed in the figure, it appears that for low frequencies the behavior is similar to that shown typically by the imaginary part of the magnetic susceptibility, while for high frequencies it mostly follows the behavior of the real part of the magnetic susceptibility. The imaginary part represents a shift of the phase of the transmission signal. Considering this result, it can

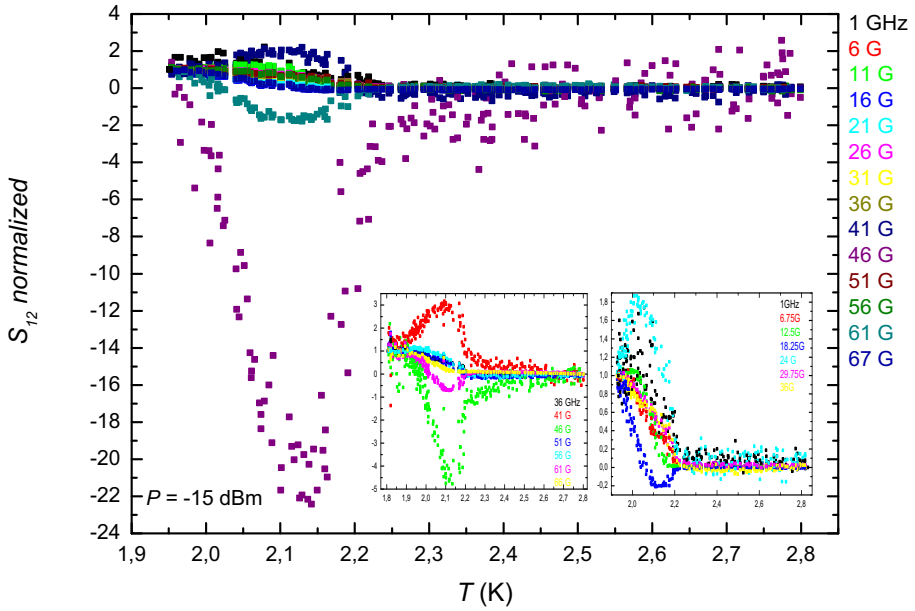

Figure 2.9: Transmission measurements as a function of temperature for 14 different frequencies from 1 GHz to 67 GHz. The insets show high (left) and low (right) frequencies separately. The vertical axis corresponds to the normalized transmission signal.

be deduced that for low frequencies there is a greater absorption of the sample. The peak of the variation fits the transition temperature of the sample, $T_c \approx 2.2$ K. For this kind of sample in the normal state the transmission is complete, while in the SC state it is a perfect mirror. Transmission features appear between T_c and the so called Berezinskii-Kosterlitz-Thouless temperature, T_{BKT}, that is the temperature at which the whole sample is in the SC state.

Transmission as a function of the frequency for different temperatures is presented in Fig. 2.10. For each temperature a sweep of the frequency is performed. In this case the signal has been normalized at high T by subtracting the signal from the value of the normal state [S_{12}(N)-$S_{12}(T)$]. It can be observed here that the signal detects more changes at low frequencies and for low temperatures, especially around T_c. This presentation shows at which frequencies the experimental setup is more sensitive.

A remarkable change at some specific frequencies, as 13 GHz, 26 GHz

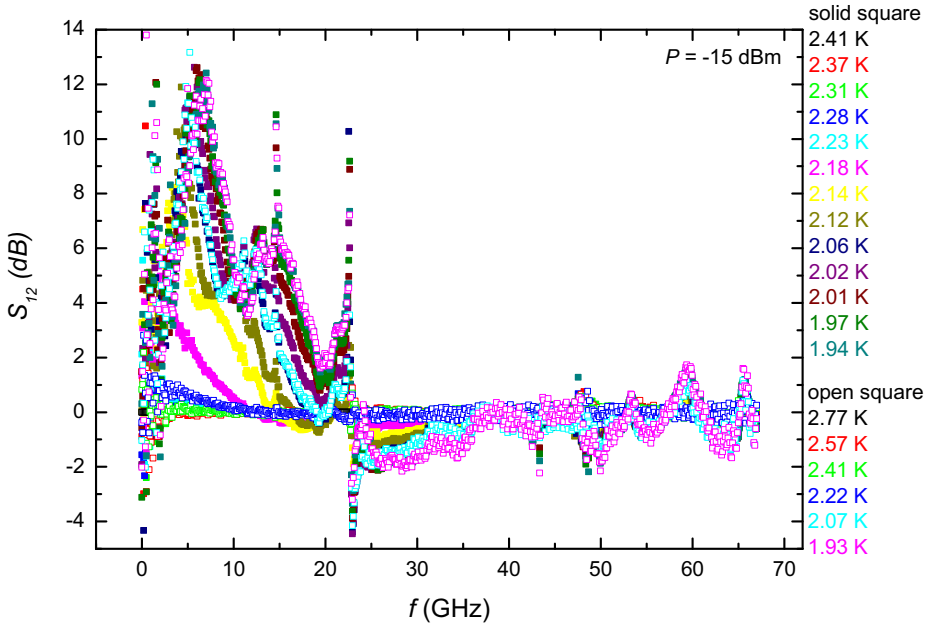

Figure 2.10: Transmission measurements as a function of the frequency for different temperatures from 1.93 K to 2.77 K.

and 46 GHz, can be observed both in Fig. 2.9 and 2.10. These seem to be resonant frequencies of the experimental setup, that arise from an artifact in the signal, not from the sample.

In Fig. 2.11 and 2.12 the last set of measurements with MWs is presented. Transmission detection was performed here for different temperatures and frequencies applying an external magnetic field. The sequence of the experiment was the following:

1. The temperature desired is set and stabilized. The range goes from 1.8 K to 2.4 K, with a step of 0.05 K.

2. The magnetic field is selected. The range of measurement is from 0 to 1.5 T.

3. For each magnetic field a frequency sweep is performed from 100 MHz to 67 GHz, measuring 134 different frequencies (in order to record the frequency with a step of 0.5 GHz) for each step of the magnetic field.

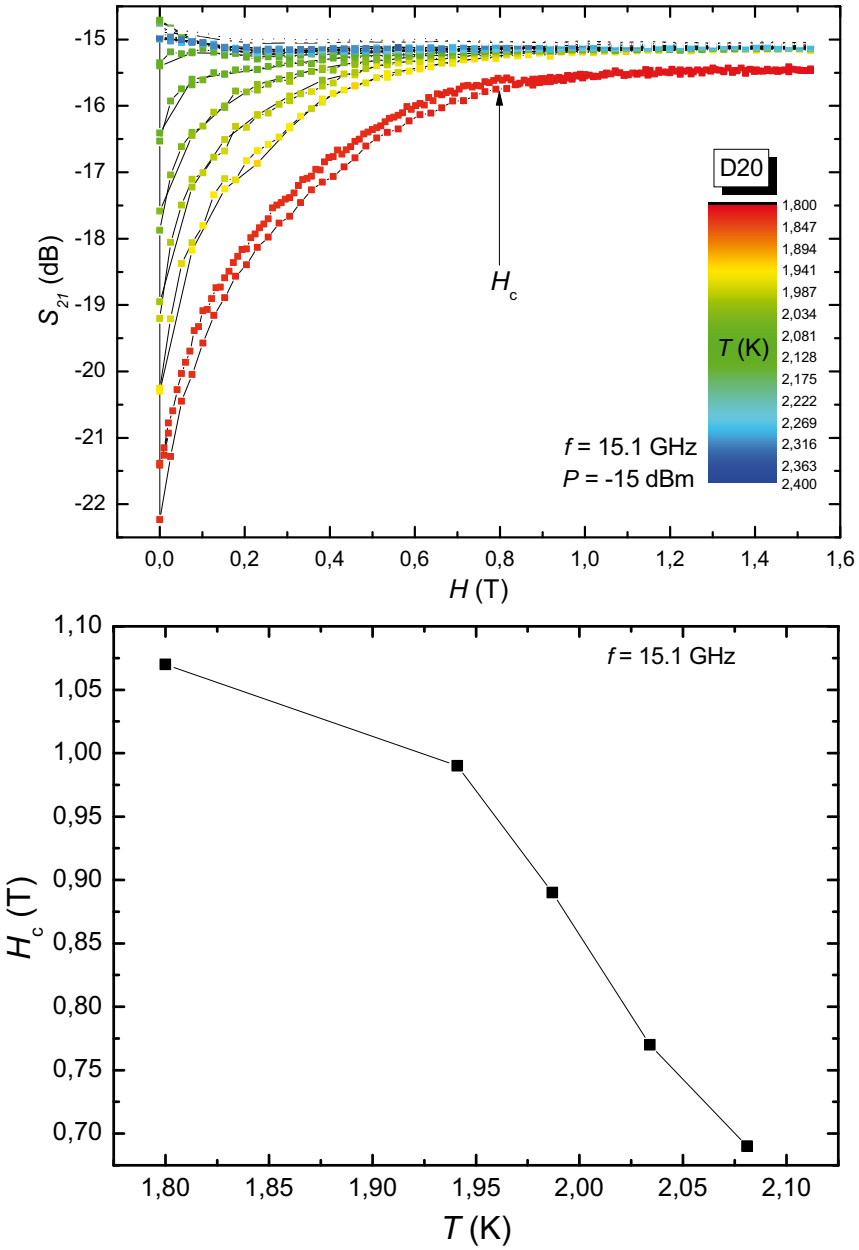

Figure 2.11: Top: Results from the measurements of transmission as a function of an external magnetic field for a frequency of 15.1 GHz. Bottom: Analysis of the critical field as a function of the temperature for 15.1 GHz.

It is important to notice here that between two complete measurements the sample is heated back to the normal state and cooled down again, waiting

time enough to stabilize the temperature. Two examples of these results can be seen in the top panels of Fig. 2.11 and 2.12. The increasing or decreasing behavior of these results for some frequencies only depends on how each frequency affects the measurement. In fact, the measuring system is a resonator dependent on the working frequency and therefore this is the trend observed.

Studying the magnetic field at which the sample turns superconductor (this is the H value at which S_{12} changes behavior going from high to low field) for the frequency of 15.1 GHz the result shown in the bottom panel of Fig. 2.11 is obtained. It follows the behavior expected for a superconducting material. The same behavior is obtained repeating this analysis for all frequencies. Therefore the result can be considered as a measurement of the SC transition by applying MW.

The behavior of an unexpected peak, called H_{min}, detected in the transmission measurements as a function of the magnetic field for some frequencies is analyzed in the bottom panel of Fig. 2.12. It can be observed that the peak moves with frequency following a linear behavior that could be interpreted as a ferromagnetic resonance, with a gyromagnetic ratio of 32.83 GHz/T and a g-factor of 2.34. The main idea here is that H_{min} is not from our sample but an artifact of some part of the experimental setup, probably from some magnetic impurity in the SMA connectors. Further measurements should be performed with different connectors in order to determine the origin of H_{min} and suppress it.

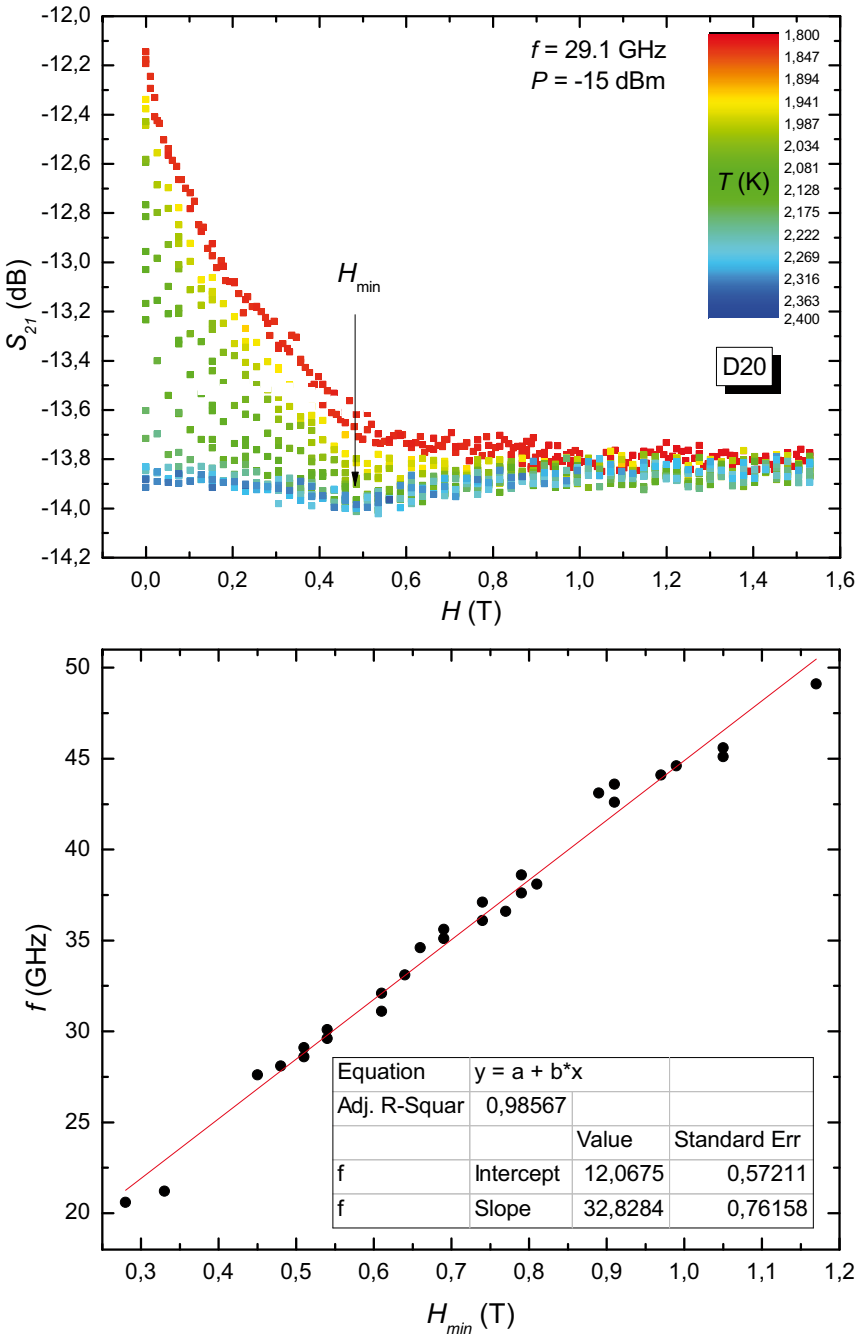

Figure 2.12: Top: Results from the measurements of transmission as a function of an external magnetic field for a frequency of 29.1 GHz. Bottom: Analysis of the displacement of H_{min} with the frequency.

Chapter 3

Conclusion

The aim of the first part of this thesis was to prove the development and improvement of a new equipment built to study magnetic and electrical properties, specially applying MWs in reflection and transmission conditions. For this purpose different probes were designed, built and tested.

The equipment has been successfully improved and checked using three different experimental setups that allowed, on the one hand, to test the system by performing experiments already known, and on the other, to start trying transmission measurements that will be in the future the main experiments developed in this cryostat due to its special characteristics.

Finally, the cryostat is working systematically and is ready to measure in a automatic way using different control programs that have been developed specially for this purpose. The probes and sample holders built are flexible enough to enable the change between different experiments immediately and are easy to adapt to any kind of modification that fits the system.

The MW experiments performed on a TiN thin film open a future research line to try to study the superconducting gap. The transition between the normal and the superconductor state has been observed under the application of microwave radiation. An unexpected feature, H_{min}, probably because some kind of magnetic impurity in the experimental setup, appears at some frequencies as a function of the magnetic field. Further measurements should be performed to ascertain its nature and be able to suppress it.

Part II

Quantum transport in thin TiN films and nanostructures

Chapter 4

Introduction

The second part of this thesis focuses on the measurements of thin TiN films in a dilution refrigerator working with a mixture of ^{3}He and ^{4}He that enables experiments at a few tens of millikelvins. The cryostat also contains a superconductor magnet which can apply a magnetic field up to 5 T. Transport experiments as a function of the temperature, the magnetic field and an external current have been performed during the last three years.

A thorough discussion of the results and questions that are still open is presented at the end of this work.

4.1 TiN bulk properties

Titanium nitride (TiN) belongs to transition metal mononitrides. These are materials of considerable interest due to their unique combination of properties: elevated hardness, high melting temperatures, high thermal stability, low electrical resistivity and an important range of superconducting properties. Table 4.1 summarizes some properties of bulk TiN. [19]

Property	TiN
Crystal structure	fcc, NaCl-type
Lattice parameter	4.23 Å
Density	5.43 g/cm^3
Resistivity	21.7 $\mu\Omega$cm
Melting point	3290°C
Hardness	9-10 Mohs

Table 4.1: Bulk properties of TiN at room temperature. [20]

4.2 TiN thin film properties

Titanium nitride (TiN) is an extremely hard ceramic material with very interesting properties that enable a huge amount of applications from mechanical to microelectronic to biotechnological.

Is often used to form thin film coatings on titanium alloys, steel, carbide, and aluminium components to improve the substrate's surface properties. As TiN has excellent infrared reflectivity properties too it can also be used as anti-reflective coating.

Assuming an important role in microelectronics TiN is commonly used as diffusion barrier in contact structures of silicon integrated circuits, due to its high thermodynamic stability, a low resistivity and that it can be deposited with a good step coverage (that is the ratio of the thickness of a film along the walls of a step to the thickness of the film at the bottom of a step). While the film blocks diffusion of metal into the silicon, it is conductive enough (30 - 70 $\mu\Omega$cm) to allow a good electrical connection. In this context, TiN is classified as a "barrier metal", even though it is clearly a ceramic from the perspective of chemistry or mechanical behavior. Recent chip design in nanotechnology use TiN as a metal material for improved transistor performance. [21]

Due to its high biostability, TiN layers may also be used as electrodes in bioelectronic applications [22] like in intelligent implants or in-vivo biosensors that have to withstand the body fluid severe corrosion. TiN electrodes have already been applied in the subretinal prothesis project [23] as well as in biomedical microelectromechanical systems. [24]

Focusing on solid state physics, in 2008, a titanium nitride thin film was cooled down to millikelvin converting it into the first known superinsulator, with resistance suddenly increased by a factor of 100,000 [25]. This finding promoted the development of the second part of this thesis. Like superconductors, which have applications in many different areas of physics, from accelerators to magnetic-levitation trains or MRI machines, superinsulators could eventually find their way into a number of products, including circuits, sensors and battery shields.

The most common methods of TiN thin film creation are physical vapor deposition (PVD, usually sputter deposition, cathodic arc deposition or electron beam heating) and chemical vapor deposition (CVD). In both methods, pure titanium is sublimated and reacted with nitrogen in a high-energy, vacuum environment.

The principal problem with the PVD technique is step coverage, which degrades rapidly with increasing aspect ratio of the feature size. Alternatively, the CVD of TiN, which works by the use of $TiCl_4/NH_3$ chemistry, has been applied to improve this problem, but on the other hand, several

issues limit the application of this chemistry to the production of device manufacturing [26, 27]:

1. Deposition temperature in the $TiCl_4/NH_3$ chemistry, which is greater than 600°C, is too high for the process to be applicable at all metallization levels.

2. The incorporation of significant amounts of impurities and Cl in the TiN film, especially at low deposition temperatures (< 600°C) is of major concern for long term reliability of finished devices.

To improve the problems related to $TiCl_4/NH_3$ chemistry, several different methods have been tested solving some existing problems but finding others or causing not desirable changes in some of the sample properties. [28–30]

A new deposition method that appeared around 2000 and seemed to solve most of the problems respecting, and in some cases improving, sample properties is Atomic Layer Deposition technique (ALD).

This is a new method for growing semiconductor materials by one atomic layer at a time. The growth sequential control of this system is based on saturating surface reactions between the substrate and each of the reactants used. Each surface reaction adds full or a partial fraction of a monolayer of the material on the surface and makes the growth rate proportional to the number of reaction cycles instead of the reactant flow rate.

The advantages of ALD over other CVD processes are excellent thickness uniformity, conformal step coverage, very low pinhole density, and complete elimination of particle generation by gas phase reaction [31–33].

The purposes of this ALD development are:

1. To lower the deposition temperature of the $TiCl_4/NH_3$ process.

2. To achieve excellent film quality of TiN films with low resistivity and low chlorine content.

The resistivity of TiN thin films appear to be inversely proportional to the deposition temperature. In general, the resistivity is affected by impurity content, preferred orientation, crystallinity of the thin film, and film microstructure. TiN film grown by the ALD process exhibited excellent step coverage along with high quality thin film properties such as low resistivity, low impurity content, and high density.

The samples of this thesis have been deposited, as it will be explained below, by ALD technique using titanium chloride ($TiCl_4$) as metal source

and ammonia (NH_3) as nitrogen source, as part of a Ph. D. thesis developed at the Katholieke Universiteit of Leuven by Alessandra Satta.

The density of the TiN film was calculated by ellipsometry thickness and the Rutherford backscattering spectrometry (RBS) areal density of Ti atoms, assuming stoichiometric films. The impurity content of the films was determined by RBS. Measurements were performed in a four point probe system in order to study the thin film electrical properties. A calculation of the film resistivity from the ellipsometry thickness and sheet resistance values allowed to study the deviations between the film and the bulk value [19]. Transmission electron microscopy (TEM) was used to investigate the microstructure of the TiN films.

Some results concerning particularly our sample will be presented in the next chapter.

4.3 Atomic Layer Deposition technique

ALD is an absorption controlled CVD process for thin film and simple crystal growth. ALD is based on two important ideas [34, 35]:

- Precursor molecules are supplied in an alternate way, in order to lead to a sequential gas-solid reaction.
- Gas-solid reactions have to continue until surface saturation is achieved. This enables better control of film thickness and uniformity.

These basic principles are an innovation of ALD techniques over conventional CVD where neither thickness nor uniformity cannot be controlled during the deposition process. Besides, in CVD the reactant molecules are simultaneously supplied leading to a possible formation of gas phase impurities. Table 4.2 presents the main differences between ALD and CVD.

For binary compounds (MN) the ALD reaction can be divided in two parts. In each part the surface is exposed to one of the two reactants. Actually, the complete cycle growth has four steps:

- Exposure to the first reactant.
- Exposure to an inert gas (normally Ar or N_2) to purge the chamber.
- Exposure to the second reactant.
- Exposure to the purging gas.

CVD	ALD
Less reactive precursors preferred	Highly reactive precursors preferred
Precursors react at the same time on the substrate (possible gas phase formation)	Precursors react separately on the substrate (elimination of gas phase)
Precursors are allowed to decompose at processing temperature	Precursors should not decompose at processing temperature
Uniformity requires constant flux of reactant	Uniformity ensured by the saturation mechanism
Thickness adjust by precise process control and monitoring	Thickness control by counting the number of reaction cycles

Table 4.2: Different process conditions in CVD and ALD techniques. [19]

The cycle is repeated until the desired film thickness is obtained. The thickness is proportional to the number of deposition cycles. In our case, to reach a 5-nm-thick sample, 200 cycles have been performed at a temperature of 350°C. Figure 4.1 shows the basic sequence for a binary compound.

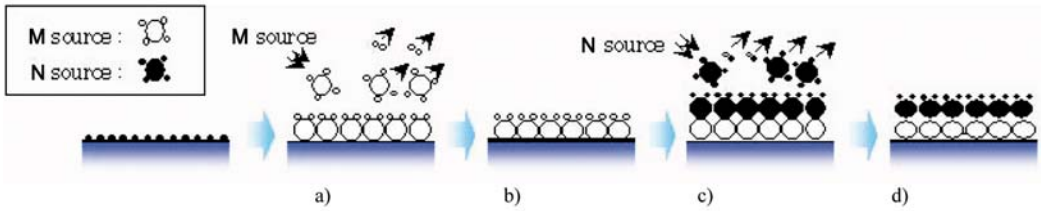

Figure 4.1: Basic sequence of ALD for an MN compound, from compound reactants $MX_n(g) = M$ source and $NY_n(g) = N$ source. **(a)** Introduction of $MX_n(g)$ onto the substrate surface. **(b)** Formation of a chemisorbed layer. **(c)** Introduction of NY_n onto $MX_n(s)$ surface, after a purging step to remove unreacted species and byproducts. **(d)** Formation of $MN(s)$ surface layer and release of $XY(g)$ byproducts. [19]

Chapter 5

Samples

In this thesis we present the results of the measurements performed on a 5-nm-thick TiN thin film, formed on 10 nm of SiO_2 grown on top of a $< 100 >$ Si substrate by ALD at 350°C [36]. In Fig. 5.1 we can see a cross section of the sample and easily differentiate the TiN thin film built on the SiO_2/Si substrate.

Analysis by atomic force microscopy (AFM) shows that the film exhibits low surface roughness and consists of a dense packing of crystallites, with an average size of $\sim$ 5 nm, as shown in Fig. 5.2, left. The samples were patterned into Hall bridges using conventional UV lithography and plasma etching. Fig. 5.3 shows a sketch of the pattern mentioned.

In this sample we can differentiate two parts. One half is a plain thin film and the other half has a square lattice of holes. We refer to these two parts respectively as film and perforated. To fabricate the nanoperforated film, a 80-nm-period square lattice of 20-nm-diameter holes was patterned covering part of the Hall bridge by electron beam lithography (EBL) and plasma etching. This square lattice is shown in Fig. 5.2, right.

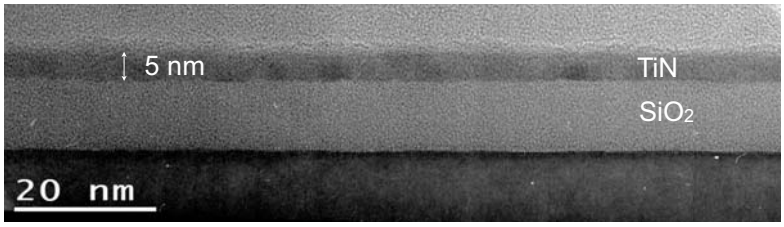

Figure 5.1: Cross section of the sample.

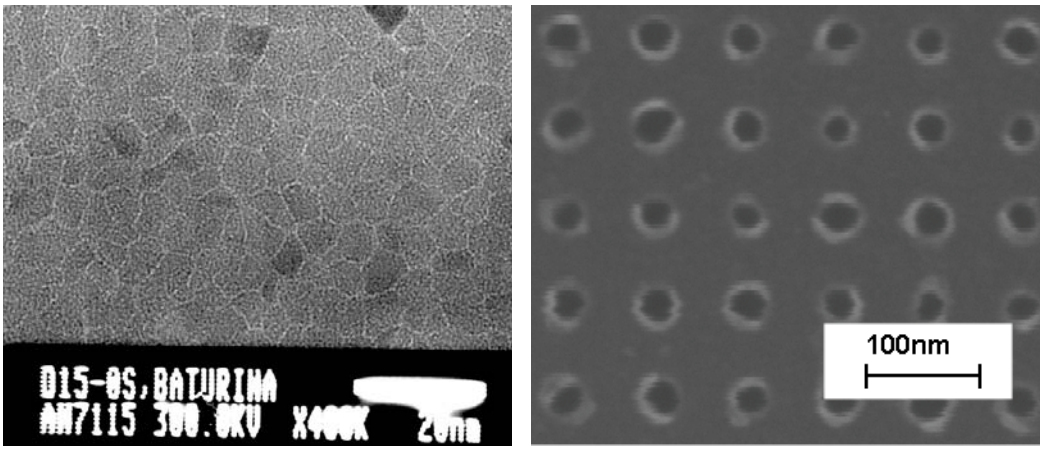

Figure 5.2: Left: Thin TiN film made by a packing of crystallites shown by atomic force microscopy. Right: Scanning electron micrography of the part of the TiN film patterned with the 80-nm-period square array of holes.

5.1 Fabrication of the Hall bridge and the nanoperforated film

As it has been said, the samples were patterned into Hall bridges using conventional UV lithography and plasma etching.

UV lithography is a process used in micro-fabrication to selectively remove parts of a thin film or the bulk of a substrate. It uses light to transfer a geometric pattern from a photomask to a light-sensitive chemical photoresist, or simply resist, on the substrate. A series of chemical treatments then either engraves the exposure pattern into, or enables deposition of a new material in the desired pattern upon, the material underneath the photoresist.

The pattern in the etching resist is created by exposing it to light, either directly or with a projected image using an optical mask. This procedure is comparable to a high precision version of the method used to make printed circuit boards. It is used because it can create extremely small patterns (down to a few tens of nanometers in size), it affords exact control over the shape and size of the objects it creates, and because it can create patterns over an entire surface cost-effectively. Its main disadvantages are that it requires a flat substrate to start with and it can require extremely clean operating conditions.

A single iteration of photolithography combines several steps in sequence. Modern cleanrooms use automated, robotic wafer track systems to coordinate the process. The most common steps in this procedure are the following:

- **Cleaning**: Before starting the process is important to clean the wafer (thin slice of semiconductor material used as substrate). If organic or inorganic contaminations are present on its surface, they are usually removed by wet chemical treatment.

- **Preparation**: The wafer is initially heated to a temperature sufficient to drive off any moisture that may be present on the wafer surface. Wafers that have been in storage must be chemically cleaned to remove contamination. A water repellent layer is added to prevent the aqueous developer from penetrating between the photoresist layer and the wafer's surface.

- **Photoresist application**: The wafer is covered with photoresist by spin coating. A viscous, liquid solution of photoresist is dispensed onto the wafer, and the wafer is spun rapidly to produce a uniformly thick layer. The photoresist-coated wafer is then pre-baked to drive off excess photoresist solvent, typically at 90 to 100°C for 30 to 60 seconds on a hot plate.

- **Exposure and developing**: After pre-baking, the photoresist is exposed to a pattern of intense light. Optical lithography typically uses ultraviolet light. Positive photoresist, the most common type, becomes soluble in the basic developer when exposed; unexposed negative photoresist becomes insoluble in the developer. This chemical change allows some of the photoresist to be removed. The resulting wafer is then hard-baked if a non-chemically amplified resist was used, typically at 120 to 180°C for 20 to 30 minutes. The hard bake solidifies the remaining photoresist, to make a more durable protecting layer in future ion implantation, wet chemical etching, or plasma etching.

- **Etching**: In etching, a liquid (wet etching) or plasma (dry etching) chemical agent removes the uppermost layer of the substrate in the areas that are not protected by photoresist.

- **Photoresist removal**: After a photoresist is no longer needed, it must be removed from the substrate. This usually requires a liquid "resist stripper", which chemically alters the resist so that it no longer adheres to the substrate. Alternatively, photoresist may be removed by a plasma containing oxygen, which oxidizes it. This process is called ashing, and resembles dry etching.

To perform the 80-nm-period square lattice of 20-nm-diameter EBL technique has been used.

EBL is the practice of emitting a beam of electrons in a patterned fashion across a surface covered with a film called the resist, [37] and of selectively removing either exposed or non-exposed regions of the resist. The purpose, as with photolithography, is to create very small structures in the resist that can subsequently be transferred to the substrate material, often by etching. It was developed for manufacturing integrated circuits, and is also used for creating nanotechnology architectures. The primary advantage of electron beam lithography is that it is one of the ways to beat the diffraction limit of light and make features in the nanometer regime.

Specifically the procedure used with the samples presented on this thesis was the following:

- **Bridge patterning**: In order to carry out the transport measurements the film was first patterned by means of the conventional UV lithography and plasma etching into the 50-μm-wide bridges, with a 100 μm distance between the voltage probes, see Fig. 5.3.

- **PMMA spin-coating**: As a first step of the EBL process, the films were spin-coated with the poly(methyl methacrylate) (PMMA) electron-beam resist with the molecular weight 950.000 diluted with anisole ($CH_3OC_6H_5$), providing the thickness of 180 nm after 30 seconds spinning at 3000 rpm.

  PMMA is a transparent thermoplastic, often used as a lightweight or shatter-resistant alternative to glass. It is sometimes called acrylic glass. It is also an economical alternative to polycarbonate (PC) when extreme strength is not necessary. Additionally, PMMA does not contain the potentially harmful bisphenol-A subunits found in PC. It is often preferred because of its moderate properties, easy handling and processing, and low cost, but behaves in a brittle manner when loaded, especially under an impact force, and is more prone to scratching than conventional inorganic glass.

- **Lattice patterning**: The samples coated with PMMA were subsequently baked over 30 min in a convection oven at the temperature 170°C. The desired network pattern was created by the exposure of the PMMA layer to the electron beam using *Raith*150 high-resolution EBL system (the diameter of the beam is of about 2.4 nm at 20 kV). The PMMA was used as a positive electron-beam resist since it provides the high contrast with respect to further developing. Upon removing of the exposed parts of the PMMA by the standard methyl-isobutil-ketone (MIBK)-isopropil 1:3 solution the pattern mask was formed.

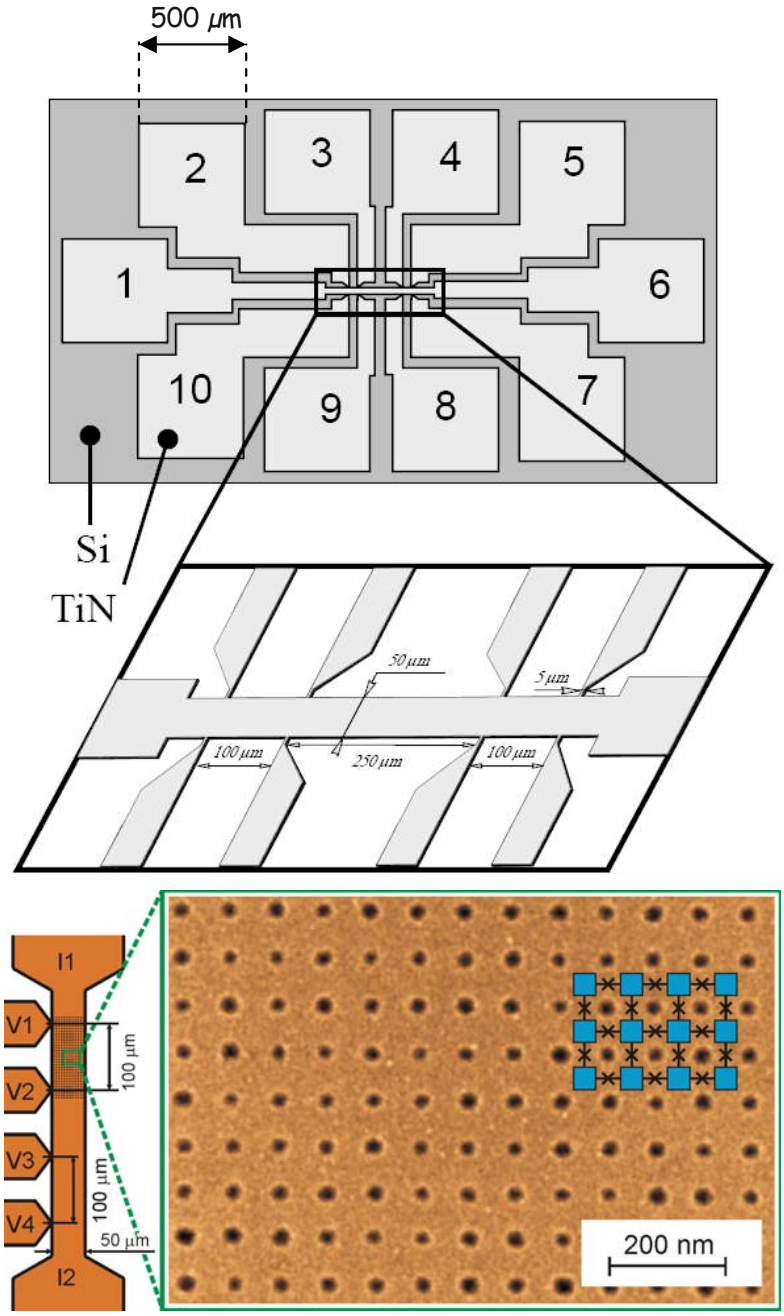

Figure 5.3: Top: Hall bridge patterned on the TiN sample by UV lithography and plasma etching. Bottom: 80-nm-period square lattice of 20-nm-diameter holes patterned covering part of the Hall bridge by electron beam lithography and plasma etching.

Following this procedure, a square lattice of holes with the diameter ~ 20 nm and the period $a = 80$ nm covering the 50 x 120 μm^2 area was created, see Fig. 5.3. The voltage probes $V_1 - V_2$ were designed to fall within the nanopatterned domain of the film, while the probes $V_3 - V_4$ were placed within the as-cast film. The nanopatterned section of the film confined between the probes $V_1 - V_2$ contained 50 μm x 100 μm/(80 nm)^2 = 781,250 elemental units.

Usually in the EBL systems the dots are designed as an array of single elements. Then the time necessary for settling the unique element gets critical for the overall time of the structure exposure. To design this TiN nanopatterned samples a special method has been developed, which allows the exposure of the array of 10^9 dots over a time as short as a few tenths of minutes. The strategy was to write a large rectangle, using a step equal to the array step. The size of the dots depended on the area dose and could be varied from 20 nm up to 120 nm as a result of the Gaussian shape of electron beam and of the proximity effect. It has been determined that the best patterning results are achieved if the energies of the electrons in the beam exceed or are equal to 20 kV, and the apertures size are small enough, about 7.5 μm, to ensure the round shape of the dots. The chosen design (pairs of $V_1 - V_2$ and $V_3 - V_4$ probes) allows comparing the physical properties of the patterned sections and the non-patterned sections of the film that were subject to the whole procedure except for being exposed to electron beam.

5.2 Sample properties

Our sample was grown by ALD at 350°C with $TiCl_4$ and NH_3 as precursors. For film characterization, TiN film was deposited on thermal SiO_2/Si substrates at 350°C. 10-nm-thick SiO_2 films were thermally grown at 750°C by a wet oxidation process. TEM was used to investigate the microstructure. Films are polycrystalline with columnar grain morphology, with grain boundaries being perpendicular to the surface. Maximum grain size is comparable to the thickness of the film.

For a thickness range of 10 to 30 nm, the film density is around 80% the bulk density. For films with a width < 10 nm, the density decreases to 70% the bulk value. Also, thickness effects start contributing to the resistivity. Electron scattering from the film surface and grain boundaries in polycrystalline films can significantly contribute to an increase of the resistivity of thin films, in addition to the bulk scattering (from impurities and vacancies). [38, 39]

Chapter 6

Measurements

6.1 Measurement development

In this chapter, experiments on a thin TiN film performed on a dilution refrigerator are presented. Three complete set of measurements corresponding to three evolution states of the sample are compared. State A was measured at the Institute of Semiconductor Physics in Novosibirsk (Russia) by Dr. Tatyana Baturina and her team in 2008, and states B and C were measured in Barcelona in 2009 and 2010 respectively, as part of this work.

Low-temperature transport properties of nanoperforated superconducting TiN films have been experimentally studied. Resistance measurements have been performed in the critical region of the superconductor-insulator transition (SIT), applying the magnetic field perpendicular to the plane of the structure or the dc current through the sample. SIT is a transition between a SC to a insulator state by localizing the Cooper pairs. Commensurability effects are observed at the magnetic field where the vortex lattice spacing matches the hole lattice period (80 nm). The evolution of the SIT with temperature, magnetic field and dc current is investigated in detail.

6.1.1 Dilution refrigerator

The principle of operation of the dilution refrigerator was originally proposed by H. London in 1951, but the first working systems were not built until more than ten years later. Since that time, the performance of these systems has widely improved, and the physical processes involved are now much better understood. Fig. 6.1 shows a schematic diagram of a common continuously operating dilution refrigerator.

The usual method of maintaining a low temperature is by evaporation of liquids with a low boiling point. The essence of the dilution refrigerator

method is to use a mixture of ^{3}He (boiling temperature 3.19 K) and ^{4}He (boiling temperature 4.2 K) which is separated into two phases (see Fig. 6.2). Inside the "mixing chamber", where the mixture is condensed, the two distinct phases are formed. One of them contains only ^{3}He while the other mainly consists of ^{4}He with only a small fraction of ^{3}He (is always composed of at least 6% of ^{3}He, no matter at what temperature). During operation, ^{3}He is removed from the ^{4}He-rich phase by pumping on it. As a consequence, ^{3}He atoms are forced to move from the ^{3}He-rich phase into the ^{4}He-rich phase, a process which is endothermal and therefore cools the system. For continuous operation, this process is repeated by using a closed circulation of ^{3}He, so that it is possible to run a built-in experiment at low temperatures.

As it has just been said, at temperatures below the triple point, the ^{3}He/^{4}He mixture separates into two liquid phases, divided by a phase boundary. On the one hand, the ^{3}He-rich phase corresponds to a point in the diagram below and to the right of the triple point, along the equilibrium line. On the other hand, the ^{4}He-rich phase corresponds to a point in the diagram below and to the left of the triple point, along the equilibrium line. The two phases are maintained in liquid-vapor form. Since there is a boundary between both phases, extra energy is required for particles to go from one phase to another.

When pumping with a rotary pump on the ^{4}He-rich phase, ^{3}He is mostly removed (meaning a move to the left off the equilibrium line in the diagram), destroying the equilibrium state. To restore equilibrium, ^{3}He will have to cross the phase boundary from the ^{3}He-rich side to the ^{4}He-rich side, but it needs energy to do so. The ^{3}He-rich phase will provide the ^{3}He and get the energy in the form of heat from the walls of the mixing chamber, which are in thermal contact with what is trying to be cooled down. Then the ^{3}He will cross the phase boundary and join the ^{4}He-rich phase, restoring equilibrium. Finally, the atoms lost by the ^{3}He-rich phase are replenished by a constantly circulating flow of ^{3}He.

In detail, when the refrigerator is started the 1 K pot (a small container which is continually replenished with helium from the main bath) is used to condense the ^{3}He/^{4}He mixture into the dilution unit. Pumping on it temperature can be decreased to $\sim$1 K. It is not intended to cool the mixture enough to set up the phase boundary but only to cool it to 1.2 K. In order to get phase separation, the temperature must be reduced below 0.86 K (the triple critical point). The still is the first part of the fridge to cool below 1.2 K. It cools the incoming ^{3}He before it enters the heat exchangers and the mixing chamber, and phase separation typically occurs after a few minutes. Gradually, the rest of the dilution unit is cooled to the point where phase separation occurs.

It is important for the operation of the refrigerator that the ^{3}He concentration and the volume of mixture is chosen correctly, so that the phase boundary is inside the mixing chamber, and the liquid surface is in the still. The concentration of ^{3}He in the mixture is typically between 10 and 20%.

In a continuously operating system, the ^{3}He must be extracted from the dilute phase (to prevent it from saturating) and returned into the concentrated phase keeping the system in a dynamic equilibrium. The ^{3}He is pumped away from the liquid surface in the still, which is typically maintained at a temperature of 0.6 to 0.7 K. At this temperature the vapor pressure of ^{3}He is about 1000 times higher than that of ^{4}He, so ^{3}He evaporates preferentially. A small amount of heat is supplied to the still to promote the required flow.

The concentration of ^{3}He in the dilute phase in the still therefore becomes lower than it is in the mixing chamber, and the osmotic pressure difference drives a flow of ^{3}He to the still. The ^{3}He leaving the mixing chamber is used to cool the returning flow of concentrated ^{3}He in a series of heat exchangers.

The room temperature vacuum pumping system is used to remove ^{3}He from the still, and compress it to a pressure of a few hundred millibar. The gas is then passed through filters and cold traps to remove impurities and returned to the cryostat, where it is pre-cooled in the main helium bath and condensed in the 1 K pot. The primary impedance is used to maintain a high enough pressure in the 1 K pot region for the gas to condense. The experimental apparatus is mounted inside the mixing chamber, ensuring that it is in good thermal contact with the dilute phase. All connections to the room temperature equipment must be thermally anchored at various points on the refrigerator to reduce the heat load on the mixing chamber and give the lowest possible base temperature. If the experiment is to be carried out at higher temperatures, the mixing chamber can be warmed by applying heat to it directly, and a temperature controller can be used to give good stability.

Continuous-cycle dilution refrigerators are commonly used for low temperature physics experiments. Temperatures below 2 mK can be achieved with the best systems. In our cryostat, the lowest temperature the system is able to stabilize in around 60-80 mK.

6.1.2 Experimental setup

In order to perform the transport measurements a special sample holder is built to fit the dilution probe and keep the sample properly protected.

The TiN sample is fixed on a plastic plate with GE-varnish and set on a pin chip (see Fig. 6.3) that fits its counterpart placed on the probe which connects to the electrical box.

Setting the sample on the chip helps welding it, process which is extremely delicate. Each of the contacts, 1 - 10, shown in the sketch of Fig. 5.3 is welded to the contacts on the chip using silver wires and indium instead of tin. The procedure, that needs the use of a binocular lens, is the following:

1. After preparing the chip so that it can fit the sample space inside the cryostat, some tin is soldered on its contacts.

2. The soldering iron is prepared by cleaning its tip to make sure there is not tin left and covering it with indium. Indium oxidizes easily so the tip has to be scratched until there is only a thin film left.

3. A small amount of indium is placed on each contact of the Hall bridge shown in Fig. 5.3.

4. The wires are prepared by cutting them to the desired length, bending each one to get the better shape to make the welding easier and putting some indium on their edges.

5. One edge of the wire is soldered to the indium placed on each contact of the sample.

6. With the help of a toothpick and tweezers, the other edge of the wire is put in contact with the chip trying not to release the solder on the sample.

7. The silver wire is welded to the chip contact.

8. The extra wire is cut off and the procedure is repeated for all the contacts.

When all the wires are welded, the device is placed at the lower part of the probe and an extra thermometer is placed near the sample to track temperature changes. Next, all is covered with a plastic protection and wrapped with teflon tape. Finally all the contacts are checked and a measurement is registered at room temperature.

As it has been explained, two parts can be differentiated in this sample: one half is a plain thin film ($fA, fB...$) and the other half has a squared lattice of holes ($pA, pB...$). Here f or p indicate plain film or perforated part respectively, while A, $B...$, represent the evolutive state of the sample. Between each pair of consecutive states the sample is subjected to a thermocycling process, consisting in heating the sample in open air by contact with a soldering iron up to 370°C for several minutes. This process causes

Contacts	B $R(\mathrm{k}\Omega)$	C $R(\mathrm{k}\Omega)$	C_2 $R(\mathrm{k}\Omega)$
12-11	87.3	89.4	91.1
12-2	53.9	55.4	58.3
2-3	70.6	72.0	73.9
3-1	108.7	110.8	113.0
1-6	110.3	113.1	115.5
6-11	67.7	69.4	70.7
11-18	67.5	69.2	70.5
18-17	102.0	105.2	107.2
17-14	98.0	100.9	102.6
14-13	72.1	73.9	75.3
13-12	57.4	58.5	59.8

Table 6.1: Resistance between contacts for stage B, stage C just after the thermocycling process and stage C six months later, just before measuring. In this case the thermocycling process was for 80 seconds up to 370°C.

an increase of disorder and sample resistance, so the sample becomes more insulating each time and, therefore, this changes the results of transport measurements.

Stage A has been measured at the Institute of Semiconductor Physics in Novosibirsk (Russia) under the supervision of Dr. Tatyana Baturina. Stages B and C have been measured at the laboratory of Grup de Magnetisme in Barcelona.

After the thermocycling process some contacts may have to be welded again repeating the procedure explained above. After that, electrical contacts are always rechecked. The resistance evolution of the sample after the thermocycling can be found in Table 6.1.

A sketch of the contacts is shown in Fig. 6.4. Both, I_{ac} and I_{dc} are applied through 11-12. There are two pairs, 13-14 and 2-3, which correspond to the film, and two more, 17-18 and 1-6, for the perforated sample.

The measurement is simultaneous for the plain and perforated parts, enabling the study under the exact same conditions for both parts. Moreover, the current passing through all the sample is the same because plain and perforated parts are in series. The extra contact pair is in case there is an electrical problem in order to be able to continue performing the experiments instead of being forced to open and fix it, losing time, helium and environmental conditions.

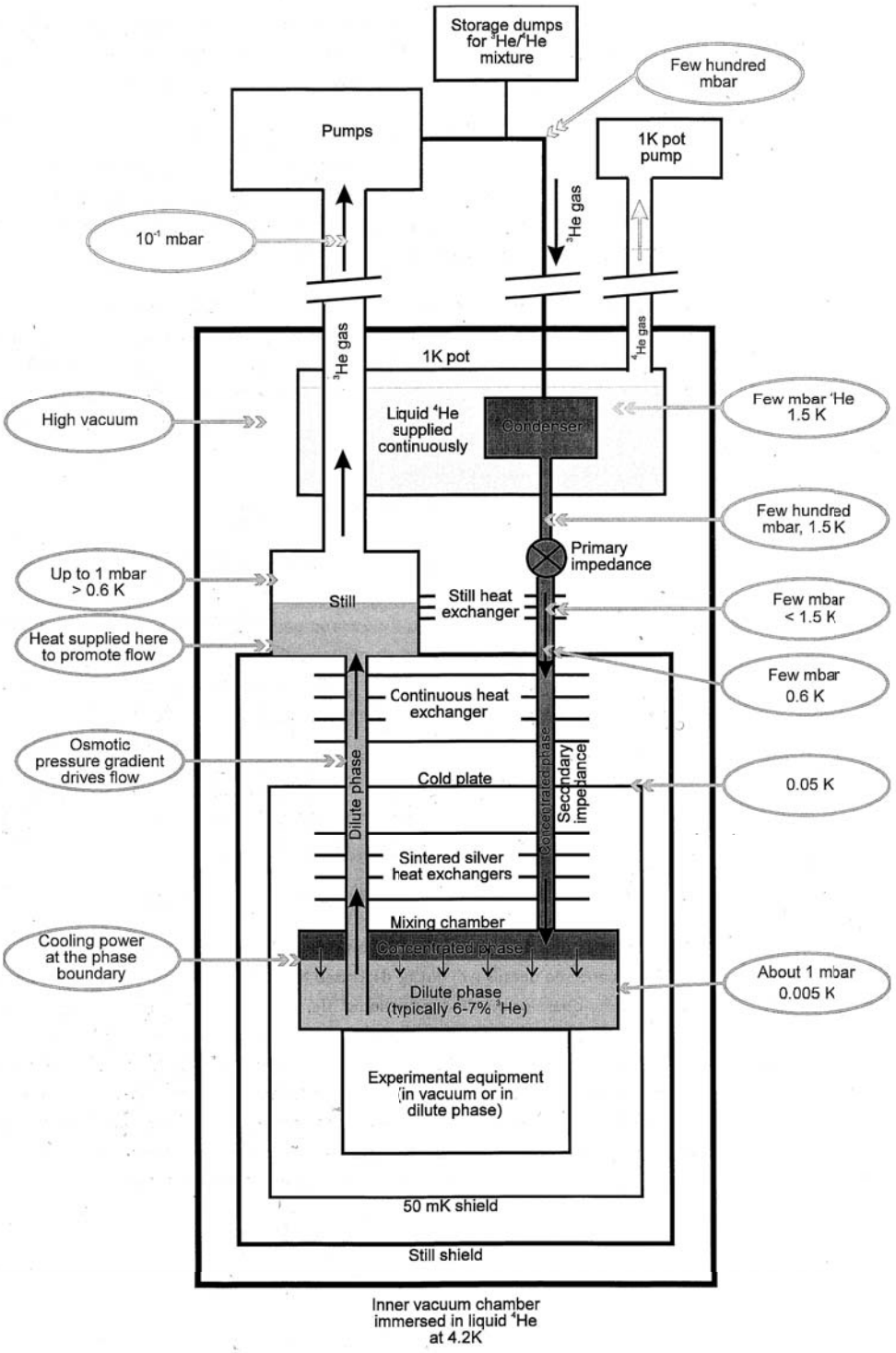

Figure 6.1: Schematic diagram of a dilution refrigerator.

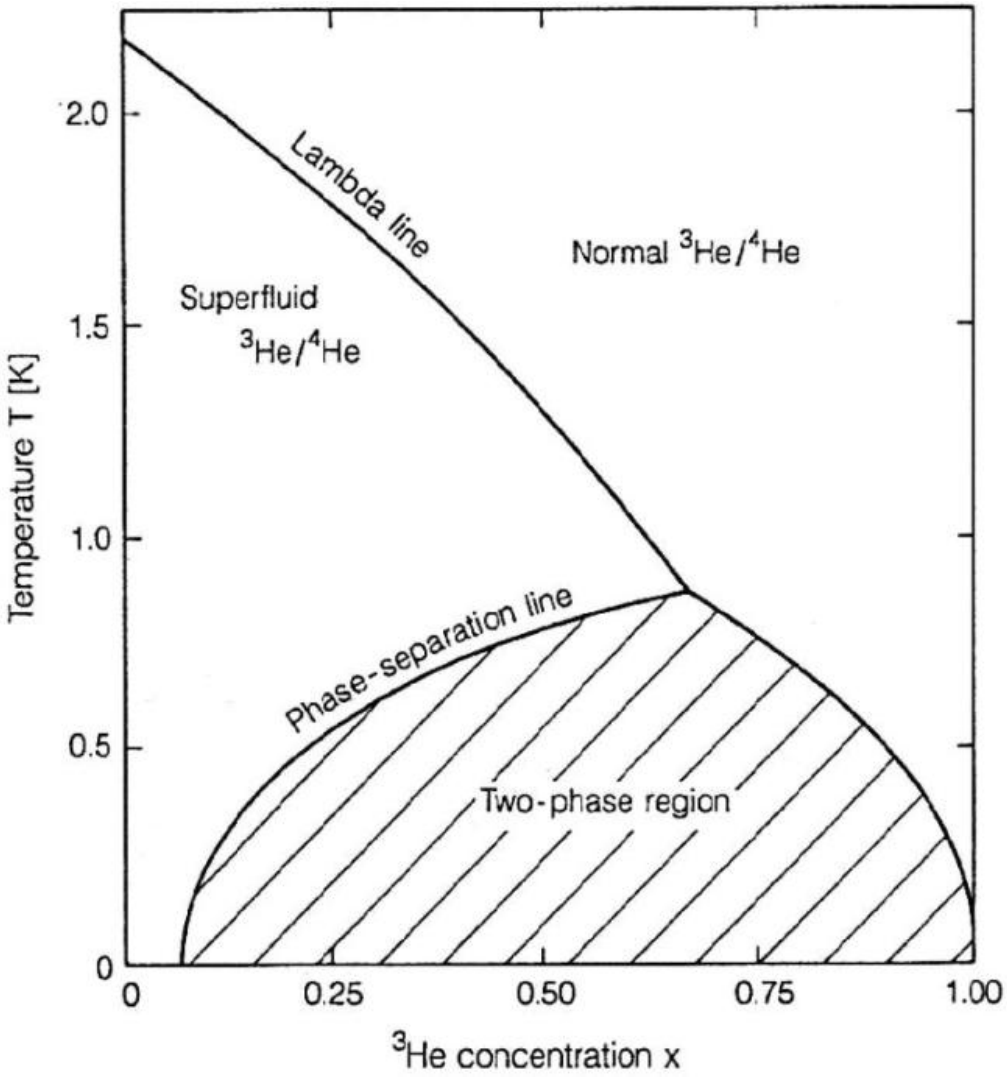

Figure 6.2: Phase diagram of ^{3}He/^{4}He mixtures.

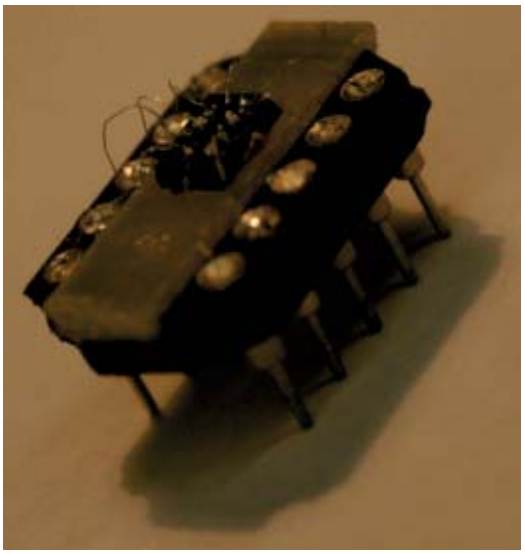

Figure 6.3: Experimental setting for transport measurements of a TiN sample. The sample is set on a device fixed on a chip in order to weld easily the contacts. The device is placed at the lowest part of the probe properly protected.

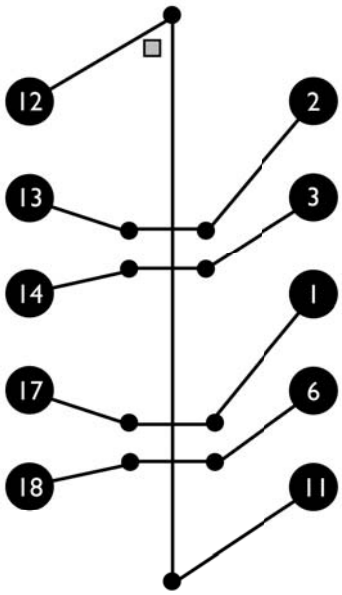

Figure 6.4: Sketch of the electrical contacts of the sample. Both, I_{ac} and I_{dc} are applied through 11-12, while 13-14 and 2-3 correspond to the film, and 17-18 and 1-6 correspond to the perforated sample.

6.2 Experimental procedure and results

After building all the sample setup, the probe is introduced inside the dilution refrigerator. This is a slow and delicate procedure. Proceeding in an inappropriate way would cause the lose of the mixture which would have to be condensed again meaning two days of work. Measurements as a function of T are performed while introducing the probe in order to be able to register temperatures over the dilution working range.

The system is connected to three lock-in amplifiers (see Fig. 6.5). With one of them an ac current is applied to the sample through a resistance of 80 MΩ and with the other two the voltage response is measured for both the plain film and the perforated part (V_{1x}, V_{1y}, and V_{2x}, V_{2y} respectively). Following this procedure, the variation of the current-voltage characteristic is measured ($\mathrm{d}V/\mathrm{d}I$ defined as $2R_{\square}$, because each sample is composed of 2 squares).

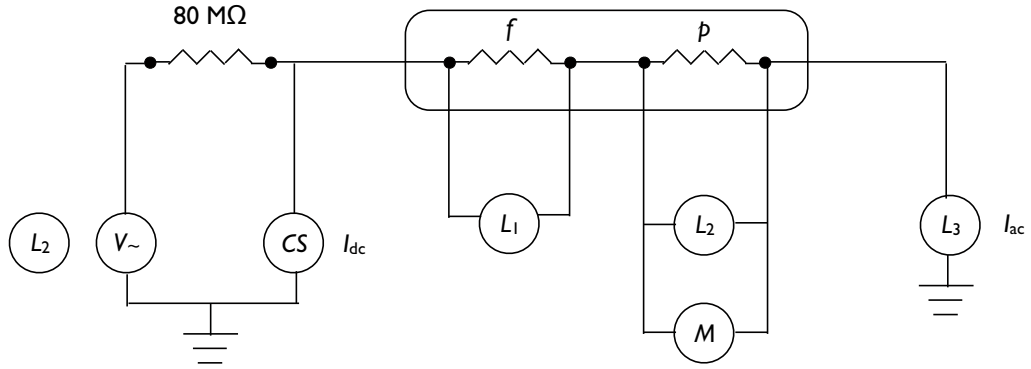

Figure 6.5: Sketch of the measurement electrical circuit. Lock-in 1 (L_1) and 2 (L_2) measure plain and perforated films respectively. L_2 applies V_{ac} through a 80 MΩ resistance getting the I_{ac} that crosses the samples. Lock-in 3 (L_3) measures I_{ac}, CS is a current source which applies a I_{dc} when is needed and M is a multimeter measuring the dc voltage of the perforated part.

$R_{\square}$ can be understood as a measurement of the sample disorder. It is defined considering an infinitesimal width (d), dividing the sample in squares, being $R_{\square}$ the resistance of each of these squares ($R = R_{\square}\frac{L}{\delta}$, where L is the length of the sample and δ the infinitesimal cross-section). This is possible because the sample studied can be considered a quasi-2D system characterized by $l < d < \xi$, where ξ is the coherence length and l the electron mean free path. In this case the Cooper pair motion is restrained enabling the possibility of measuring the superconductor-insulator transition (SIT) as it

will be shown at the end of this thesis.

All system parameters (H, T_c, I_{dc}, I_{ac} and V_i) are controlled by a computer and the measurements are automated by using a software specially programmed in LabVIEW for this reason (see Fig. 6.6). When it is necessary extra sources are added to the device.

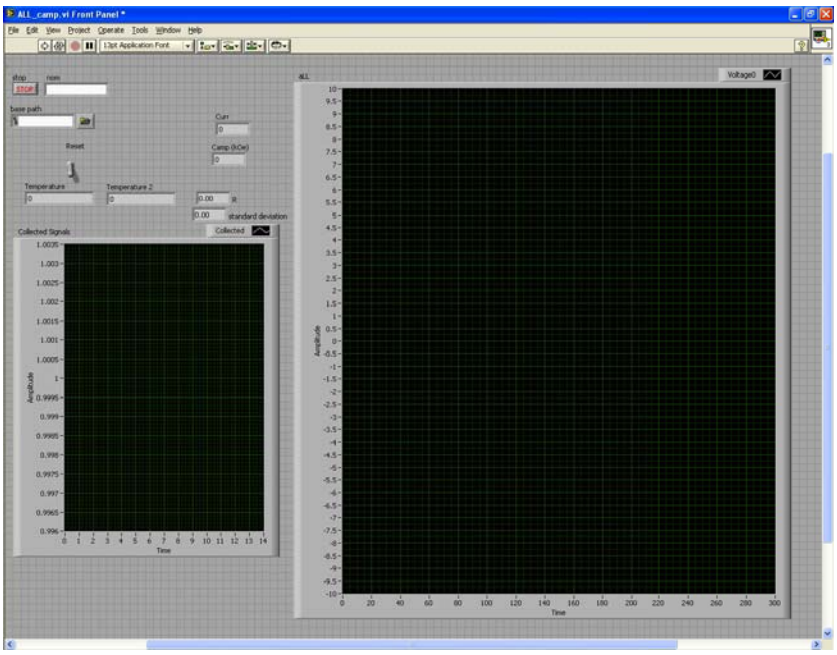

Figure 6.6: Page print of the LabVIEW program that controls the experimental measurements.

6.2.1 $R_\square$ as a function of temperature

The first measurements performed have been as a function of the temperature in absence of magnetic field, remembering that some values were already registered while introducing the probe in the dilution refrigerator in order to get data for temperatures above the working dilution range.

Results for the as-cast and perforated films are shown in Figs. 6.7 and 6.8, respectively. Fig. 6.7 shows that the change between fA, fB and fC is relatively small. As it was expected, $R_\square$ increases slightly from fA to fB to fC and the superconductor transition is shifted to lower temperatures, i.e. the increase of disorder lowers the transition temperature.

As it will be discussed in the next section, using the quantum corrections to conductivity (QCC) which govern this kind of samples, results can be

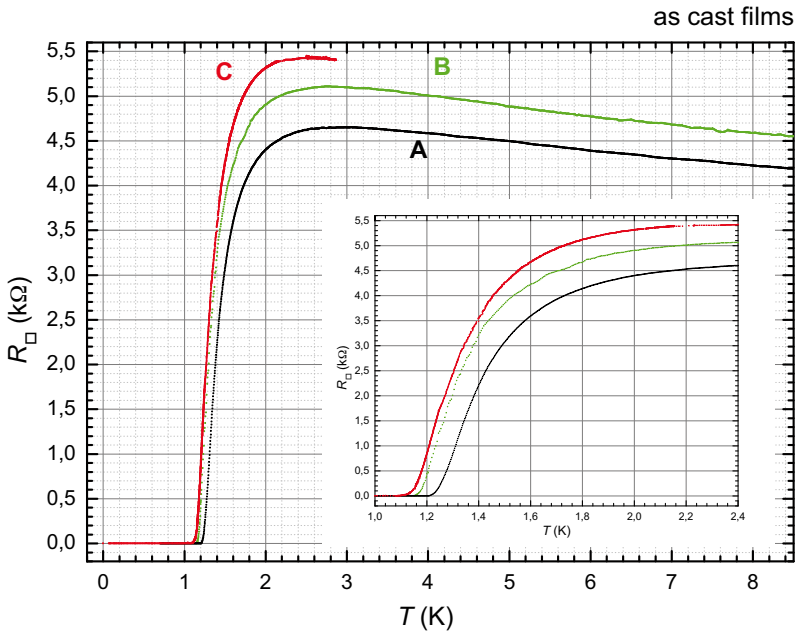

Figure 6.7: Comparison of the results of the transport measurements at zero magnetic field as a function of temperature for the three evolution states of the as-cast thin film: fA, fB and fC. The inset is a magnification of the region close to the transition.

fitted with the theory and obtain the values of T_c shown in Table 6.2 with great accuracy.

	fA	fB	fC
T_c (K)	1.15	1.09	1.08

Table 6.2: Table of the values obtained for T_c after fitting the experimental data with the quantum corrections theory.

On the other hand, the shift of T_c experienced by the perforated part after every evolution of the sample is more evident in Fig. 6.8. The increase in $R_\square$ and the shift of T_c are greater than expected for the QCC prediction. It is important to notice also that at $T < T_c$, although sample pB is already in the superconductor state, it has a remanent resistance of almost 6 kΩ (see Fig. 6.8). This effect could be explained as a coexistence of islands of superconducting and normal state, giving as a result this remanent resistance,

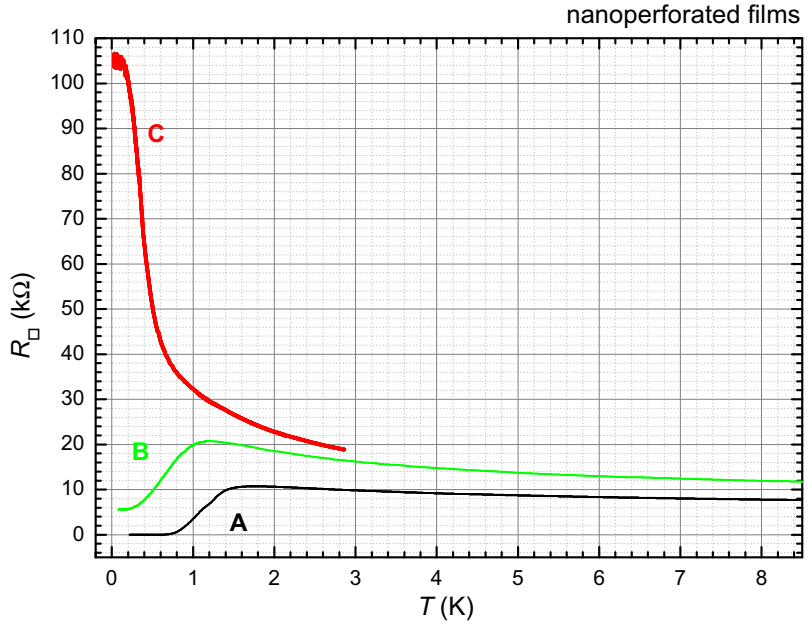

Figure 6.8: Comparison of the results of the transport measurements at zero magnetic field as a function of temperature for the three evolution states of the perforated film: pA, pB and pC.

although the macroscopic behavior is that of a superconductor.

For sample pC it is observed that as the temperature decreases $R_\square$ increases in a colossal way taking the sample into an insulator state instead of a superconductor state. It will be proved in the next lines that the sample has a superconductor behavior too, so this could be explained as the sample being in an insulator state but containing islands of material in a superconductor state.

A determination of T_c by fitting the experimental data to a theoretical expression in the case of the perforated part is not possible yet because there is still no model that explains its behavior.

Measurements as a function of the temperature for different magnetic fields have also been performed (see Figs. 6.9 and 6.10 for samples fB and pB respectively). It can be seen here that the field induces the SIT, drawing a fan-shaped plot where $R_\square$ decreases with T for a SC behavior and $R_\square$ increases with T for an insulator, skipping the metallic state where $R_\square$ would stay constant. This is particularly evident in the case of the perforated

sample, which for a field slightly above 3 T reaches a $R_{\square}$ of about 65 kΩ, beyond the value that would be exhibited if the change was simply due to quantum correction effects. [40]

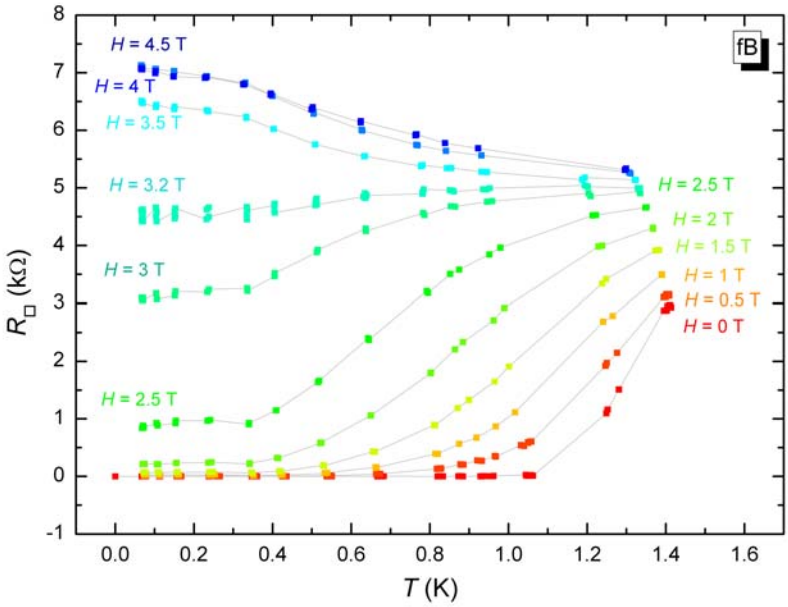

Figure 6.9: Results as a function of temperature for different magnetic fields for sample fB.

Results are even more abrupt for sample C (see Figs. 6.11 and 6.12 for samples fC and pC respectively). The magnetic field increases the square resistance to really high values specially for the perforated part as it can be observed in Fig. 6.12, where a value of almost 350 kΩ is reached for $R_{\square}$.

6.2.2 $R_{\square}$ as a function of magnetic field

The next set of results presented are measurements as a function of the external magnetic field applied perpendicular to the plane of the sample for different temperatures. The data have been registered by setting a temperature, waiting a certain time for it to stabilize and sweeping the magnetic field from -1 T to 5 T. When a set of measurements has been performed the temperature is shifted to the next value in order to repeat the process.

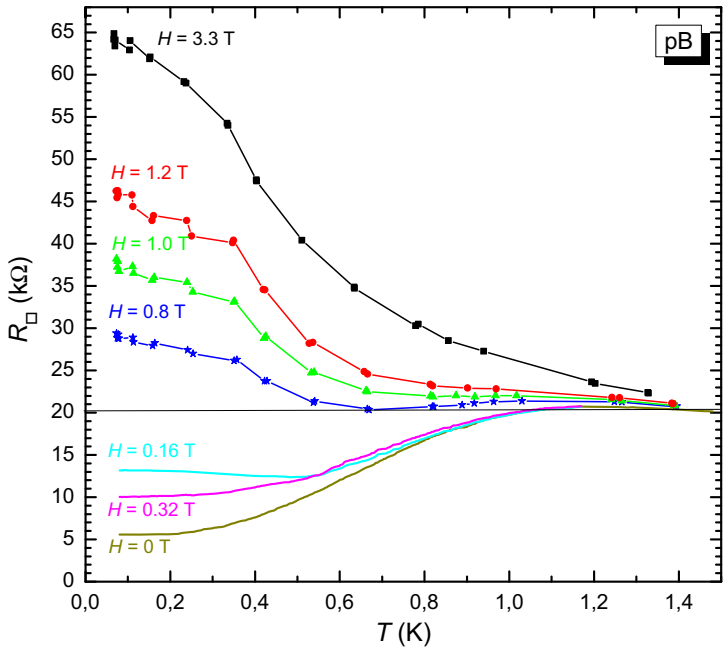

Figure 6.10: Results as a function of temperature for different magnetic fields for sample pB. The solid line corresponds to the value of resistance in the normal state.

The evolution of $R_\square$ with the magnetic field for different T values is presented in Fig. 6.13 for the plain films and in Fig. 6.14 for the perforated parts of samples A, B and C.

The results for the plain films (see Fig. 6.13) show how all the data for the different temperatures intersect at one point. In the framework of the theory for these samples, this defines a critical magnetic field and a critical resistance, whose values are 3.27 T and 5 kΩ, respectively, for sample fB, and 3.27 T and 6 kΩ, respectively, for sample fC. Unlike other superconductors [41], in these samples, the critical field as it has been defined above is independent of temperature. The theory indicates that this critical point has a certain shift between evolutionary stages of the sample. As it can be seen by comparing graphs, this is indeed so, and in the next section it will be analyzed in more detail.

Another feature of these samples, that can be seen in the plain film and more important in the perforated, is what is known as negative magnetoresistance (MR), i.e., as the magnetic field is increased to high fields, all the

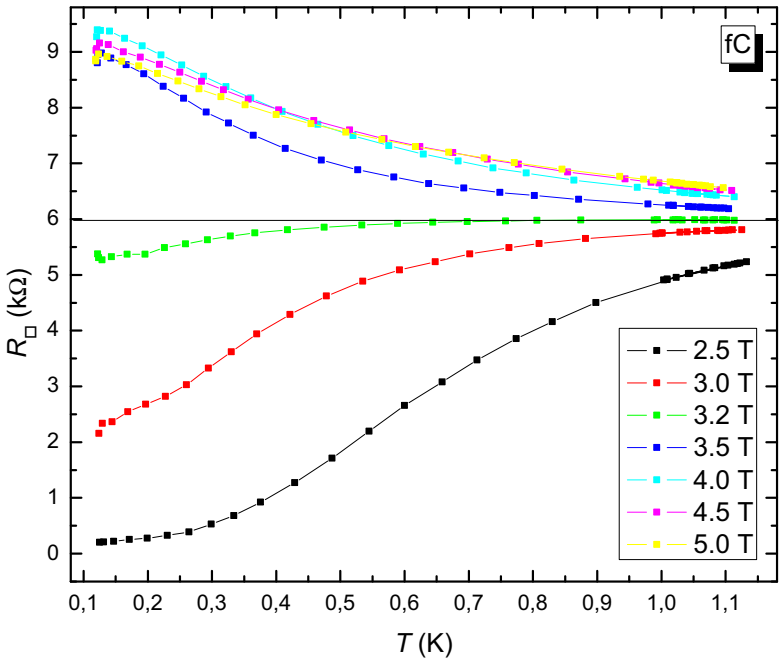

Figure 6.11: Results as a function of temperature for different magnetic fields for sample fC. The solid line corresponds to the value of resistance in the normal state.

curves decrease from a $R_{\square_{max}}$ slightly beyond H_c towards a common value. These are signs that are related to the SIT. This behavior is more exaggerated in sample C than in B, and even more than in A.

For perforated samples, commensurability effects are observed for a magnetic field (see Fig. 6.14) at which the vortex lattice spacing matches the hole lattice period. The characteristic feature of this result is the wide temperature range where these oscillations are observed. We will come back to this in the next section.

To conclude this point, it is remarkable the increase in resistance between sample A and C reached for some field, arriving in the latter case almost to 350 kΩ and making the SIT more evident. Negative MR at large fields is also much more marked in sample C, as well as the remanent resistance for zero magnetic field, showing how the increase of disorder of the sample affects the transport measurements and induces the SIT.

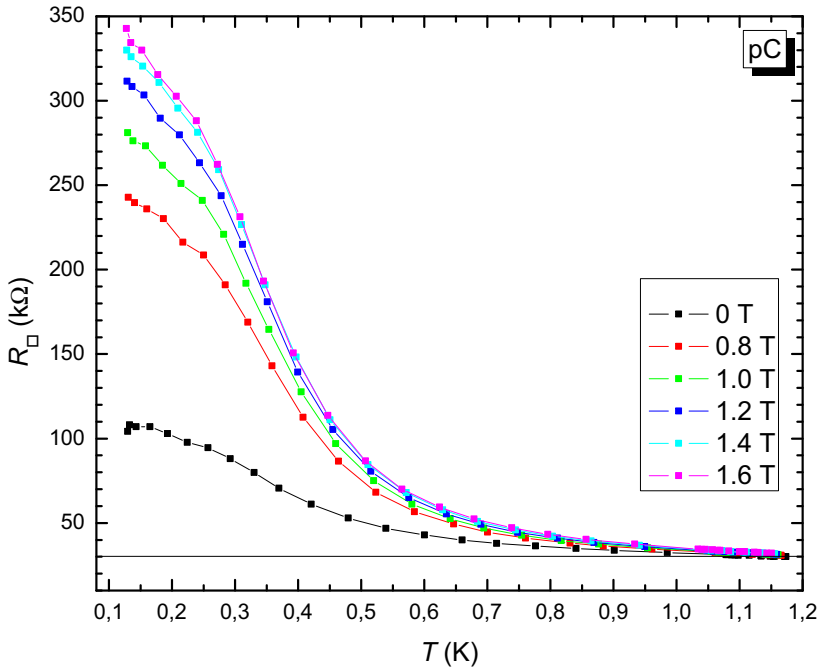

Figure 6.12: Results as a function of temperature for different magnetic fields for sample pC. The solid line corresponds to the value of resistance in the normal state.

6.2.3 $R_\square$ as a function of dc current

In the last block of measurements, a dc current is applied along the sample. For a stabilized temperature, the current is swept for different magnetic fields, gathering a huge density of data. Measurements have been performed for different temperatures and magnetic fields, analyzing how the change of one of the variables induces the SIT, for both T and H sweeping I_{dc}. Fig. 6.15 shows results for sample fB and Fig. 6.16 for pA and pB.

For this data, the SIT can be observed as the change from a minima (in the superconductor state) to a maxima (in the insulator state) around I_{dc} = 0. The critical current for fB is ∼2000 nA, although this is out of the range of this graph in order to be able to study the changes around $I_{dc} = 0$ in detail.

To see exactly how this transition occurs, the curvature of the well or

the peak is studied for samples fB and pB as the second derivative of the resistance around $I_{dc} = 0$, $d^2R_\square/dI^2$. This is plotted in black in the first and third graphs of Fig. 6.17 as a function of the magnetic field, while the same dependence is plotted in red for $R_\square$. The first graph shows how the point of zero curvature coincides with the critical field. The curve shows a single change of sign in the case of the as-cast thin film, but several sign changes for the perforated sample, which fits the matching effects detected in the magnetic field measurements. The second graph shows the curvature for several temperatures for fB, and again all results converge at the same point, the critical field.

In the case of sample C, the profile obtained is very similar to the ones seen before for sample B and it is presented in Fig. 6.18. As it had been done with sample B, measurements were repeated for several temperatures and magnetic fields. Results for sample pC as a function of I_{dc} at different temperatures are shown in Fig. 6.19. In obtaining these data, small oscillations for certain values of the current were detected. After a long process to reduce experimental noise or possible geometrical effects that may be affecting the measurements the study of these oscillations for different temperatures was performed. A deep study of these peaks and their evolution with T and H will be presented in the next section.

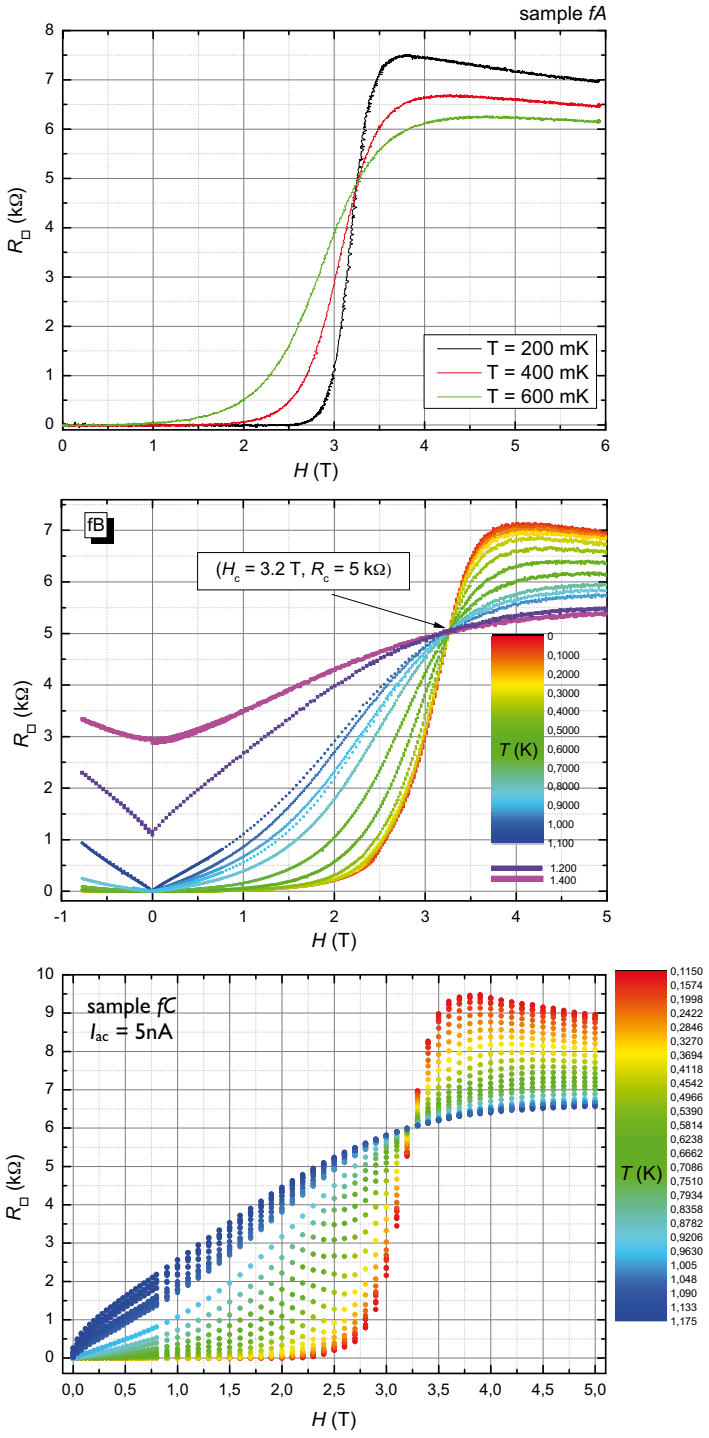

Figure 6.13: Results for the plain films as a function of magnetic field for different temperatures. From top to bottom, the panels correspond respectively to fA, fB and fC.

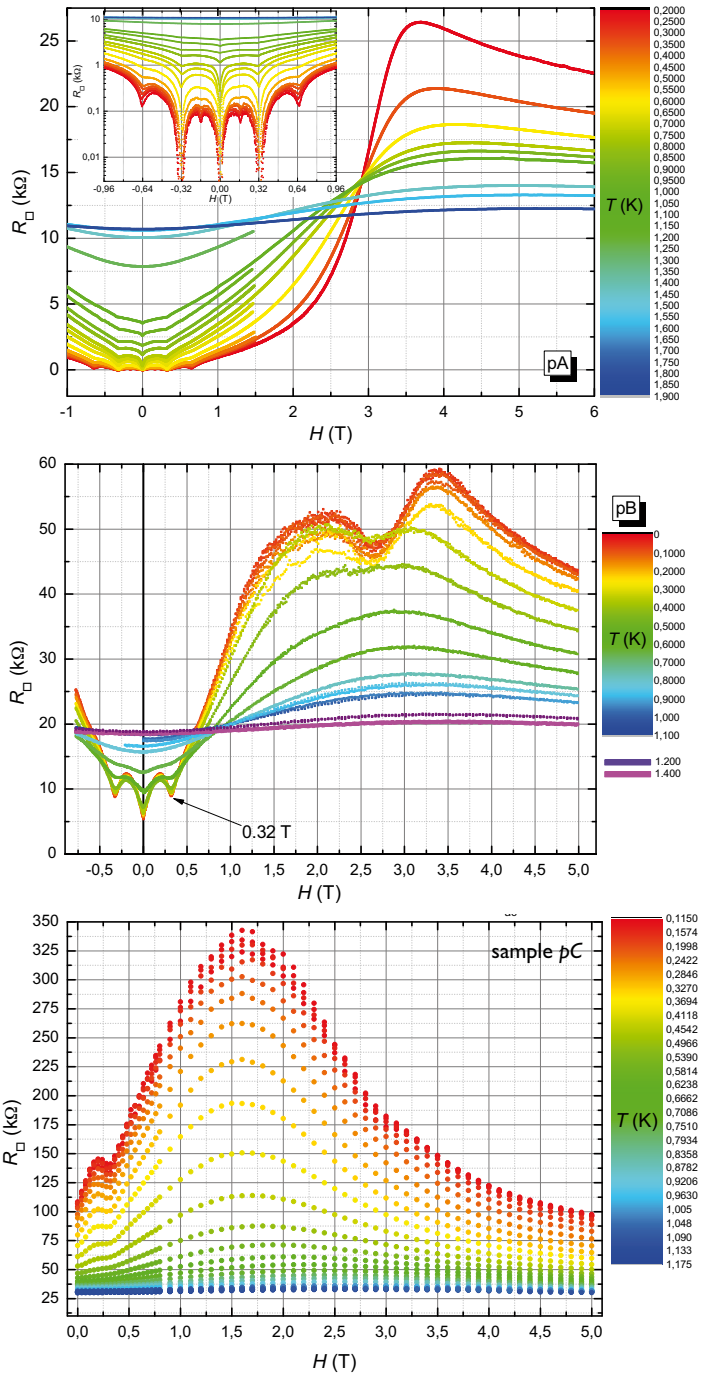

Figure 6.14: Results for the perforated parts as a function of magnetic field for different temperatures. From top to bottom, the panels correspond respectively to pA, pB and pC.

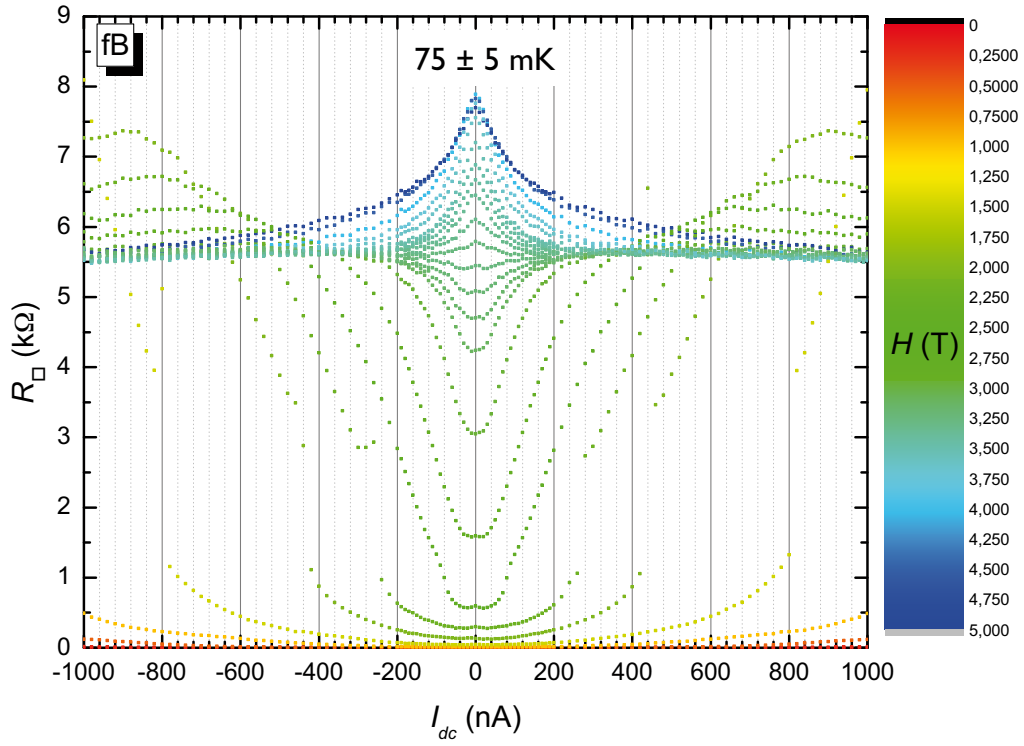

Figure 6.15: Measurements as a function of the dc current for different magnetic fields for sample fB at $T = 75 \pm 5$ K.

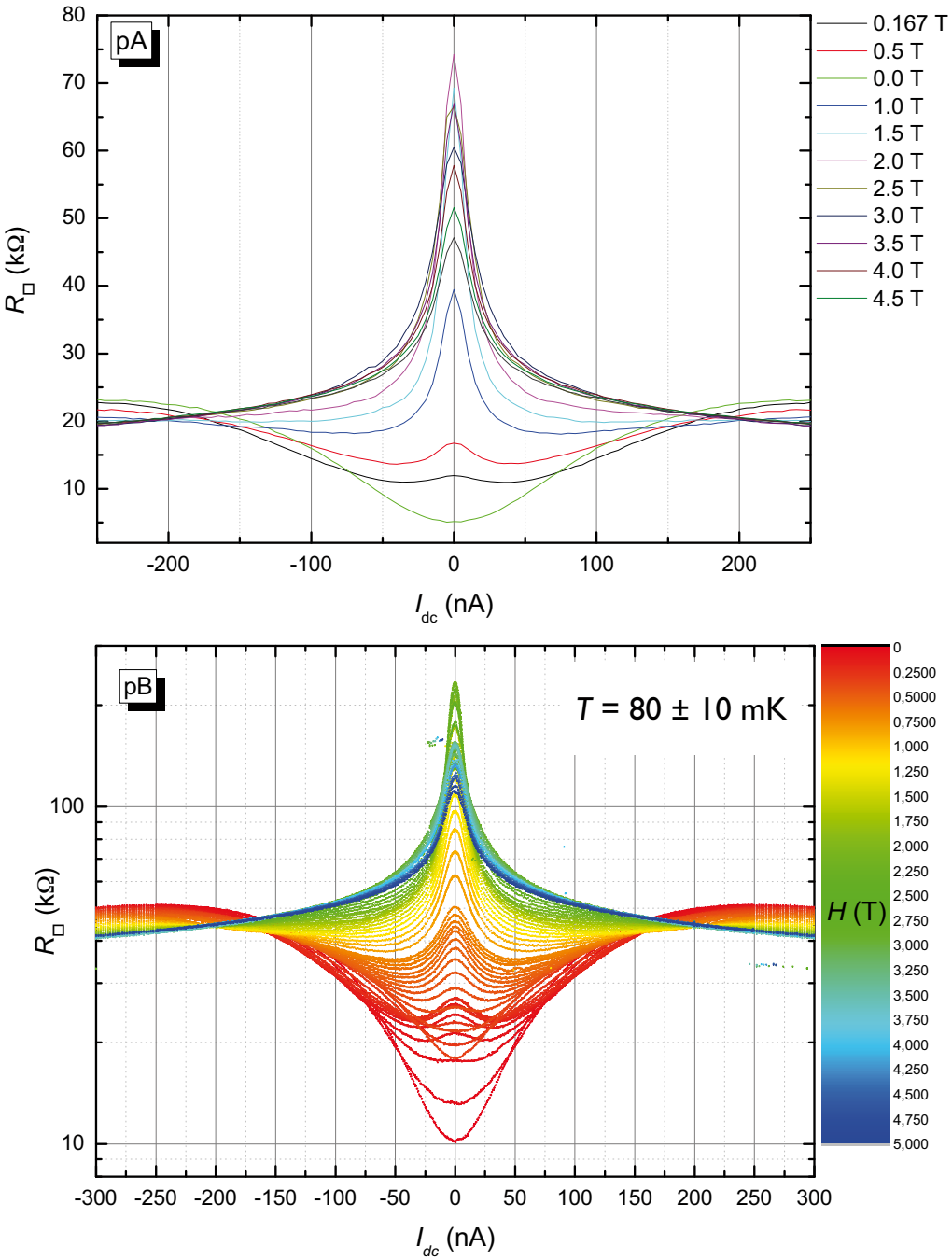

Figure 6.16: Measurements as a function of the dc current and different magnetic fields for samples pA (top) and pB (bottom) at $T = 80 \pm 10$ K.

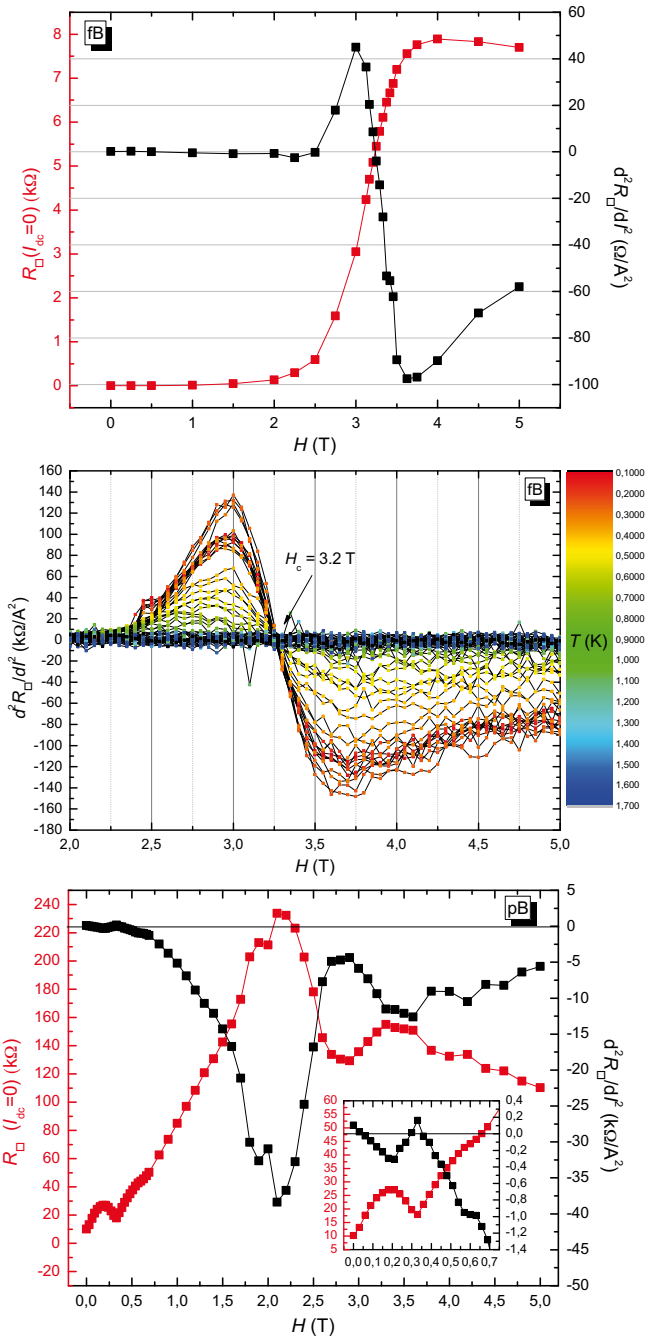

Figure 6.17: SIT studied as the curvature around $I_{dc} = 0$. The first and second graphs correspond to fB and the third to pB. $d^2R_\square/dI^2$ is plotted in black in the first and third graphs as a function of the magnetic field, while the same dependence is plotted in red for $R_\square$. The second graph shows how the curvatures of fB for several temperatures converge at the same point, the critical field.

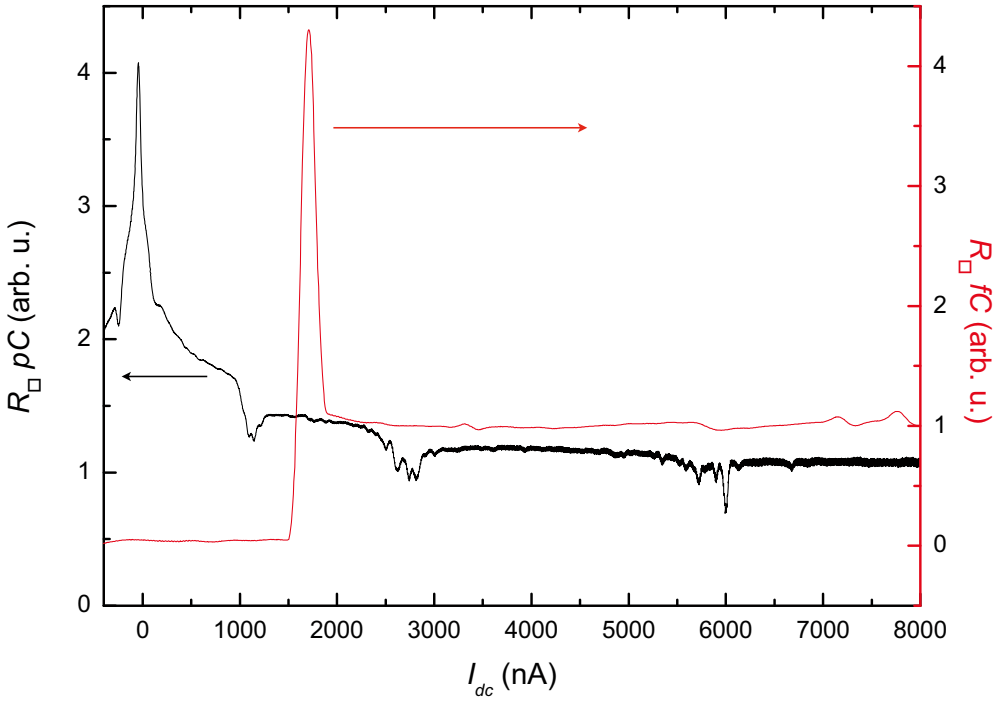

Figure 6.18: Measurements as a function of the dc current for sample fC (red) and pC (black).

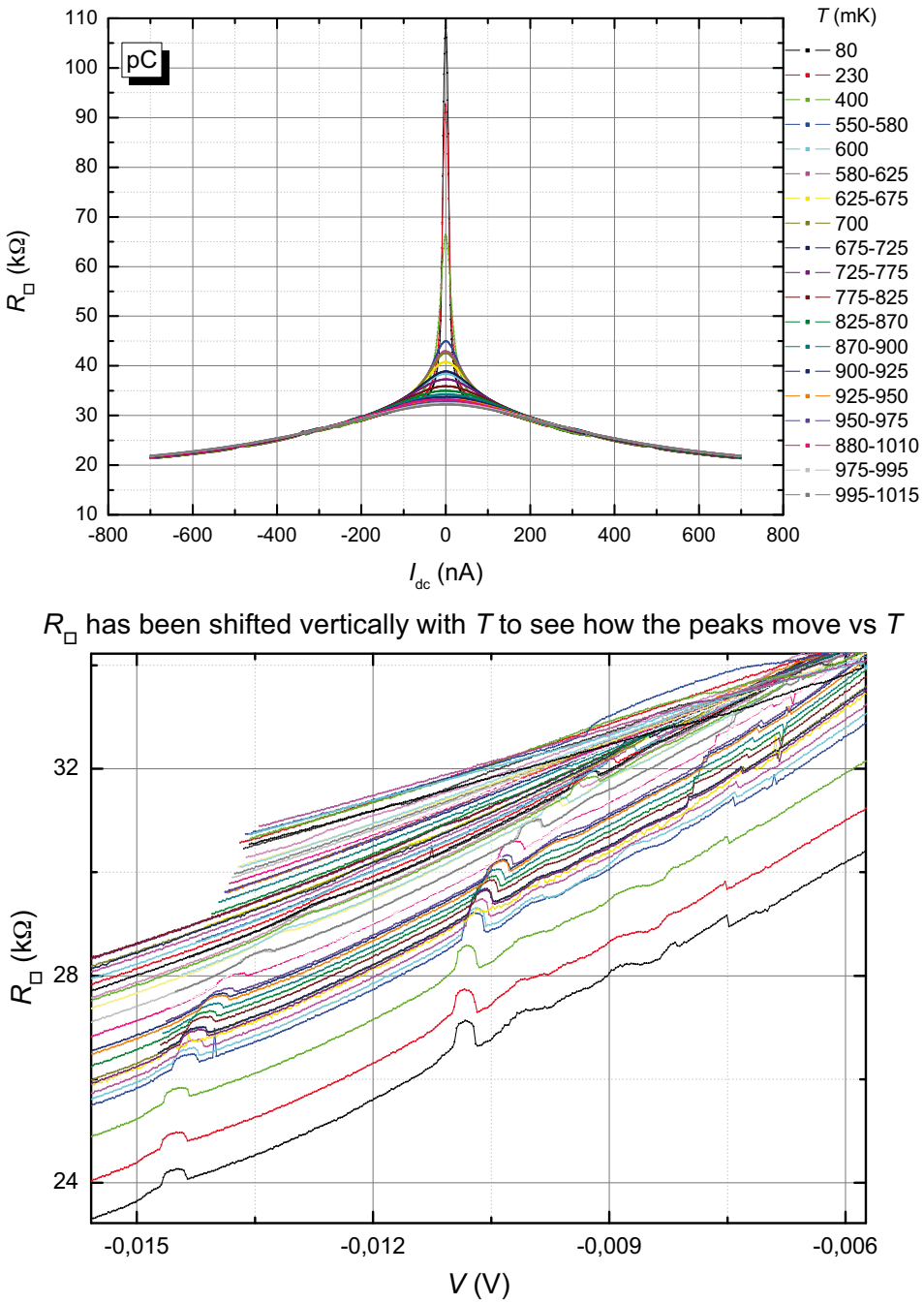

Figure 6.19: Top: Measurements as a function of the dc current at different temperatures for sample pC. Bottom: Zoom of the peaks in the $I-V$ characteristics of sample pC. This result is presented as a function of the voltage (that comes from integrating $\mathrm{d}V/\mathrm{d}I$ vs I) to simplify further analysis. The curves have been shifted along the vertical axis in order to see the peaks easily.

Chapter 7

Discussion

Measurements as a function of the temperature, the magnetic field and a dc current along the sample have been performed simultaneously on the as-cast thin film and the perforated giving as a result a huge amount of data summarized and presented in previous chapters of this thesis.

This section attempts to describe the foundation of some of these results and to establish some ideas to try to understand mainly the behavior of the perforated samples for which there is still no solid theory that describes them.

7.1 Superconductor vs superinsulator

Electrical resistance in metals arises because electrons moving through the metal are scattered due to deviations from translational symmetry. These are produced either by impurities, giving rise to a temperature independent contribution to the resistance, or by the vibrations of the lattice in the metal.

In a superconductor (SC) below its critical temperature, there is no resistance because these scattering mechanisms are unable to impede the motion of the current carriers. As a negatively-charged electron moves through the space between two rows of positively-charged atoms, it pulls inward on the atoms of the lattice. This distortion attracts a second electron to move in behind it. Thus an electron in the lattice can interact with another electron by exchanging a phonon.

Then superconductivity is the ability of certain materials to carry loss-free current by the interaction of conducting electrons with the vibrational motion of atoms. [42] The mediating action of atomic vibrations induces attraction between electrons with opposite spins and momenta, and causes them to combine into bound pairs called Cooper pairs. Being bosons, Cooper pairs condense at the lowest possible quantum state. To break a Cooper pair and

remove the two resulting unbound electrons from the condensate, one has to spend the energy 2Δ, the quantity Δ being called the superconducting gap, and this can be done by increasing temperature, magnetic field or current.

On the contrary, a superinsulator (SI) is a material that at low temperatures under certain conditions has an infinite resistance and no current will pass through it. [43] Both superconductivity and superinsulation are caused by the pairing of conduction electrons at low temperatures into Cooper pairs. In superconductors, all the pairs move in unison, allowing current without resistance. In superinsulators the Cooper pairs avoid each other, preventing current from flowing.

Several experiments [44–46] have shown in the last years that in thin SC films, disorder enforces the droplet-like electronic texture (superconducting islands immersed into a normal matrix) and that tuning disorder drives the system from superconducting to insulating behavior. A distinct state is formed in the vicinity of the transition [46]: a Cooper-pair insulator, with thermally activated conductivity. It results from synchronization of the phase of the superconducting order parameter at the islands across the whole system [47]. At a certain finite temperature, a Cooper-pair insulator undergoes a transition to a superinsulating state with infinite resistance. The SI state is dual to the SC state: it is destroyed by a sufficiently strong critical magnetic field, and breaks down at some critical voltage that is analogous to the critical current in superconductors. A phase diagram showing parallels with superconductivity is shown in Fig. 7.1 (his figure has been extracted from [43].)

This dual similarity extends even further. The Joule loss $P = IV$, which is exactly zero in the SC state, is also exactly zero in the SI. Whereas the absence of Joule loss in a SC is the result of the non-dissipative flow of the current and thus the lack of the voltage drop $V = 0$, the zero Joule loss in a SI is ensured by the absence of the current at $V < V_T$, where V_T is the threshold voltage.

In this PhD thesis experimental evidence of this transition in titanium nitride films is presented. The superconductor-insulator transition (SIT) is a phase transition of the second order and is driven by fluctuations of quantum nature. The superconducting phase is considered to be a condensate of Cooper pairs with localized vortices, and the insulating phase is a condensate of vortices with localized Cooper pairs [43].

The SIT has been studied by increasing the disorder of the sample and the application of an external magnetic field and dc current.

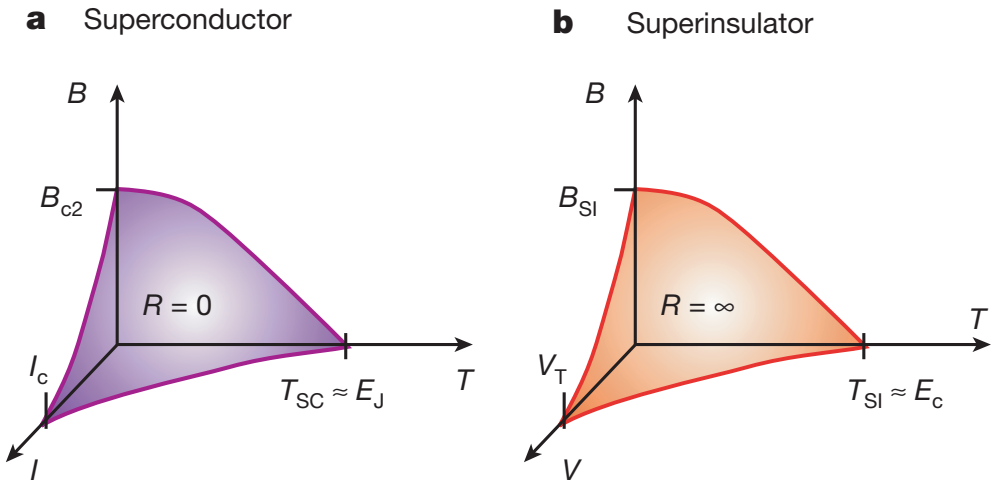

Figure 7.1: Sketch of dual-phase diagrams for a superconductor and a superinsulator. **a)** Magnetic-field-temperature-current *(B-T-I)* superconductor phase diagram. **b)** A dual-phase diagram for a superinsulator is obtained from the superconductor phase diagram by replacing current (I) by voltage (V). The threshold voltage V_T, the maximal voltage at which a superinsulator can retain a zero-conductivity state, is equivalent to the critical current of a superconductor. The critical temperature for a superconductor T_{SC} maps onto the critical temperature of the "normal" insulator-superinsulator transition T_{SI}.

7.2 As-cast thin film

7.2.1 Determination of T_c by quantum corrections

First observation of superconductivity was performed by H. Kammerlingh Onnes in 1911. It was described by a sudden and sharp transition between two states of matter at a critical temperature at which the electrical resistivity of a metal dropped to zero.

During some decades the transition was described in all cases by the Bardeen-Cooper-Schriefer (BCS) theory, but it has long been known now that in thin films the transition into a superconducting state occurs in two stages: first, with the decreasing temperature, the finite amplitude of the order parameter forms at the superconducting critical temperature T_c; second, a global phase-coherent state establishes at lower temperature T_{BKT} (the temperature of the Berezinskii-Kosterlitz-Thouless (BKT) transition) [48,49].

It is known that in 2D systems vortices can exist either as bound vortex-antivortex pairs or as dissociated free vortices and antivortices (see [50–53]

for a review). In the temperature scale these two phases are separated by T_{BKT}. Vortices in a superconductor appear when sufficiently strong magnetic field is applied. Nevertheless in the case of 2D superconductors vortices may appear as the result of thermal fluctuations. In absence of magnetic field the densities of vortices and antivortices are equal.

At $T > T_{BKT}$ in a superconductor there exists some density of decoupled vortices and antivortices. When the supercurrent flows they move in opposite directions and transfer magnetic flux. As a result, the electric field, proportional to the density of decoupled vortices, induces in the system the appearance of the resistive state. Hence the decoupling of the vortex-antivortex pairs above T_{BKT} leads to the breakdown of superconductivity and thus T_{BKT} has to be considered as the true transition temperature to the superconducting state. Below T_{BKT} all vortices and antivortices are bound and can not transfer magnetic flux.

One can easily recognize that the value of T_{BKT}, separating the region where vortices are bound in pairs from that where they are free, must be lower than the BCS (mean field) critical temperature T_{c_0}, the temperature at which the vortices disappear. Nevertheless the difference between T_{c_0} and T_{BKT} is of the order of the Ginzburg-Levanyuk number, $Gi_{(2)}$ (a relation between the found Ginzburg-Levanyuk number in the dirty 2D case with the dimensionless conductance can be written as $Gi_{(2,d)} \approx \frac{1}{23G_\square}$ where $G_\square = \frac{\hbar}{e^2 R_\square}$). Introducing the constants it is obtained that $Gi_{(2,d)} \approx 0.1058 \cdot 10^{-4} R_\square$ so even if the range analyzed had a change for $R_\square$ of several kΩ the value for $Gi_{(2,d)}$ and so the difference between T_{c_0}, T_c and T_{BKT} would be only of a few hundredths or tenths of kelvin (see reference [54] for calculations).

Following this reasoning, the transition is divided into zones, which are presented in the sketch in Fig. 7.2 and listed below:

1. Below T_{BKT}: SC state
2. Between T_{BKT} and T_c: Resistive state
3. Between T_c and T_{c_0}: Quantum fluctuation region
4. Above T_{c_0}: Vortices desappear

Fig. 16.1 from reference [54] presents the temperature dependence of the superfluid density and the average square of the order parameter in the vicinity of the transition and the relative position of different critical temperatures.

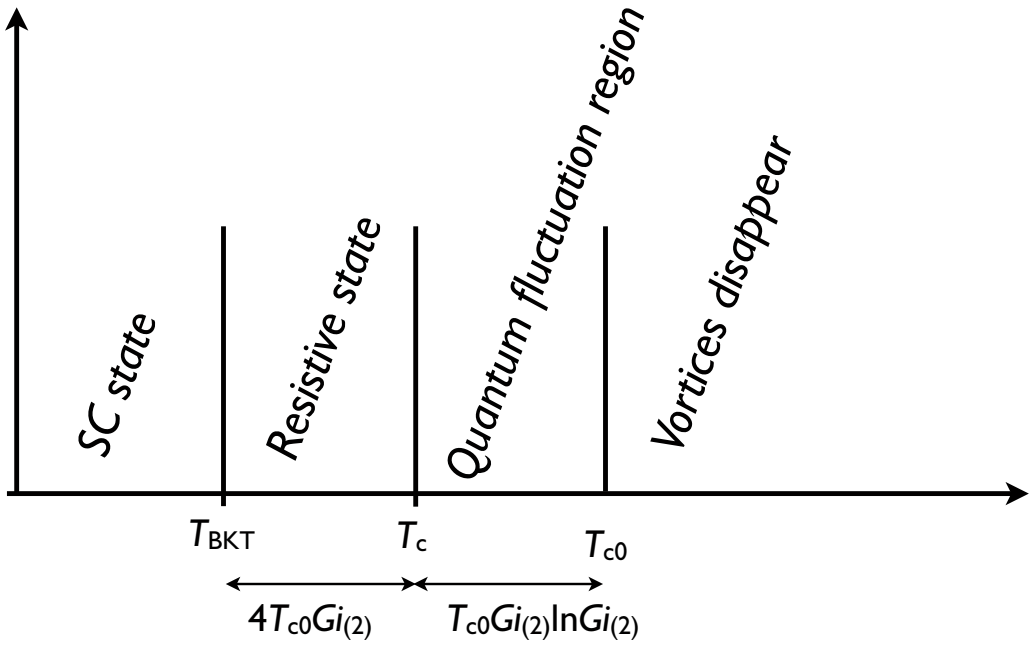

Figure 7.2: Sketch of the different temperature transition zones.

From an experimental point of view, in these cases, the determination of T_c and therefore T_{BKT} is a non-trivial task. [55] T_c can be determined by juxtaposing the measured $R_{\square}(T)$ with the results of the theory of superconducting fluctuations (SF) in the region $T > T_c$, as it enters the theory as a parameter (see ref. [54] for a review). T_{BKT} can be determined either by the analysis of the power-law behavior of current-voltage *(I-V)* characteristics at zero magnetic field or by the change of the curvature of the MR from convex to concave in the magnetic field perpendicular to the film plane [52, 56–63].

Many works have been published trying to understand quantum contributions [64–72] in different materials, but it has not been until recent that publications have been able to analyze how all quantum corrections to conductivity (QCC) contribute to the determination of T_c. These results have been used to determine the critical temperature of the samples of this thesis and to show how the SC transition temperature decreases when disorder increases.

These contributions have their inherent temperature and magnetic field behaviours that govern the transport properties of disordered systems and strongly depend on dimensionality. Samples presented on this work are quasi-

2D systems, which must follow the next conditions ($\lambda_F, l < d < \xi, l_\varphi, l_T$):

- The sample thickness, $d = 5$ nm, is larger than both the Fermi wavelength, λ_F, and the mean free path, l.
- The sample thickness d is less than the coherence length, $\xi = \sqrt{\frac{0.69\phi_0}{2\pi B_{c_2}(0)}}$, the phase coherence length, $l_\varphi = \sqrt{D\tau_\varphi}$ (where $\tau_\varphi^{-1} = \frac{\pi k_B T}{\hbar}\frac{e^2 R_\square}{2\pi^2\hbar}\ln\frac{\pi\hbar}{e^2 R_\square}$), (responsible for the weak localization effect) and the thermal coherence length ($l_T = \frac{2\pi\hbar D}{k_B T}$), responsible for the electron-electron interaction in both the Cooper contribution and the diffusion contribution.

All these parameters have been calculated and appear in Table 7.1 .

	T_c (K)	$B_{c_2}(0)$ (T)	D ($\frac{\text{cm}^2}{\text{s}}$)	$k_F l$	ξ (nm)	l_φ (nm)	l_T (nm)
fA	1.15	3.27	0.267	1.386	8.333	10.589	11.327
fB	1.09	3.27	0.253	1.314	8.333	10.700	11.027
fC	1.08	3.27	0.251	1.301	8.333	11.059	10.977

Table 7.1: Table of sample characteristics. It can be seen that all parameters follow the condition of quasi-2D systems, remembering that the sample has a thickness of 5 nm. T_c is obtained by fitting the experimental data to the quantum corrections theory.

Taking everything into account, the theory of QCC (see [54, 73] for a review) rests on two major phenomena that can be written for these samples as follows:

- The diffusive motion of a single electron is accompanied by quantum interference of electron waves (weak localization (WL)) impeding electron propagation.
- Disorder enhances the Coulomb interaction between electrons.

The corresponding QCC comprise two components as well:

- The interaction between electrons with close momenta (diffusion channel (ID)).
- The interaction of electrons with nearly opposite momenta (Cooper channel).

The contribution from WL and ID can be written as:

$$\frac{\Delta G^{WL+ID}(T)}{G_{00}} = A \ln(\frac{k_B T \tau}{\hbar}), \tag{7.1}$$

where

$$G_{00} = \frac{e^2}{2\pi^2 \hbar} = \frac{1}{\pi R_Q} = 1.2331471 \cdot 10^{-5}\, \Omega^{-1}, \tag{7.2}$$

and

$$R_Q = \frac{2\pi\hbar}{e^2} = 25812.807\, \Omega\, . \tag{7.3}$$

R_Q is known as the quantum resistance which for two-dimensional electron systems is quantized in terms of natural constants as $R_Q = \frac{2\pi\hbar}{ie^2}$, being i an integer number typically between 2 and 8 [74].

The contribution from the Cooper channel is referred to as superconducting fluctuations (SF) and is commonly divided into four distinct types:

1. Aslamazov-Larkin term (AL) describing the flickering short circuiting of conductivity by the fluctuating Cooper pairs:

$$\frac{\Delta G^{AL}(T)_{T\to T_c}}{G_{00}} = \frac{\pi^2}{8}\frac{T}{T-T_c} = \frac{\pi^2}{8}[\ln(\frac{T}{T_c})]^{-1} \tag{7.4}$$

2. Depression in the electronic density of states (DOS) due to drafting the part of the normal electrons to form Cooper pairs above T_c:

$$\frac{\Delta G^{DOS}(T)}{G_{00}} = \ln[\frac{\ln(T_c/T)}{\ln(k_B T_c \tau/\hbar)}] \tag{7.5}$$

3. The renormalization of the single-particle diffusion coefficient (DCR). [75] This is a very small contribution that has been added lately to the model and has not been taken into account in this thesis calculations.

4. The Maki-Thompson contribution (MT) [67, 68] coming from coherent scattering of electrons forming Cooper pairs on impurities:

$$\frac{\Delta G^{MT}(T)}{G_{00}} = \beta(T) \ln[\frac{\ln(k_B T \tau_\rho)}{\hbar}] = \beta(T) \ln[\frac{\ln(\pi)}{8\delta}] = B\beta(T)\, , \tag{7.6}$$

where

$$\delta = \frac{e^2 R_\square}{16\hbar} \ln[\frac{\pi\hbar}{e^2 R_\square}] = \frac{\pi\hbar}{8 k_B T \tau_\rho} , \tag{7.7}$$

and $\beta(T)$ is the electron-electron interaction strength function introduced and tabulated by Larkin. [71]

The total conductivity of the disordered system is thus the sum of all the above contributions added to the bare Drude conductivity G_0:

$$G(T) = G_0 + \Delta G^{WL+ID} + \Delta G^{SF} \tag{7.8}$$

$$\Delta G^{SF} = \Delta G^{AL} + \Delta G^{DOS} + \Delta G^{DCR} + \Delta G^{MT} \tag{7.9}$$

In this case $G(T)$ in 7.8 stands for the conductance, which is the conductivity times the film thickness d, and is the inverse of the sheet resistance, $R_\square$.

The temperature dependencies corresponding to the corrections calculated from equations from (7.1) to (7.6) together with the curve describing the sum of all the corrections are shown in Fig. 7.3 by solid lines. The experimental data for sample fB, are shown as black-filled squares. The fit of the theoretical curves to the experimental data was carried out taking the reference point at 10 K (assuming that all the contributions are practically zero at this temperature) according to the formula

$$R_\square = \frac{1}{G(T) + \frac{1}{R_\square(T=10K)}} . \tag{7.10}$$

The fitting parameters are shown in Table 7.2 .

	T_m (K)	$R_\square(T_m)$(kΩ)	T_c (K)	A	B
fA	10	4,09	1.15	2.8	1.2
fB	10	4,44	1.09	2.6	1.15
fC	10	4,80	1.08	1.98	0.7

Table 7.2: Table of the parameters for quantum corrections. T_m corresponds to the reference point of high temperature (assuming that all the contributions are practically zero at this T), $R_\square(T_m)$ i the square resistance of the reference point T_m, T_c is the critical temperature obtained with this fitting, A is the parameter related to WL+ID, equation (7.1), and B is related to MT, equation (7.6).

Some conclusions can be drawn from these fittings: for temperatures $T > 2T_c$ the total fluctuation-induced conductivity merely coincides with

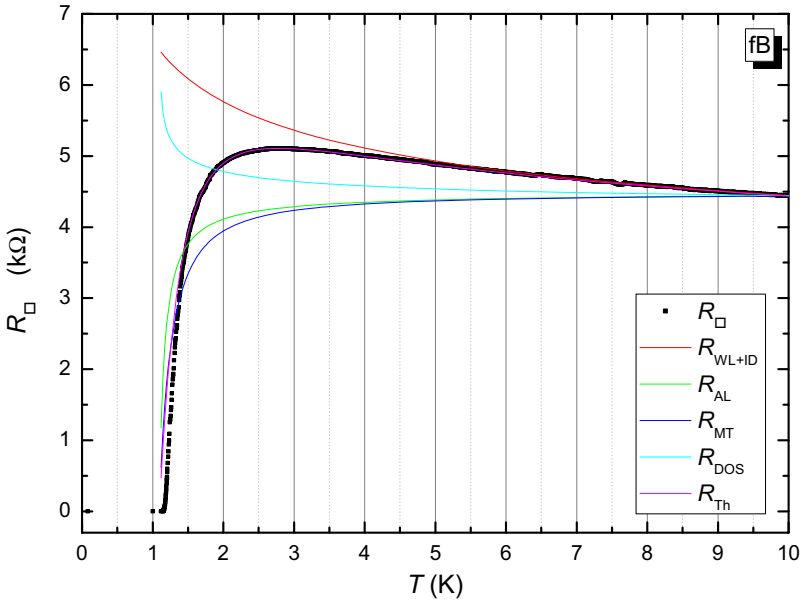

Figure 7.3: Quantum corrections for sample fB. The term R_{Th} is the one expressed in equation (7.10) which comes from adding all contributions and fits the experimental data.

great precision with that given by the MT term. Moreover, the MT process dominates the fluctuation superconductivity down to temperatures $t - 1 \lesssim \delta$, where $t = T/T_c$. At lower temperatures the AL contribution starts to become larger. The fact that MT is a leading process in a wide range of temperatures had already been emphasized in very early works [67–71]. On the experimental side, numerous experimental studies demonstrate that the MR at $T > T_c$ is caused mainly by the suppression of the MT process [76–85].

Although SF contributions alone would have resulted in the monotonic behavior of the resistance (with $dR/dT > 0$), the contributions from WL and ID processes make $R_\square(T)$ become non-monotonic and exhibit a maximum at some temperature, T_{max}, slightly above T_c [55], as it is observed in experimental results too (see Fig. 6.7). It is noteworthy that the maximum lies in the domain where the SF are dominated by the MT contribution and that the maximum itself arises from the competition between the WL + ID and MT processes.

The fitting remarkably captures all major features of the observed de-

pendences (see Fig. 7.3): the non-monotonic behavior, the position and the height of R_{max}, and the graduate decrease in the resistance matching perfectly the experimental points down to values $R \ll R_{max}$.

It is noteworthy that while varying δ and A significantly shifts the temperature position and the very value of R_{max}, it does not change noticeably the position of T_c. It reflects the fact that ΔG^{SF} does not depend on the pair-breaking parameter δ in the close vicinity of T_c.

The values of T_c obtained by this method are much more precise than the ones achieved by taking a certain percentage of the transition, for example.

In conclusion, it has been demonstrated that the temperature dependence of the resistance of quasi-2D superconducting films, including its non-monotonic behavior and the significant broadening of the transition, is perfectly described by the theory of quantum corrections to conductivity. The analysis based on a careful account of all contributions enabled a precise determination of the superconducting transition temperature. It has also been checked that the increase of disorder in this systems causes a shift of T_c to lower temperatures.

7.2.2 Magnetic field tuned SIT

Metal and insulator are two basic ground states of electrons in solids. The Cooper pairing, a manifestation of the attractive part of the electron-electron interaction, results in an instability of the Fermi sea and the formation of a new ground state. This superconducting state is characterized by long-range phase coherence and the possibility of non-dissipative charge transport. On the other hand, disorder acts in the opposite direction, as it favors the repulsive part of the electron-electron interaction and the localization of the electron wave function. The competition between localization and superconductivity can result in an insulating ground state, called Bose insulator, which is formed by localized Cooper pairs [86–88].

At zero temperature the transition between these two phases, the SIT, is driven purely by quantum fluctuations and is one of the prime examples of a quantum phase transition [89, 90]. Experimentally, the SIT can be induced by decreasing the film thickness [91, 92] and also by applying a magnetic field close to the critical thickness [93]. These possibilities are commonly distinguished as disorder-driven SIT and magnetic-field driven SIT. In the latter case, the magnetic field is supposed to suppress first the macroscopic phase coherence, while the Cooper pairing may survive locally. At sufficiently low temperatures this results in a sharp increase of the resistance up to several orders of magnitude [94] (Bose insulator). Upon further increasing the magnetic field, the localized Cooper pairs are gradually destroyed, leading

to a strongly negative MR [95].

Between these two states there is the only metallic phase point, and this metal has a bosonic nature as well (see Fig. 7.4). The theoretical description based on this assumption was suggested in [88]. At finite temperatures, a quantum phase transition is influenced by thermal fluctuations, and according to the theory:

1. The film resistance, near the magnetic-field-induced SIT at low temperature in the vicinity of the critical field is a function of one scaling variable $\delta = \frac{|H-H_c|}{T^{\frac{1}{\nu z}}}$, with the critical exponents ν and z being constants of order of unity.

2. At the transition point, the film resistance is of the order of the quantum resistance for Cooper pairs (see equation (7.3)).

Although much work has been done, and in many systems the scaling relations hold [93, 95–99], the magnetic-field-induced SIT in disordered films remains a controversial subject, especially concerning the insulating phase and the bosonic conduction at $H > H_c$. The behavior of the resistance in this region discussed in [97, 98] in terms of the magnetic-field-induced SIT can actually be explained in the framework of the theory of the quantum corrections to the conductivity in disordered metals. The possibility of such interpretation is shown in [100] based on the recent calculation of the quantum corrections to conductivity due to superconducting fluctuations [101]. As a usual thermodynamic superconductor-normal metal transition, provided that the behavior of this metal is controlled to a considerable degree by the quantum corrections, and a superconductor-insulator transition may have very similar experimental manifestations, some clear criteria are needed to enable one to tell which of the two underlies the behavior observed experimentally.

Some experimental evidence of the SIT are:

- Fan-shaped curves for the isomagnetic temperature dependences of the resistance. It has been shown that samples of this thesis follow this behavior (see Fig. 6.9 and 6.11).

- Existence of a critical resistance corresponding to a critical magnetic field, independent of the temperature (H_c, R_c) (See Fig. 6.13).

- Displacement of R_c with the disorder.

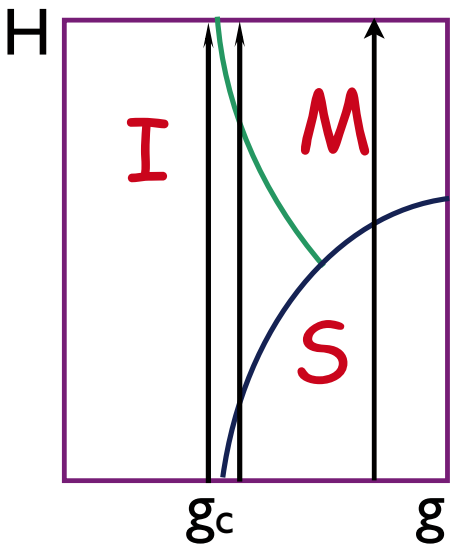

Figure 7.4: Sketch of the phase diagram with the superconductor (S), metal (M) and insulator (I) states, and the SMT, SIT, and SIMT. The abscissa axis represents conductivity and g_c the critical region where a SIT can be observed.

- The presence of a $R_{\square_{max}}$ leading to a subsequent MR that saturates to a value of the order of the quantum resistance (see equation (7.3)). The Zeeman splitting of the localized Cooper pairs seems to be the likely mechanism behind the suppression of the Bose-insulator phase (see [36] for details). Although we are not able to reach high enough magnetic field to check this result the behavior of our samples seems the same.

It can be seen in Fig. 6.13 that the results presented in this work for the as-cast thin films match the behavior just exposed.

Some of the characteristic values for the samples presented in this thesis are summarized in Table 7.3.

Analyzing the evolution of the resistance with the magnetic field for various temperatures it can be seen the existence of a critical point $(H_c, R_{\square_c})$ (see table 7.3), as it was expected. Using the value found for H_c, the same data can be plotted against the variable $\frac{|H-H_c|}{T^{\frac{1}{\nu z}}}$ and the product of the critical exponents νz can be adjusted to obtain the best scaling of the data. Following this procedure, all curves should scale for a single value of νz. [36, 40] This has not been possible for the results presented in this thesis, where the best scaling is obtained for two different values of the critical exponent for fields

	H_c (T)	R_c(kΩ)	H_{max} (T)	$R_\square(H_{max})$(kΩ)
fA	3.27	4.95	3.76	7.50
fB	3.27	5.00	3.99	7.12
fC	3.27	6.06	3.75	9.47

Table 7.3: Properties of the measurements as a function of the magnetic field for as-cast thin films obtained from the analysis of Fig. 6.13. The value for the maximum is for the lowest temperature.

above ($y = 0.55$) or below ($y = 0.23$) H_c (see Fig. 7.5).

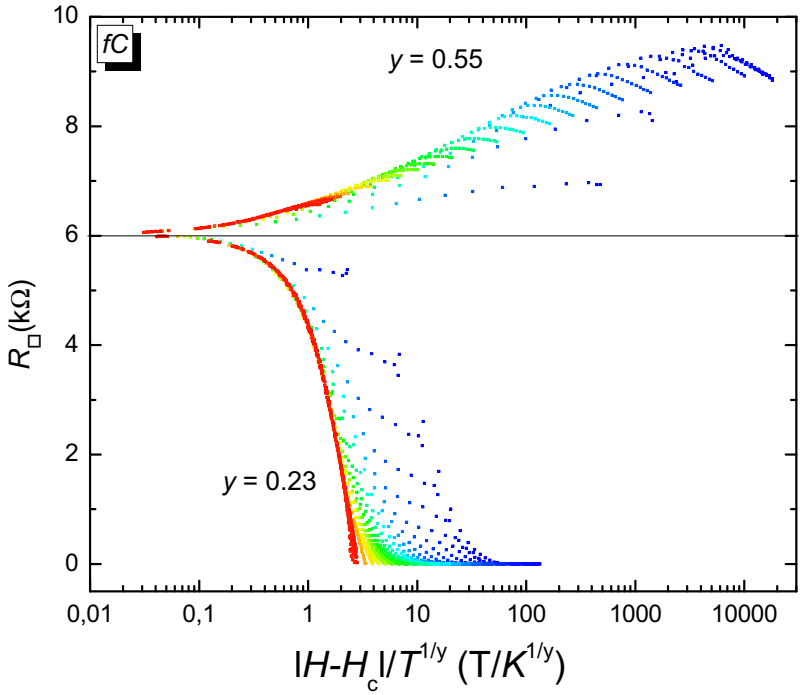

Figure 7.5: Scaling of the resistance per square measured in a temperature range from 0.1 K to 1.2 K ($H_c = 3.27, R_{\square_c} = 6.06k\Omega$).

However, it has been suggested that such behavior, previously regarded as the main evidence for the existence of SIT, is actually not an incontestable proof of the presence of the superinsulating phase at $H > H_c$ [100]. In this regime, $G(T)$ should be well described by $G(T) = a + bT^{1/3}$ (see reference [36]). In order to ascertain the type of phase, the temperature dependence

of the high-field conductance at different magnetic fields has been analyzed (see Fig. 7.6). To be able to assure this is a SIT, $G(0)$ has to be negative at least for one field over the critical field. Analyzing the fit of the data for sample fC (the most resistive of the three), this is not the case.

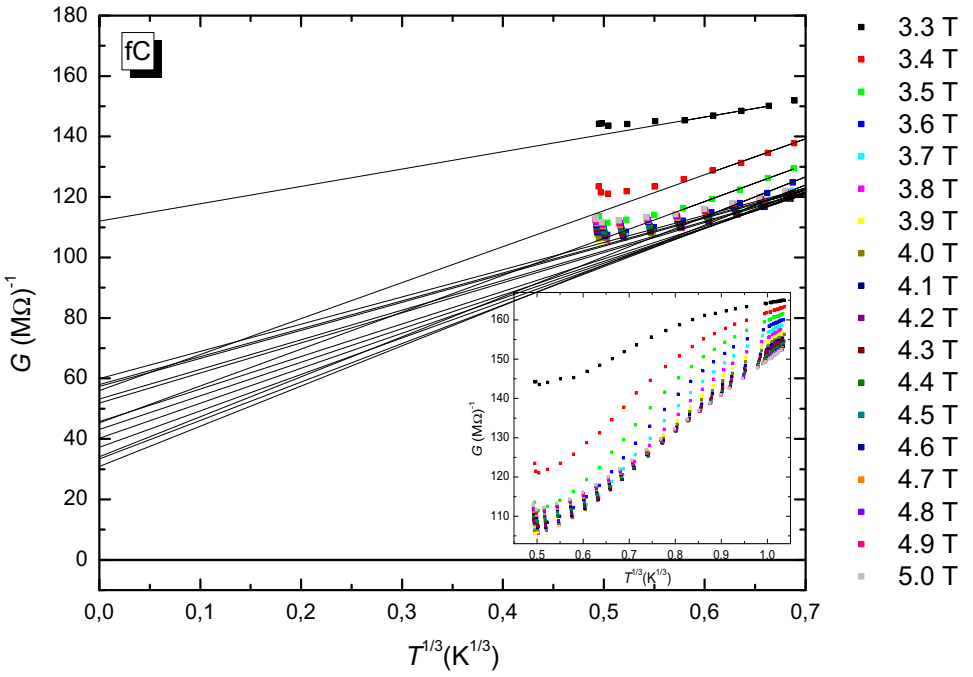

Figure 7.6: Conductance $G = 1/R_{\square}$ vs $T^{1/3}$ at different magnetic fields on the high-field side of the SIT. The inset shows all the range of temperatures measured.

Following this idea, it has been proposed [36, 40] that although the behavior of the resistance conforms, in general outline, to the expected pattern for the H-induced SIT, in some experiments [97, 98, 102] the change of the resistance at $H > H_c$ is very small, about ten percent at most. This reminds of the behavior of a disordered metal with quantum corrections to the conductivity rather than that of an insulator. Then these features can actually be explained in the framework of the QCC theory in disordered metals, provided that the correction is smaller than the conductivity itself.

Despite this suggestion, considering the results obtained for fC, the SIT can not be excluded due to the following reasons. On the one hand, the double critical exponent indicates that the behavior is not the same for both

sides of the H-induced phase transition, as it was expected. On the other hand, it can be seen in Fig. 7.6 that our curves do not fit $G(T) = a + bT^{1/3}$ in the lowest temperature range. This could be explained by an overheating of the sample by the current applied to perform the transport measurements. Because of this, the value of $R_\square$ measured in the SC state could be higher than the real one, while that measured in the SI state would be lower. This means that in terms of the conductivity we might be detecting a value larger than the real one in the SI state, so a negative value for $G(0)$ can not be excluded because of the error in the measurement due to the overheating.

Being not able to rule out or quantify the effects of a possible overheating, the SIT can not be excluded especially considering that our plain films have all the experimental evidence of a SIT, as it has been said before.

7.2.3 Current - voltage characteristics

Extensive experimental material has been published about the disorder-driven SIT and the magnetic-field-tuned SIT, but only a few works touched on the effect of an electric field on the properties of a system near the transition point [103–105]. Interest in studying nonlinear current-voltage characteristics is caused by the possibility of determining the critical indices which reflect the fundamental properties of the transition. However, these investigations have been facing problems associated with the necessity of avoiding superheating of a system by an electric current.

Currently there are two different proposals to explain the same effect:

1. In the insulating state, the current-voltage ($I - V$) characteristics exhibit an abrupt jump of I at a H-dependent voltage threshold [106] (see Fig. 7.7). Because of the fact that this sharp jump is observed only at $T < 0.15$ K, it was taken as an indication that a new correlated state of electrons is formed [43, 47, 106] and an observation of the SIT, based on the analogy from the relation between the coherence length and the characteristic energy scale ($\Omega \propto \xi^{-z}$) and a characteristic length associated with the electric field ($l_E \propto E^{-1/(z+1)}$).

2. Some believe it is an effect of an overheating of the system by the electric current. The basic premise of the approach is that the electrons are heated by the applied power and so maintain an effective temperature, T_{el}, that is significantly higher than that of the phonon bath of the embedding material, T_{ph} [107, 108]. In contrast to other known disordered insulators, R is determined, not by T_{ph}, but solely by T_{el}.

The existence of electron overheating in the immediate vicinity of the SIT has been observed previously, and was shown to cause a saturation of the measured resistance at low temperatures [109]. These authors defend that the electron overheating phenomenon persists deep within the insulating state.

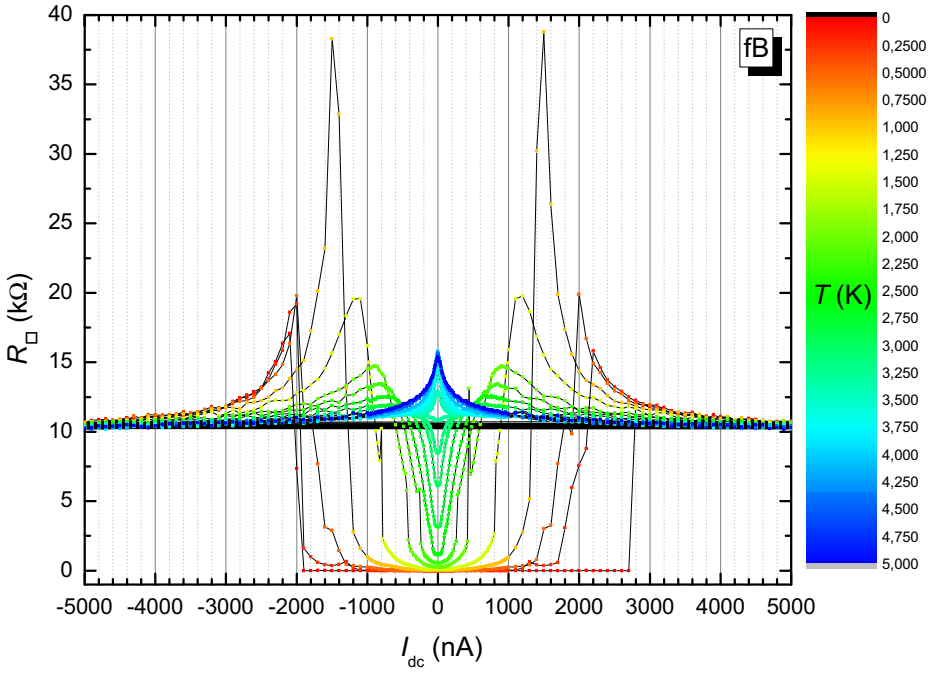

Figure 7.7: Results for $R_\square$ as a function of a dc current for different magnetic fields, presenting all the range of current in order to see the abrupt change in the I-V characteristics. Lower fields are in red, high fields are in blue. It is important to notice how for the lowest T the result is non symmetric and presents bistability due to overheating. Applying the current from negative to positive values, the first transition at negative values of I_{dc} is for a situation where $T_{el} > T_{ph}$ because of the overheating, so the transition occurs at a smaller I_{dc}. For positive values of the current, $T_{el} = T_{ph}$, the system is well thermalized and so I_c is higher.

Let us analyze these options and compare them with the data registered. Fig. 6.15 corresponds to the $R_\square$ dependences with a dc current at a temperature of 75 mK in different magnetic fields. In weak magnetic fields,

the $I - V$ characteristics have a positive derivative. In the range of strong currents, the behavior of the $I - V$ near H_c is qualitatively different: the derivative becomes negative, and the curves show a "tunnel" character. The peak amplitude increases with an increase in the magnetic field below H_{max} and decreases upon its further increase.

The curvature around $I = 0$ has been studied and the change between a valley to a peak is presented in the first and second graphs of Fig. 6.17. It can be seen how the plot of this curvature for different temperatures also coincides with the critical field of the $R(H)$ representation.

The $R(T)$ curves shown in Fig. 6.9 and the $R(I)$ curves in Fig. 6.15 are, in a sense, similar: the ranges of resistances in the same magnetic field are close, the signs of the derivatives coincide, and the curves show the same non-monotonic behavior suggesting the two experimental results may be ruled by the same process. It makes sense then to try to write a heat-balance equation applicable to the electronic system under nonlinear conditions: [87]

$$R(T_{el})I^2 = \alpha(T_{el}^{\beta} - T_{ph}^{\beta}), \tag{7.11}$$

where α (in some publications is not a parameter but the product between the electron-phonon coupling length and the volume of the sample [104]) is the coefficient of proportionality and β is a parameter to fit the experimental data which would indicate the phenomena ruling the process. The electron temperature T_{el} depends on the current and the external temperature and is determined by the balance between the Joule heat $I^2R(T_{el})$ released in the sample and the energy flux from electrons to phonons. The lattice temperature T_{ph} is assumed to coincide with the helium bath temperature T, if the sample is immersed in liquid helium.

Reference [103] proposes the transformation $T \propto I^{0.4}$. Taking into account this relation between I and T the curves presented in that paper superimposed well on one another. A value of 0.4 may well correspond to superheating with $\beta = 5$, usually observed for metals and superconductors when the deformation interaction of electrons with acoustic phonons dominates at low temperatures.

If the nonlinear behavior of the $I-V$ characteristics is due to the heating of the electron subsystem alone, the dependence of voltage U on the current I and the bath temperature T has the form:

$$U(I, T) = IR(T_{el}) \tag{7.12}$$

Differentiating equation (7.12) and introducing the expression of I obtained from equation (7.11) their experimental data seem to fit properly their hypothesis, i.e., the effect of I is the same as that of T.

At high fields up to H_c, there is a good agreement between computation and experiment. As the field decreases below H_c the α value turns virtually to zero, indicating that the heat transfer to the lattice is inefficient and equation (7.11) does not longer apply.

At lower fields (between H_{max} and H_c), the state of the electron subsystem is unclear, so that equation (7.11) cannot be theoretically substantiated with confidence. However, these authors defend the excellent agreement between the calculation and the experiment to assume that the transport and the heat transfer to phonons are dominated by normal electrons [95]. In this sense it is proposed that superheating is the main cause for the nonlinearity of the $I-V$ characteristics in the vicinity of the transition as well. Following this reasoning, the direct influence of an electric field on the SIT is then not observed. At fields below H_c, when the film resistance becomes lower than in the normal state, the role of Cooper pairs in transport cannot be ignored, and the agreement between the calculation based on equation (7.11) and the experimental curves fades away. Nevertheless, they suppose that the behavior of the electron subsystem upon applying an electric field in this region is also governed by superheating because there is no data that contradict this hypothesis.

On the other hand, some publications [104,105] present a development of bistability: using experimental data and solving numerically equation 7.11 two values of T_{el} provide a stable solution for low enough T_{ph}. Authors suggest that it is this bistability which is behind the I jumps in the data. They adopt the assumption in [105], that the measured $I-V$ nonlinearity results solely from electron overheating. At $V=0$, there is no external heating and $T_{el}=T_{ph}$. As $|V|$ is increased an increasing amount of power is supplied to the electrons and T_{el} can become larger than T_{ph}, producing a change in R that causes the apparent nonlinearity of $I-V$. The results presented constitute a convincing case for the validity of the electron overheating approach to $I-V$ data but it obscures the physical bistability that exists in the model [105].

Summarizing, some publications provide evidence that the strong nonlinearity and the I jumps in the $I-V$ characteristics of the samples in the insulating state result from a thermal decoupling of the electrons from the phonon bath. If indeed the electron transport depends on T_{el} alone, a new phonon-independent mechanism leading to the observed insulating behavior must be identified. Overheating of the electrons is quite usual in low resistive metals [110]. As for insulators (resistance far in excess of h/e^2) the overheating was rarely [111] considered quantitatively, because the conventional mechanisms of the low temperature charge transport are based on phonon-assisted hopping [112]. This explanation of the current jumps contradicts the standard picture as well as the Arrhenius law.

There are few conclusive results on this topic. In one hand a framework for the SIT is proposed based on the analogy from the relation between the coherence length and the characteristic energy scale ($\Omega \propto \xi^{-z}$) and a characteristic length associated with the electric field ($l_E \propto E^{-1/(z+1)}$). This hypothesis has not been proven yet and in the meantime a reasoning based on the overheating of the system by the electrical current has been proposed. This suggestion seems to fit the experimental data at high magnetic fields but not in the lower case. At the same time the model proposed leads to a physical bistability that has no been proved neither explained yet.

Further research should be developed on this subject because none of the two models proposed today is in full agreement with the experimental data or is able to explain what is observed.

7.3 Perforated film

Physical properties of superconducting films can be significantly changed by the artificial introduction of defects. Such defects can be holes in films.

Nanopatterning a thin TiN film into a regular square lattice of holes turns it into an array of weak links and, therefore, increases disorder and stimulates the direct SIT. It enhances the role of the 2D Coulomb interaction and changes the characteristic energies of the film on length scales significantly larger than the mean free path or the superconducting coherence length. Depending on the original degree of disorder it either suppresses the critical temperature T_c, or drives the initially superconducting film into an insulating state, or else, transforms the originally insulating film into an even more pronounced insulator. Nanopatterned films also present remarkable features in the magnetic-field dependence of the resistance, predicted by the theory of Josephson junction arrays (JJA), and repeatedly observed in experiments. [113–117]

There is still no comprehensive study of the transport properties of these samples or a theoretical framework to explain their behavior. Measurements in this thesis are in agreement with recent publications and open different possible research lines that would be interesting to continue.

7.3.1 Disorder-driven SIT

One of the most remarkable aspects of disordered superconducting film is the ability to be a superconductor and somehow turn into an insulator [91,92,118–122]. One of the engines driving this transition is the effect of disorder in the sample. On the one hand, disorder limits the electron diffusion

enhancing thus the Coulomb electron-electron interaction which competes with the Cooper pairing [123, 124]. On the other hand, disorder-induced inhomogeneities in an interplay with the enhanced Coulomb interaction localize Cooper pairs to form an insulating state, Cooper-pair insulator. For this to be possible a restricted geometry is needed as it has been presented for the initial films. For the insulating state to be observed the thickness of the superconducting material has to be comparable or smaller than the superconducting coherence length ξ. One of the major experimental challenges in these studies remains the optimization of material parameters taking the sample in study to the closest proximity of the direct SIT and identifying the systems that exhibit such a transition at available temperatures. Thats why improvement of the deposition and nanopatterning techniques during the last years has been fundamental to be able to advance on this subject.

To fabricate the nanoperforated film presented here, a 80-nm-period square lattice of 20-nm-diameter holes was patterned covering part of the Hall bridge by electron beam lithography and plasma etching on a 5-nm-thick TiN film. The square lattice and a schematic equivalent JJA is shown in Fig. 7.8.

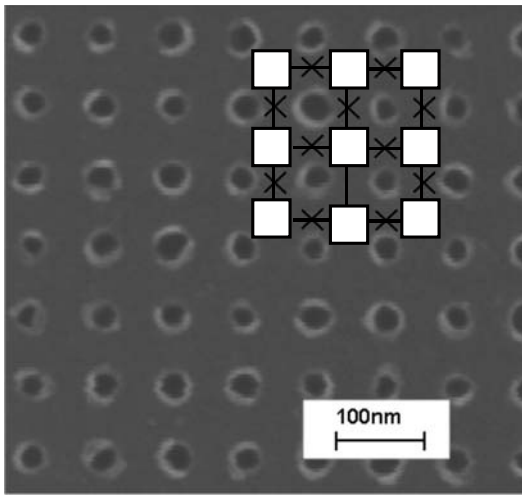

Figure 7.8: Scanning electron micrograph of the part of the TiN film patterned with the nanometer square array of holes with the centers spacing of 80 nm. The Josephson array is schematically shown on the image: weak links are crosses and superconducting islands are white squares.

Fig. 6.8 shows temperature dependences of $R_\square$ for zero magnetic field. Results for the perforated sample demonstrate the occurrence of the SIT. Sample pA and pB transit to a SC state while sample pC turns to be a SI. This means that the disorder-driven transition is observed in this case while

for initial films (fA, fB, fC) disorder was not enough and the three samples had superconducting transitions (see Fig. 6.7).

Measurements as a function of T are also presented in logarithmic scale in Fig. 7.9 (films) and 7.10 (perforated) in order to emphasize the features of the temperature behavior of the resistance and compare how changes with disorder are more remarkable in perforated samples than in plain films. Resistances of all the nanopatterned films grow upon decreasing the temperature from room temperature, with all the superconducting samples showing a non-monotonic $R_{\square}(T)$ behavior with a pronounced maximum preceding the superconducting transition. The maximal resistance of films and perforated are presented in table 7.4. Upon further cooling the pB sample exhibits a drop in the resistance to a finite value, remaining in the resistive state even at the lowest temperatures. That is, sample pB does not transit into a global phase coherent superconducting state. This issue will be taken up again once the results as a function of the magnetic field will have been discussed. While the reference sample fC falls to a superconducting state, the nano-structured part pC appears at the insulating state of the SIT. Both fA and pA have a complete superconducting transition.

	film $R_{\square}$(kΩ)	perforated $R_{\square}$(kΩ)
A	4.7	10.7
B	5.1	20.7
C	5.4	-

Table 7.4: Maximal resistance for both, perforated and plain films, for the samples with a superconducting transition.

We now turn to details of the electronic transport properties. Upon cooling down to 10 K all samples exhibit a logarithmic temperature dependence of the conductance (see Fig. 7.11), $G(T) = 1/R_{\square}(T)$, which is well described by equation (7.1). This behavior is in agreement with the QCC theory for quasi-2D disordered systems and can be attributed to weak localization and repulsive electron-electron interaction corrections [73] explained in section 7.2.1 of this thesis.

The difference between the slopes of each set at high T is of a factor around 3 in agreement with the geometric reduction of the effective cross-sections of the conducting channels in nanopatterned structures as compared to those in the reference films. This evidences that local resistivity and, accordingly, microscopic disorder are the same in both patterned and continuous films in each respective state, A, B, and C. Nevertheless, it can be noticed here that the factor obtained in our results is smaller in some cases,

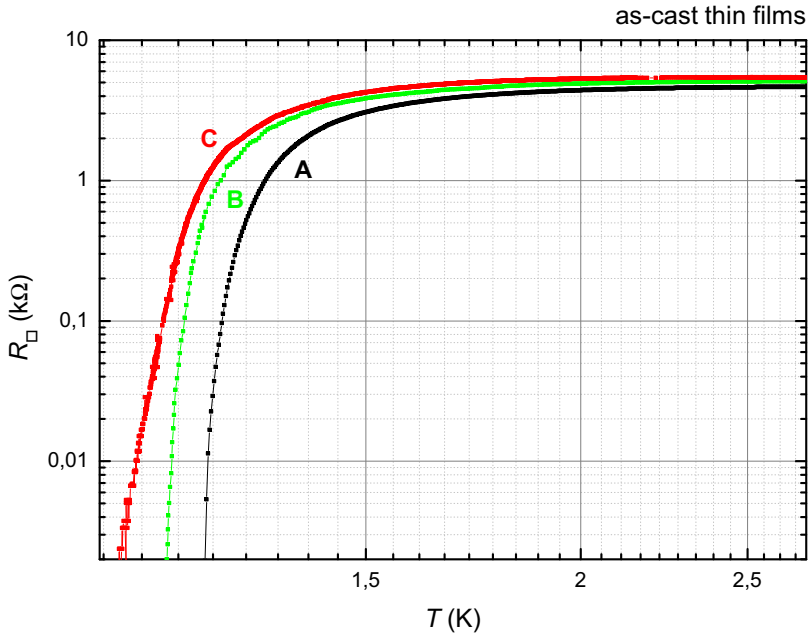

Figure 7.9: Comparison in log-scale of the results of the measurements as a function of the temperature of the as-cast thin film for the three evolution states of the sample: fA, fB and fC.

probably because the reduction in the effective cross-sections due to perforating the sample is not really 2/3. The existence of disorder in the plain films would be causing already a constraining in the conducting channels even before perforating the sample.

The behavior of the non-superconducting sample pC is well fitted by the Arrhenius formula evidencing that it is indeed an insulator.

Finally, in the perforated samples the disorder-driven transition has been measured in spite of the results obtained for the as-cast thin films. Perforation transforms the network into a new one changing the "bond" length, and so the characteristic energy of the JJA [125]. This increases even more the disorder and favors the SIT.

7.3.2 Magnetic field tuned SIT

Applying a magnetic field to nanopatterned films brings in competing energies and spatial scales and thus commensurability effects which manifest

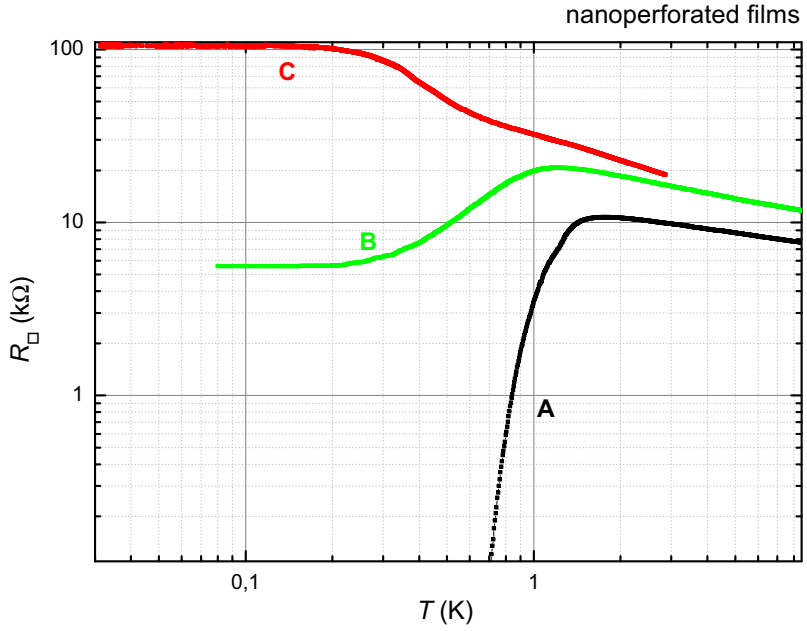

Figure 7.10: Comparison in log-scale of the results of the measurements as a function of the temperature of the perforated film for the three evolution states of the sample: pA, pB and pC.

themselves through oscillations in thermodynamic and transport properties.

At lower magnetic fields, the MR of nanoperforated films exhibits a rich structure. Commensurability effects are observed for a magnetic field (see Fig. 6.14) at which the vortex lattice spacing matches the hole lattice period [41]. There are oscillations with the period 0.32 T (see equation (7.13)), corresponding to one magnetic flux quantum, $\phi_0 = \pi\hbar/e$, per unit cell:

$$\frac{\phi_0}{d^2} = \frac{\text{Magnetic flux quantum}}{(\text{lattice period})^2} = \frac{2.067834 \cdot 10^{-15}\,\text{Wb}}{(80 \cdot 10^{-9}\,\text{m})^2} \approx 0.32\,\text{T} \qquad (7.13)$$

For sample pA minima are observed for half and double values of 0.32 T, while for samples pB and pC only the 0.32 T minimum survives because of the increase in the disorder. The oscillations are observed starting from T_c of the original films down to the lowest measured temperature achieved in the experiment, and are deeply emphasized in the more disordered samples. This contrasts with previous results [116,126,127], where the oscillations were seen

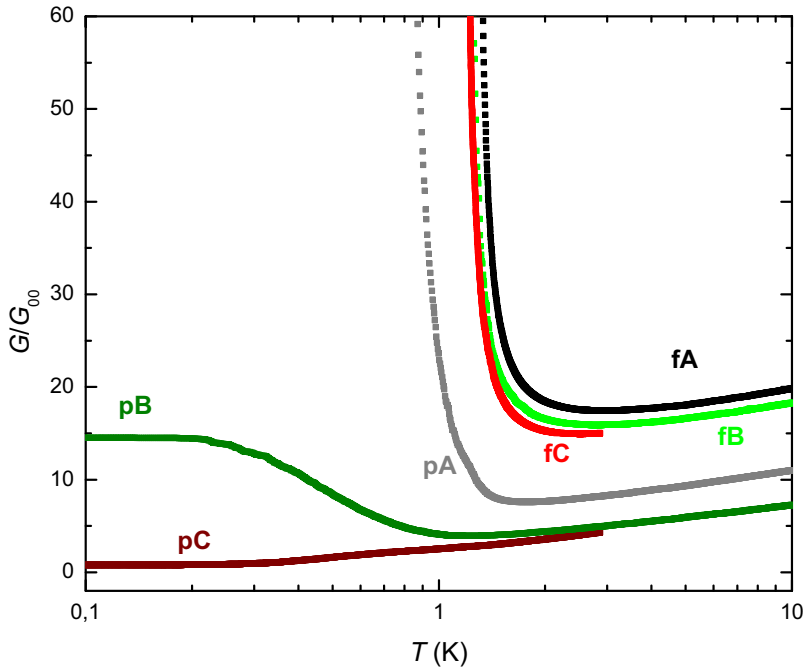

Figure 7.11: Conductance $G/G_{00} = \frac{2\pi^2\hbar}{e^2 R_\square}$ as a function of temperature for plain and perforated samples.

near T_c only.

Some important observations have to be done in sight of these results:

- The resistance oscillations are observed over a surprisingly wide temperature range (see Fig. 6.14).
- The amplitude of the oscillations experiences a colossal amplification upon approaching the SIT.
- The temperature dependence of the amplitude of the oscillations $\Delta R_\square$ does not coincide with that of $dR_\square/dT$ (see Fig. 7.12). [116, 117]
- Only at low temperature and only in a less resistive sample (pA) the magnetic field dependence of the oscillations $R_\square(H)$ (see Fig. 7.13) follows that of $\Delta E/E$ (magnetic field-induced reduction of the coupling energy) as

$$\frac{\Delta E}{E} = 4f \sin^2(\pi \frac{1-f}{4}) \tag{7.14}$$

where $f = Ha^2/\phi_0$ is the magnetic field filling factor and a is the unit cell size. [128–130]

Assuming that the shift in $\widetilde{T} \equiv k_B T/E(T)$ due to f variation is equal to that in the ground-state energy, one arrives at

$$\Delta R(T) = \frac{dR}{d\widetilde{T}} \widetilde{T}_c(f=0) \frac{\Delta E}{E} \tag{7.15}$$

which indicates that both curves should coincide, unlike our results.

The most intriguing aspect of the results as a function of H is the wide temperature region where oscillations are observed. MR oscillations in perforated films and/or superconducting wire networks (SWN) were usually found, if measured in the linear response regime, in the very proximity of T_c [127, 129, 131–135]. More extended temperature regions of the MR oscillations were reported in [116, 136–139]. It has been published [128] that juxtaposing the data obtained for various systems and inspecting the geometric characteristics of these systems it can be observed that as a rule the low-temperature boundary for the MR oscillations to appear corresponds to the temperature at which $w/\xi_d(T) \lesssim 5$, where w is the width of the superconducting constriction and $\xi_d(T) = \xi_d(0)/\sqrt{1-T/T_c}$. This reminds Likharev's result [140] that the weak link cannot accommodate an Abrikosov vortex if $w < w_c$ and transforms into a Josephson junction, where the critical width $w_c(L)$ was evaluated as being equal to $4.41\xi(T)$ for the large link ($L \gg w$, where L is the link length) near T_c. For the square link ($L = w$), $w_c \approx 5\xi$ and it can become well larger for the short weak links.

It is noteworthy that in the above qualitative consideration, being close to T_c is not a condition and implies that the concept of the critical size of the superconducting weak link below which it turns into a Josephson junction can be extended to low temperatures.

The next observation is that in order to exhibit MR oscillations, the SWN should be in a resistive state. Thus the second condition determining the range of observability of the oscillations is that the temperature should be higher than the temperature of the vortex BKT transition in the SWN, T_{VBKT}. So, if the experiment lies in the interval $T > T_{VBKT} = \pi E_J/(2k_B)$, oscillations will be observed in the whole temperature range, as it is this case [141]. For this reason the $R_\square(T)$ dependence for sample pB remains

finite at all the experimental temperatures. An increase of disorder expands this range [142].

Finally, let us briefly discuss MR at large fields beyond the range of oscillations. It can be observed a huge peak of MR at some $H = H_{max}$, followed by the appreciable negative MR, as it was also presented for the as-cast thin films (see Fig. 6.14). The value of H_{max} shifts towards larger fields upon increasing T in a similar way as for the initial films. In spite of the reference films, where the degree of disorder was not enough to take the sample to the SIT with the magnetic field, in the perforated films the change in the resistance is much larger and so the negative MR is more pronounced indicating undoubtedly that the magnetic-field-induced SIT is being observed.

7.3.3 Current - voltage characteristics

Current-voltage characteristics are the darkest side in trying to understand how these systems work, both in the initial layers, where the discussion is latent, and in the perforated films, even when there is no clear theory to describe them.

Results presented about this subject in the thesis are in agreement with what is published and what is known until nowadays. Experimental data confirm one of the possible explanations for charge transport proposed in the literature (see Fig. 6.19).

Many measurements have been performed as a function of the dc current for different temperatures and magnetic fields. An example is shown in Fig. 6.16 where the differential resistance per square as a function of dc current is drawn for samples pA and pB. The SIT is shown as a change of the behavior from a minimum to a maximum at zero dc current as the magnetic field increases. The curvature of $R_{\square}(I_{dc})$ at $I_{dc} = 0$ (black) and the differential resistance per square (red) are plotted vs magnetic field in Fig. 6.17. The curvature shows several sign changes for sample pB (bottom panel) confirming commensurability effects. Results for sample pC, which has already an insulating behavior, are shown in Fig. 6.19.

Let us try to explain what may be happening with the theoretical knowledge we have today. Superconductor/normal-metal (SN) interfaces of high transparency exhibit remarkably different properties for electric charge and energy transfer. Quasiparticles with energy ϵ below the superconducting energy gap Δ cannot enter the superconductor. This implies a high thermal resistance at the SN boundary since energy is exclusively carried by the quasiparticles. [143] In contrast, charge can be transmitted at $\epsilon < \Delta$ via the Andreev reflection process: an electron coming from the normal side is re-

flected as a hole and a Cooper pair is transferred to the superconductor. [144] This has important consequences for the energy distribution of quasiparticles in a short normal bridge connected to two superconducting reservoirs. Assuming that the length L of the bridge is larger than the thermal diffusion length $L_T = \sqrt{\frac{\hbar D}{2\pi k_B T}}$, which governs the penetration of Cooper pairs into the normal wire, the supercurrent through the structure is then exponentially weak.

It was found [145] that in granular arrays the tunneling electrons generate strings of electron-hole pairs which serve as an environment enabling tunneling. In two dimensions the Coulomb interactions between charges are logarithmic and the electron-hole plasma experiences the charge BKT transition [146, 147] at temperature $T = T^* \simeq E_c$, where E_c is the charging energy of a single superconducting island. Accordingly, the energy gap of the order of E_c appears in the environment excitations spectrum. Opening this gap completely [138] impedes both Cooper pairs and normal quasiparticle currents in the superconducting tunneling array at $T < E_c$. This is the microscopic mechanism of the insulator-to-superinsulator transition [43, 47].

Although the above results were derived in a context of granular arrays, the same picture holds for homogeneously disordered 2D superconducting films as well [46, 148, 149], as it is the case presented here. Indeed near the disorder-driven superconductor-insulator transition (D-SIT) the films exhibit an electronic phase separation [150] and can be well modeled as a two-dimensional array of superconducting weakly coupled islands. Such systems develop a huge dielectric constant on approach to the transition [151, 152]; thus all the electric field lines get trapped within the film and the electron-hole environment becomes a two-dimensional plasma with the long range logarithmic Coulomb interactions. It seems then that these interaction and the resulting gap in the electron-hole environment spectrum is the major component in the formation of the low-temperature transport behavior near the transition to an insulating state in 2D systems.

Summarizing and focusing on the experimental consequence of what it has been exposed, electronic transport in alternating superconductor-normal metal junctions is mediated by the Andreev conversion of the supercurrent into the current of quasiparticles and vice versa at interfaces between the superconducting and normal regions [143]. The phenomenon ruling this mechanism is an enhancement of the conductivity observed in SNS junctions at voltages that constitute an integer fraction of the superconducting gap, $V = 2\Delta/en$ [153–161], due to the effect of the multiple Andreev reflection (MAR) [162–164]: if a quasiparticle confined between the superconducting leads and reflecting n times from the interfaces acquires from the bias the

energy equal to 2Δ, the conductivity exhibits peaks due to the enhanced normal excitations density of states at the edges of the superconducting gap. Multiply connected SNS systems, i.e. large regular two-dimensional arrays of SNS junctions comprised of nanometer-scale superconducting and normal-metal regions, add more richness to Andreev transport. In particular, these systems bring effects of synchronization [116, 165–168] which has been detected in sample pC and presented in Fig. 6.19 where dips can be observed at some voltages.

Note that since the studied films are within the critical region of the D-SIT [36, 169], even the slightest treatment can suppress their superconductivity. This is why these films offer an ideal laboratory for fabrication of multiply connected SNS systems and probing the nature of Cooper-pair transmission on a nanometer-scale.

The important result here is that the temperature dependences of the shift with voltage of these singularities follow the BCS temperature behavior of the superconducting gap (see Fig. 7.14 and 7.15). The same measurements and analysis have been performed for different magnetic fields. Peaks are also detected in this case and follow the same behavior. This is shown in Fig. 7.16 were data have been shifted vertically in order to be able to distinguish the shift of the peaks easily. More measurements would be needed in order to perform the same analysis that has been done before as a function of the temperature.

Results for different temperatures can be presented in a color map where the displacement of the peaks can be easily seen. This map is shown in Fig. 7.15, where colors represent the variation in the resistance indicating when there is an oscillation.

Fig. 7.14 shows that this is satisfied with high accuracy for the first, second and third dips, while the forth dip deviates at higher temperatures. This can be explained because of the proximity to the peak of $I_{dc} = 0$ where $R_{\square}$ grows rapidly and makes more difficult the analysis of the dependence of the position of the dips with the temperature. It is proposed in [138] that the voltage for zero T in Fig. 7.14 compares with the value of the gap found by direct scanning tunneling spectroscopy.

As a matter of fact, the enhancement of the conductivity was predicted for a single SNS unit [162–164] for voltages $V = 2\Delta/en$. In contrast, the resonant enhancement of conductivity is observed at voltages $V = 2\Delta/2^m e$, where m is the the number of resonance, i.e., the number of peak (the first peak corresponds to m=0, the second peak to m=1, and so on). These papers propose that this long-distance resonant transparency results from the multiplicative effect of the enhanced proximity in the narrow window near the middle of the superconducting gap and the enhanced density of the nor-

mal states near the edges of the gap [138]. This reveals a new mechanism of current transfer in large SNS arrays, which can be viewed as a synchronized Andreev transmission (SAT) where Andreev conversions occur simultaneously at many SN-interfaces.

The accuracy of the results presented here does not allow to verify this proposition and more tests should be performed. However, if this is confirmed it would be a novel high precision Andreev spectroscopy technique for determining the superconducting gap in disordered films. At least, what these results are able to confirm is that they follow what is expected for the superconducting gap in terms of the BCS theory verifying a superconducting behavior in an initial insulating sample.

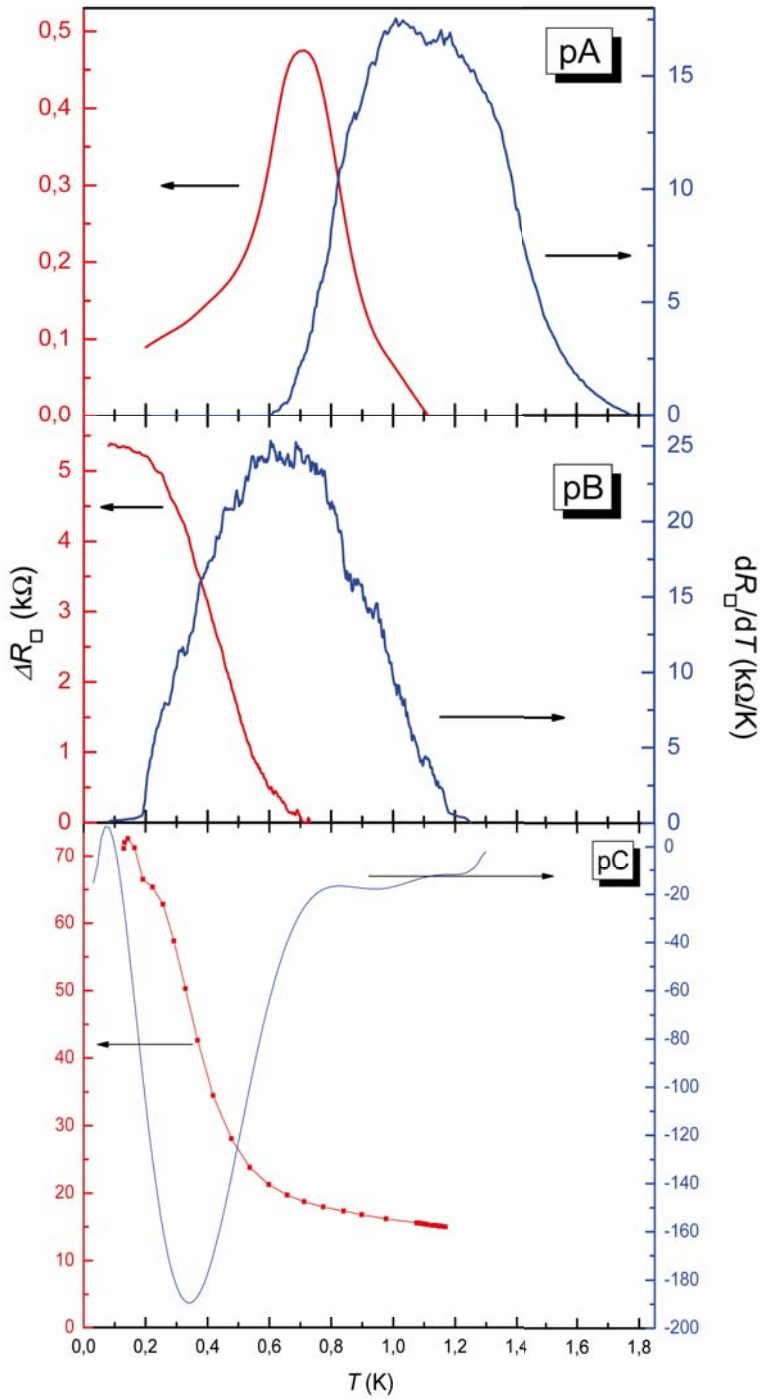

Figure 7.12: Comparison between the thermal dependence of the matching depth, $\Delta R_\square$, and that of the derivative of $R_\square$ with temperature for samples pA, pB and pC (from top to bottom).

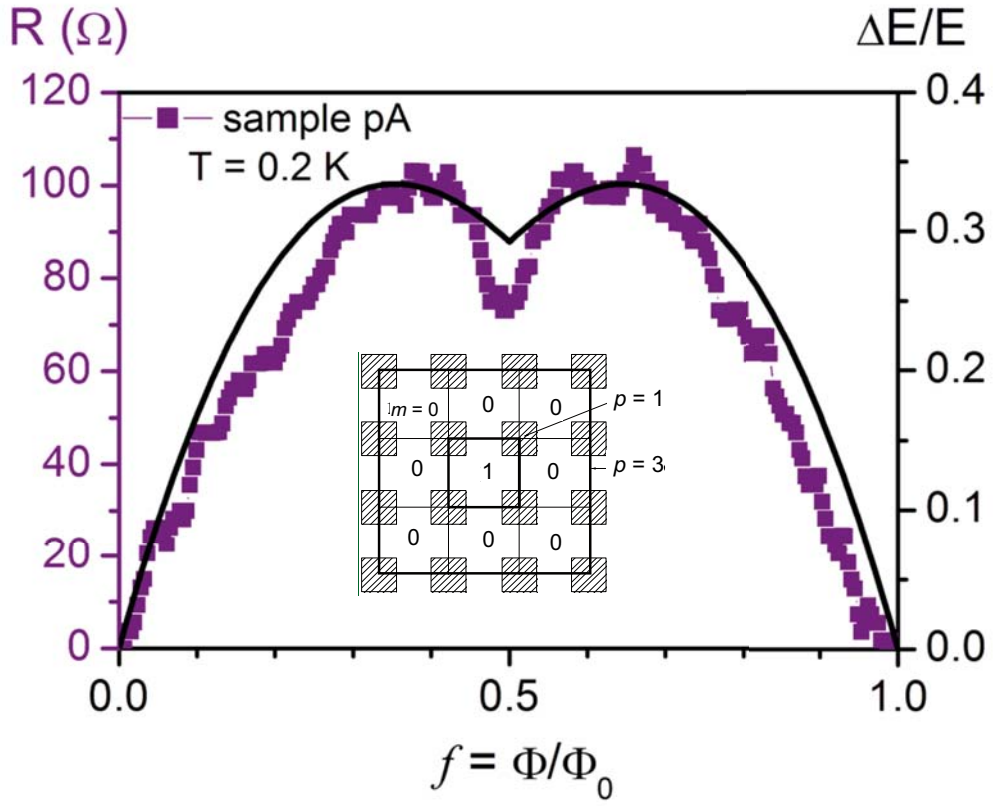

Figure 7.13: Analysis of the oscillation shape: squares correspond to the experimental results of sample pA, while the solid line represents the calculation according to the simple JJA model [117]. Inset: Sketch of the JJA.

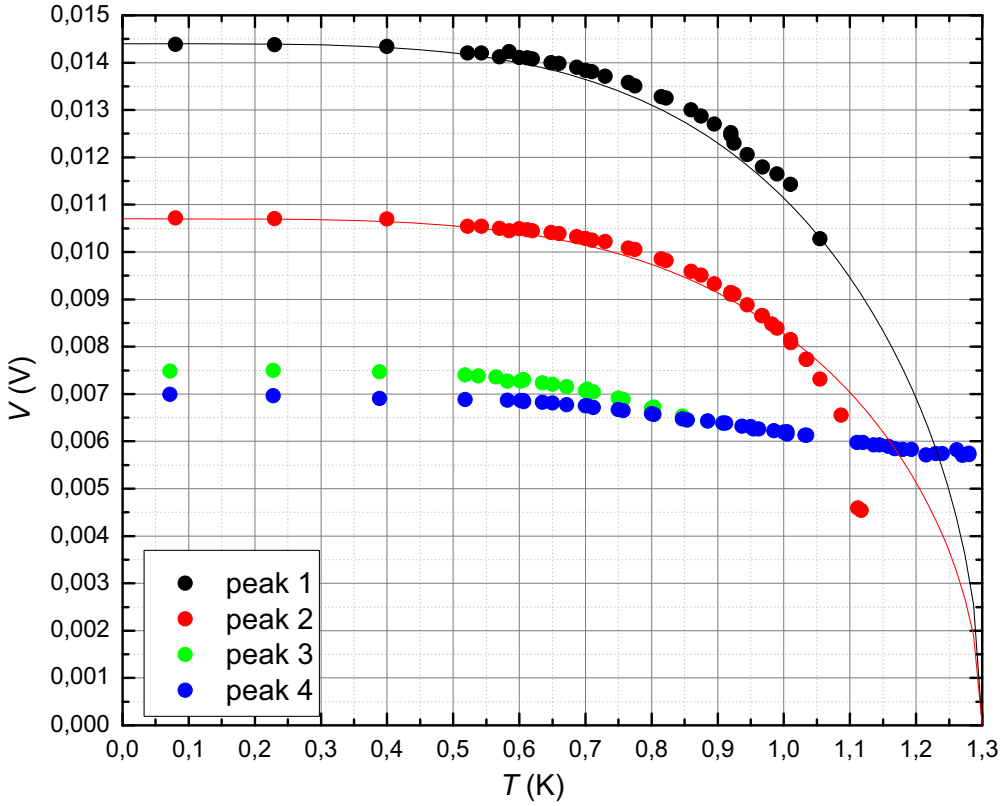

Figure 7.14: Analysis of the position of the peaks in Fig. 6.19 as a function of the dc current for different temperatures. Solid lines correspond to a fit using the theoretical expression for the SC gap in 2D samples, $\Delta(T) \propto \sqrt{\cos\frac{\pi}{2}(\frac{T}{T_c})^2}$.

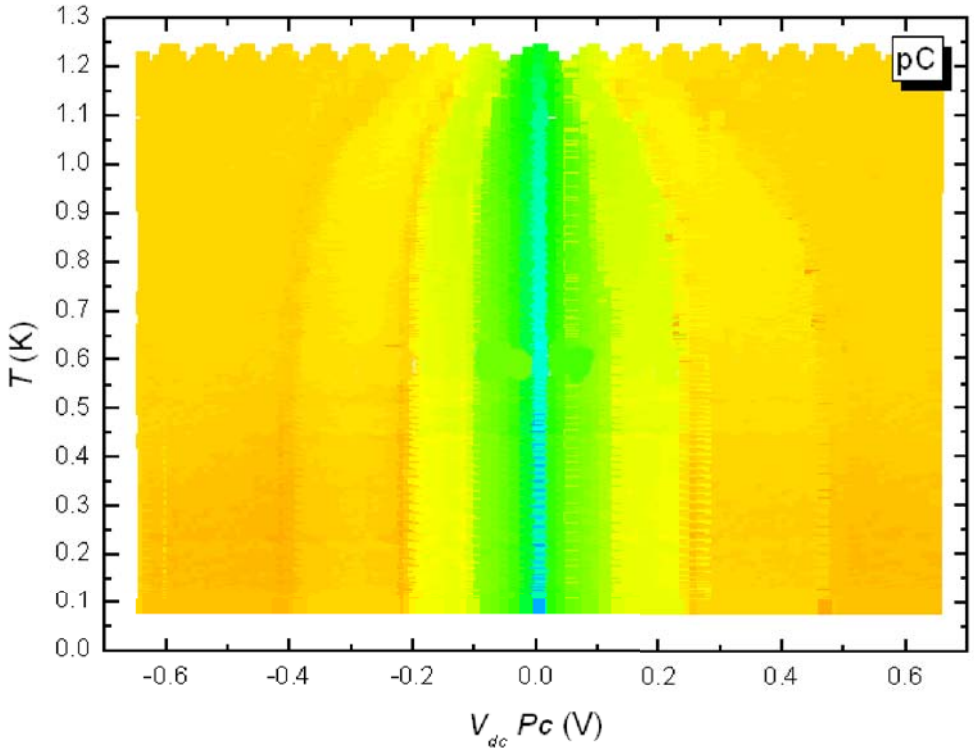

Figure 7.15: Analysis of the peaks as a function of the dc current for different temperatures in a color map. Different colors represent the changes in $R_{\square}$.

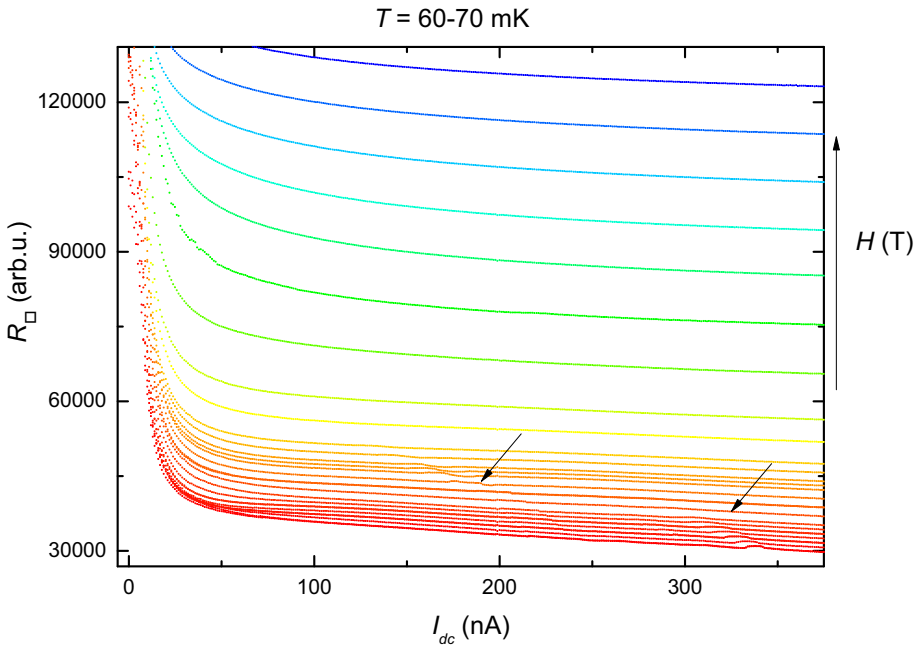

Figure 7.16: Peaks observed as a function of the dc current for different magnetic fields. Data have been shifted vertically with H in order to see the peaks easily.

Chapter 8

Conclusion

The aim of the second part of this thesis was to prove the existence and observation of the superconductor-insulator transition (SIT) and a new state of matter called superinsulator, which is considered as dual to a superconductor.

For this purpose low-temperature transport properties of nanoperforated superconducting TiN films have been experimentally studied. For a 5-nm-thick sample with a square lattice of antidots with a period of 80 nm, resistance measurements have been performed in the critical region of the SIT, applying the magnetic field perpendicular to the plane of the films or the dc current through the sample.

Characteristic parameters as T_c, D, ξ, etc., have been determined for as-cast thin films using the theory if quantum corrections to conductivity. As it is expected for these samples, critical parameters ($H_c, R_\square$ and I_c) are detected. The three thermal evolutions of the sample for the plain films have a transition to a superconducting state.

Several controversial results have been obtained studying the H-induced SIT for the plain films. Although the behavior of the resistance conforms, in general outline, the pattern expected, some extra analysis should be performed to be able to assume the occurrence of the SIT. Thus, even if the results for sample fC do not fit the conditions imposed, SIT can not be excluded. An explanation based on sample overheating is proposed. So, being not able to rule out or quantify the effects of a possible overheating, the SIT can not be excluded especially considering that our plain films have all the experimental evidence of this phenomenon, as it has been said before.

Different explanations have been exposed for the current-voltage characteristics but further tests should be developed to contribute new ideas and get a final framework that could explain this charge transport.

A deep study has been performed for the perforated films, for which the disorder-driven transition has been detected in spite of the results found

for the as-cast thin films, indicating that patterning the sample increases even more the disorder and favors the SIT. A remanent resistance at low temperatures is also observed although the sample is in the superconducting state, demonstrating the existence of normal state islands.

Commensurability effects are observed at the magnetic field where the vortex lattice spacing matches the hole lattice period. The oscillations are observed starting from T_c of the original films down to the lowest measured temperature achieved in the experiment, and are emphasized in the more disordered samples. This contrasts with the previous results where the oscillations were seen near T_c only.

From the analogy that a nanopatterned sample can be studied as a JJA it has been checked that electronic transport in alternating superconductor-normal metal junctions is mediated by the Andreev conversion of the supercurrent into the current of quasiparticles and vice versa at the interfaces between superconducting and normal regions.

In this sense it has been demonstrated a superconducting behavior in an insulating sample, that is the existence of the superinsulator state.

There is not a complete theoretical framework for this kind of samples so this is only the beginning of what should be a long researching subject.

Resum de la tesi en llengua catalana

El treball que es presenta en aquesta tesi consta de dues parts ben diferenciades. La primera pretén el desenvolupament d'un equip experimental concebut per a l'estudi de propietats magnètiques i elèctriques en materials diversos i, en especial, el treball amb radiació de microones en condicions de reflexió i transmissió. La segona s'ha centrat en les mesures de transport d'una capa fina superconductora de nitrur de titani (TiN) de 5 nm de gruix en un criòstat de dilució.

Desenvolupament d'un nou equip experimental

Aquest equip consisteix en un criòstat amb forma cilíndrica que es troba foradat al llarg de tot l'eix per facilitar mesures de transmissió amb microones. Aquest forat té un diàmetre de 36 mm, molt superior al dels criòstats convencionals, en què el diàmetre sol ser més petit de 10 mm. Això permet estudiar mostres grans i, alhora, introduir cavitats ressonants de grans dimensions per a l'estudi de les propietats esmentades, la qual cosa permet assolir les freqüències més baixes del rang de les microones, impensables per a criòstats convencionals i amb cavitats més reduïdes. El criòstat té instal·lat un imant superconductor per a l'aplicació de camps magnètics controlats de fins a 5 T, i un sistema de control de temperatura, que permet treballar en un rang entre 1,8 i 300 K. El refredament es fa mitjançant líquids criogènics: nitrogen líquid en primer lloc, i posteriorment heli-4 fins assolir la temperatura desitjada. L'escalfament es fa mitjançant una resistència calefactora que permet controlar la temperatura amb la precisió que calgui segons l'experiment que s'estigui realitzant.

S'ha dissenyat l'instrumental necessari per a l'estudi en aquest equip de les propietats esmentades anteriorment. A dia d'avui hi ha cinc sondes de mesura dissenyades i muntades. (A partir d'ara em referiré a les sondes de mesura com a canyes). Adaptant-se a les necessitats i paràmetres d'aquest

equip, la intenció ha estat construir les canyes de manera que fossin el més versàtils possible. Seguint aquesta idea, s'han dissenyat les canyes dividint-les en dues meitats, de manera que es puguin combinar segons el que més interessi per a cada experiment. Cada canya consta d'un tub d'acer de 8 o 10 mm de diàmetre, que serveix per protegir el propi sistema de mesura i per donar rigidesa al conjunt. Al llarg del tub s'hi solden unes anelles que serveixen com a mirall de radiació i per centrar el tub dins el criòstat. A la part de dalt de la canya superior s'hi col·loca la tapa per segellar el buit i un connector Fischer de setze pins. A la part inferior s'hi munta la peça que subjecta el portamostres i que alhora connecta amb la meitat inferior de la canya.

Respecte a la canya inferior, s'han fet dos dissenys diferents. Un d'ells és simplement una camisa, amb el tub d'acer, que també consta de les anelles de radiació i de la peça que uneix amb el portamostres. A més a més, a la part inferior hi té una peça d'acer que serveix per segellar el buit amb la part de baix del criòstat. A l'altre disseny s'hi afegeix un altre connector Fischer de 16 pins a la part inferior, unit a la peça que segella el buit, de manera que pugui servir per a experiments en què es necessitin fer més mesures de resistències.

A aquestes camises d'acer s'hi afegeixen els coaxials i les guies d'ones, de manera que en total hi ha nou mitges canyes, quatre parts superiors que es poden combinar amb cinc parts inferiors.

Pel que fa a les freqüències de treball, es disposa de tres rangs de guies d'ona (WR10, WR15 i WR22) que permeten treballar entre 0 i 120 GHz, i un cable coaxial que conserva el mode fonamental fins a una freqüència de 60 GHz.

S'han dissenyat diferents portamostres segons la necessitat de l'experiment. Aquests van directament connectats al coaxial o a les guies d'ona, i tot el conjunt està contingut dins de dues peces semicilíndriques que s'uneixen a les dues mitges canyes i donen rigidesa a tot el conjunt.

Un cop les canyes han estat muntades, s'han testat per comprovar que permetien fer buit correctament i refredar fins a baixa temperatura. A més, a totes s'hi ha afegit el cablejat necessari per poder treballar amb els connectors Fischer abans esmentats, així com també un sistema de petits connectors per fer més fàcil el canvi entre dues mostres que es vulguin estudiar consecutivament.

També es disposa de dos termòmetres calibrats amb un magnetòmetre SQUID per treballar especialment en l'equip presentat en aquesta tesi, i d'una caixa de connexions especialment muntada per a aquest sistema i que permet treballar alhora amb els dos connectors Fischer (el superior i l'inferior), en el cas que el nostre experiment requereixi utilitzar la part inferior de la canya

de resistències.

Una vegada tot el material ha estat preparat, s'han realitzat tres experiments diferents per tal de provar que tot funcioni correctament. El primer i el segon han consistit a estudiar la resposta magnètica d'un monocristall de Mn_{12}-acetat quan se li envia radiació de microones, ja sigui en forma de polsos o de manera contínua, mesurant primer amb un transductor i després amb una sonda Hall. Així s'ha aconseguit provocar i enregistrar allaus magnètiques al llarg de la mostra. Per a aquest experiment es van utilitzar les dues meitats de la canya que incorpora cable coaxial i, en algunes ocasions, també la meitat de la canya de resistències, la qual cosa ha permès constatar que les canyes treballen correctament.

El tercer experiment ha consistit en l'estudi del senyal de transmissió d'una mostra de TiN en enviar-hi radiació de microones. La mostra es col·loca entre dos connectors de panell i es protegeix amb un filament d'indi. Els connectors s'ajusten als coaxials i el conjunt se situa dins les peces d'acer que uneixen les dues meitats de la canya i que protegeixen el sistema. En aquest experiment s'ha aconseguit veure la transició superconductora per efecte de la radiació.

Acabats tots els experiments, l'equip està funcionant de manera sistematitzada i automatitzada amb alguns programes informàtics que s'han dissenyat expressament. Totes les canyes han estat provades i l'equip pot funcionar a ple rendiment quan es consideri necessari.

Mesures de transport en capes fines de TiN

Aquestes mesures han estat realitzades en un criòstat de dilució. La mostra conté, en realitat, dues mostres alhora, ja que una meitat és una capa fina llisa i l'altra meitat té una xarxa de forats de 20 nm de diàmetre i un període de 80 nm. La capa és un conglomerat de cristalls amb una mida mitjana de 5 nm i es va créixer mitjançant la tècnica de la deposició química. Sobre la mostra s'hi ha col·locat un pont de sondes Hall amb litografia UV, i en la part perforada, els forats s'han dut a terme amb litografia electrònica. Aquestes mostres van ser fabricades a l'Institut de Física de Semiconductors de Novosibirsk (Rússia).

La raó per la qual és necessari treballar amb una capa tan fina és que hem d'estar segurs que es tracta d'un sistema quasi 2D, i perquè sigui així s'ha de complir que el gruix de la mostra sigui més petit que la longitud de coherència superconductora, però més gran que el recorregut lliure mig dels electrons. D'aquesta manera s'està constrenyent el moviment dels parells de Cooper, i això permet observar, en aquest tipus de mostra, la transició

superconductor-aïllant (TSA). Es podria dir també que reduint el gruix de la mostra, se n'augmenta el desordre, el qual es mesura com la resistència quadràtica ($R_\square$) de la mostra. Per definir $R_\square$ es considera que el gruix és infinitesimal, i es divideix la mostra en quadrats, de manera que $R_\square$ és la resistència de cadascun d'aquests quadrats.

Les primeres mesures han estat en funció de la temperatura en absència de camp magnètic, per veure la transició superconductora i com aquesta és diferent entre les mostres A, B o C. Puntualitzem: és sempre la mateixa mostra, però es tracta de diferents parts o estadis evolutius de la mateixa. Així, fA, fB i fC són estadis evolutius de la part llisa, el film, mentre pA, pB i pC són estadis evolutius de la part perforada. Entre A i B i entre B i C, la mostra ha patit sengles evolucions. Això vol dir que ha estat sotmesa a un cicle tèrmic que consisteix a escalfar-la, en atmosfera oberta i per simple contacte tèrmic, fins a uns 350°C durant un parell de minuts. El que això provoca és un augment de $R_\square$ a temperatura ambient, és a dir, un increment del desordre, de manera que la mostra és cada cop una mica més aïllant i, per tant, això canvia els resultats en les mesures de transport.

L'estadi evolutiu A de la mostra s'ha mesurat a l'Institut de Física de Semiconductors de Novosibirsk (Rússia) sota la supervisió de la Dra. Tatyana Baturina, amb qui mantenim una col·laboració, igual que amb el Dr. Valerii Vinokour, de la Divisió de Ciències Materials del Laboratori Nacional d'Argonne (Chicago, EUA). Els estadis evolutius B i C s'han mesurat al Grup de Magnetisme de la Universitat de Barcelona. El canvi entre fA, fB i fC és relativament petit. Com era d'esperar, $R_\square$ augmenta lleugerament i la temperatura crítica es desplaça una mica a temperatures més baixes. Mitjançant les correccions quàntiques per les que es regeix aquest tipus de mostres, es poden ajustar aquests resultats amb la teoria i obtenir amb molta exactitud que els valors de la temperatura crítica per a fA, fB i fC són, respectivament, 1,15 K,1,09 K i 1,08 K, demostrant com el desordre desplaça la temperatura de transició a valors més baixos.

Per altra banda, el canvi entre pA, pB i pC és molt més notori, i comencen a aparèixer resultats inicialment inesperats. L'augment de la resistència i el desplaçament de T_c són més grans de l'esperat, i s'observa també que a baixes temperatures, la mostra pB té una resistència romanent de gairebé 6 kΩ, tot i que ja es troba en estat superconductor. Això es podria analitzar dient que dins la mostra poden coexistir illes en estat superconductor i illes en estat normal, donant com a resultat aquesta resistència, tot i que el comportament macroscòpic és superconductor. A més la mostra pC ja no té una transició superconductora sinó que resulta aïllant. Observant el mateix tipus de mesures per a diferents camps magnètics, es veu com el camp indueix la TSA, sobretot en el cas de la mostra perforada.

El segon grup de mesures realitzat ha estat l'estudi de l'evolució de $R_\square$ amb el camp magnètic per a diferents temperatures. En el cas del film les dades per a totes les temperatures s'intersequen en un mateix punt. En el marc de la teoria d'aquestes mostres, aquest punt defineix un camp magnètic crític i una resistència crítica. A diferència d'altres superconductors el camp crític és independent de la temperatura. Una altra característica d'aquestes mostres, que es pot observar en el film i més exageradament en la part perforada, és que tenen el que s'anomena magnetoresistència negativa, és a dir, que a mesura que s'augmenta el camp magnètic, totes les corbes de resistència disminueixen cap a un valor comú. Aquests són signes que es relacionen amb la TSA. Analitzant els resultats de les mostres perforades, s'observa el que es coneix com un fenomen de commensurabilitat entre el paràmetre de la xarxa de vòrtexs i el període de la xarxa de forats, donant com a resultat pics cada 0,32 T.

A la mostra mesurada a Novosibirsk, pA, s'observen pics a la meitat i al doble de 0,32 T, però en canvi aquests desapareixen en les mostres pB i pC, només quedant el de 0,32 T, degut a l'augment del desordre. Si s'analitza la dependència tèrmica de la profunditat de les oscil·lacions degudes al fenomen de commensurabilitat, $\Delta R_\square$, es veu que aquesta no segueix el comportament esperat segons els resultats publicats per M. Tiknham l'any 1983 i reproduïts per T. Baturina en el 2003, d'acord amb els quals $\Delta R_\square$ ha de coincidir amb $\mathrm{d}R_\square/\mathrm{d}T$. Per una banda, $\Delta R_\square$ no només està desplaçat respecte a $\mathrm{d}R_\square/\mathrm{d}T$ sinó que tampoc torna a zero a baixes temperatures. S'observen oscil·lacions per a un rang sorprenentment ample de temperatures i alhora, la seva profunditat augmenta en créixer el desordre entre la mostra pA i pB i entre pB i pC, fins a un ordre de magnitud.

En l'últim bloc de mesures, s'aplica un corrent dc al llarg de la mostra i es mesura en funció d'aquesta intensitat, per a diferents temperatures i camps magnètics. S'han reunit i analitzat un gran quantitat de dades modificant aquestes variables. En aquest tipus de mesura, s'observa la TSA com el canvi de passar d'un mínim (en estat superconductor) a un màxim (en estat aïllant) per a intensitat igual a zero. La intensitat crítica per al film és d'uns 2000 nA. Per veure de manera clara com es produeix aquesta transició, es pot estudiar la curvatura del pou o el pic al voltant de $I_{dc} = 0$ com la segona derivada de la resistència respecte la intensitat al voltant d'aquest valor d'intensitat. En el cas del film la curvatura presenta un sol canvi de signe que coincideix amb el camp crític, i en el cas de la perforada es presenten diversos canvis de signe que coincideixen amb el fenomen de commensurabilitat que observem. En aquest darrer estudi, per a la mostra pC s'observen uns resultats interessants. En obtenir aquestes dades es van detectar unes petites oscil·lacions per a uns valors concrets del voltatge d'excitació. Després d'un llarg procés

experimental per a reduir possible soroll o efectes geomètrics que poguessin estar afectant les mesures es va poder fer l'estudi d'aquestes oscil·lacions per a diverses temperatures.

De l'anàlisi dels resultats s'ha pogut veure com aquests pics es desplacen en funció de la intensitat i per a diferents temperatures seguint la teoria BCS, ajustant-se força bé al comportament que tindrien en tractar-se d'un efecte superconductor. Els pics més propers al centre es desvien del comportament esperat segurament degut al fet que cada cop estem en un estat de resistència més alta i en fa més difícil l'anàlisi. El mateix tipus de mesures s'ha realitzat variant el camp magnètic, i també s'observen pics amb el comportament esmentat.

Una possible explicació sobre l'origen d'aquests pics és el que es coneix com a reflexió Andreev. Es tracta d'una dispersió de partícules que té lloc a la interfície entre un superconductor i un material en estat normal. És un procés de transferència de càrrega on un corrent normal es transforma en un supercorrent, salvant la transmissió prohibida d'una partícula individual en la banda prohibida superconductora per una transferència doble a través de la interfície. En cas de reafirmar-se aquesta idea, els resultats dels experiments tindrien un caràcter força rellevant.

Bibliography

[1] The writing of this chapter is based upon the information contained in *Operator's Handbook* and *Practical Cryogenics*, Oxford Instruments (2006).

[2] Alberto Hernández Mínguez, *Avalanchas en sistemas de espines: deflagración magnética cuántica y nueva ley de relajación*, Ph. D. Thesis, Universitat de Barcelona (2009).

[3] J. R. Friedman, M. P. Sarachik, J. Tejada, and R. Ziolo, Phys. Rev. Lett. **76**, 3830 (1996).

[4] J. M. Hernandez, X. X. Zhang, F. Luis, J. Bartolome, J. Tejada, and R. Ziolo, Europhys. Lett. **35**, 301 (1996).

[5] J. Tejada, E. M. Chudnovsky, E. del Barco, J. M. Hernandez, and T. P. Spiller, Nanotechnology **12**, 181 (2001).

[6] M. N. Leuenberger and D. Loss, Nature **410**, 789 (2001).

[7] T. Lis, Acta Cryst. B **36**, 2042 (1980).

[8] S. Hill, J. A. A. J. Perenboom, N. S. Dalal, T. Hathaway, T. Stalcup, and J. S. Brooks, Phys. Rev. **80**, 2453 (1998).

[9] I. Mirebeau, M. Hennion, H. Casalta, H. Andres, H. U. Güdel, A. V. Irodova, and A. Caneschi, Phys. Rev. **83**, 628 (1999).

[10] C. Paulsen and J. G. Park, pp. 189-207 in *Quantum Tunneling of Magnetization - QTM'94*, Edited by L. Gunther and B. Barbara (Kluwer, Dordrecht, Netherlands, 1995)

[11] E. del Barco, J. M. Hernandez, M. Sales, J. Tejada, H. Rakoto, J. M. Broto, and E.M. Chudnovsky, Phys. Rev. B **60**, 11898 (1999).

[12] A. Hernández-Mínguez, M. Jordi, R. Amigó, A. García-Santiago, J. M. Hernandez, and J. Tejada, Europhys. Lett. **69**, 270 (2005).

[13] Y. Suzuki, M.P. Sarachik, E. M. Chudnovsky, S. McHugh, R. Gonzalez-Rubio, N. Avraham, Y. Myasoedov, E. Zeldov, H. Shtrikman, N. E. Chakov, and G. Christou, Phys. Rev. Lett. **95**, 147201 (2005).

[14] A. Hernández-Mínguez, J. M. Hernandez, F. Macià, A. García-Santiago, J. Tejada, and P. V. Santos, Phys. Rev. Lett. **95**, 217205 (2005).

[15] D. A. Garanin and E. M. Chudnovsky, Phys. Rev. B **76**, 054410, (2007).

[16] A. Hernández-Mínguez, F. Macià, J. M. Hernandez, J. Tejada, P. V. Santos, J. Magn. & Magn. Mat. **320**, 1457 (2008)

[17] A. Hernández-Mínguez, F. Macià, J. M. Hernandez, J. Tejada, and L. H. He, F. F. Wang, Europhys. Lett. **75**, 811 (2006)

[18] J. M. Hernandez, X. X. Zhang, F. Luis, J. Tejada, Jonathan R. Friedman, M. P. Sarachik, and R. Ziolo, Phys. Rev. B. **55**, 91 (1997)

[19] Alessandra Satta, *Growth mechanism and properties of atomic layer deposited ultra-thin films*, Ph. D. Thesis, Katholieke Universiteit Leuven (2003).

[20] *CRC Handbook of Chemistry and Physics*, 91th edition (2010-2011).

[21] T. G. Dziura, B. Bunday, C. Smith, M. M. Hussain, R. Harris, X. Zhang and J. M. Price, Proc. SPIE 6922, 69220V (2008)

[22] M. Birkholz, K.-E. Ehwald, D. Wolansky, I. Costina, C. Baristyran-Kaynak, M. Fröhlich, H. Beyer, A. Kapp and F. Lisdat, Surf. Coat. Technol. **204**, 2055-2059. (2010).

[23] H. Hämmerle, K. Kobuch, K. Kohler, W. Nisch, H. Sachs and M. Stelzle, Biomat. **23**, 797-804. (2002).

[24] M. Birkholz, K. E. Ehwald, P. Kulse, J. Drews, M. Fröhlich, U. Haak, M. Kaynak, E. Matthus, K. Schulz and D. Wolansky, Adv. Func. Mat. **21**, 1652-1656 (2011).

[25] *Newly discovered 'superinsulators' promise to transform materials research, electronics design.* PhysOrg.com. 2008-04-07.

[26] J. C. Hu, T. C. Chang, L. J. Chen, Y. L. Yang, and C. Y. Chang, Thin Solid Films **332**, 423-427 (1998).

[27] C. Faltermeier et al., J. Electrochem. Soc. **144**, 1002-1008 (1997).

[28] D. H. Kim, J. J. Kim, J. W. Park, and J. J. Kim, J. Electrochem. Soc. **143**, 188-190 (1996).

[29] S. H. Kim, D. S. Chung, K. C. Park, K. B. Kim, and S. H. Min, J. Electrochem. Soc. **146**, 1455-1460 (1999).

[30] R. Tobe, A. Sekiguchi, M. Sasaki, O. Okada, and N. Hosokawa, Thin Solid Films **281-282**, 155-158 (1996).

[31] T. Suntola, Thin Solid Films **216**, 84-89 (1992)

[32] S. Yokoyama, H. Goto, T. Miyamoto, N. Ikeda, and K. Shibahara, Appl. Surf. Sci. **112**, 75-81 (1997).

[33] A. Usui, Thin Solid Films **225**, 53-58 (1993).

[34] M. Ritala and M. Leskela, *Handbook of Thin Film Materials*, Vol. 1, edited by H. S. Nalwa, Academic Press, San Diego, California, 103-159 (2002).

[35] T. Suntola, *Handbook of Crystal Growth*, Vol. 3, edited by D. T. J. Hurle, Elsevier, Amsterdam, 601-663 (1994).

[36] T.I. Baturina, D. R. Islamov, J. Bentner, C. Strunk, M. R. Baklanov and A. Satta, JETP Lett. **79** 337 (2004).

[37] M. A. McCord and M. J. Rooks, *Handbook of Microlithography, Micromachining and Microfabrication* Volume 1, edited by P. Rai-Choudhury, Cornell NanoScale Science & Technology Facility (CNF), Cornell University, Ithaca, New York (2000).

[38] M. Ohring, *Materials Science of Thin Films*, Academic Press, San Diego, California (2002).

[39] E. S. Machlin, *Materials Science in Microelectronics. The relationships between thin film processing and structure*, Vol. 1, 2nd edition, Elsevier, Amsterdam (2005).

[40] T.I. Baturina, J. Bentnerb, C. Strunk, M.R. Baklanov and A. Satta, Physica B **359-361**, 500-502 (2005).

[41] A.C. Rose-Innes and E.H. Rhoderick, *Introduction to Superconductivity*, University of Manchester Institute of Science & Technology, Pergamon Press (1978).

[42] J. Bardeen, L. N. Cooper and J. R. Schrieffer, Phys. Rev. **108**, 1175-1204 (1957).

[43] V. Vinokur, T. Baturina, M. Fistul, A. Y. Mironov, M. Baklanov and C. Strunk, Nature **452**, 613 (2008).

[44] D. Kowal, and Z. Ovadyahu, **90**, 783-786 (1994).

[45] V. F. Gantmakher, M. V. Golubkov, J. G. S. Lok and A. K. Geim, JETP **82**, 951-958 (1996).

[46] T. I. Baturina, A. Yu. Mironov, V. M. Vinokur, M. R. Baklanov and C. Strunk, Phys. Rev. Lett. **99**, 257003 (2007).

[47] M. V. Fistul, V. M. Vinokur and T. I. Baturina, Phys. Rev. Lett. **100**, 086805 (2008).

[48] M. R. Beasley, J. E. Mooij and T. P. Orlando, Phys. Rev. Lett., **42**, 1165 (1979).

[49] B. I. Halperin and D. R. Nelson, J. Low Temp. Phys., **36** 599 (1979).

[50] V.S. Berezinskii, JETP **34**, 610 (1972).

[51] J.M. Kosterlitz and P.J. Thouless, Journal of Physics, **6**, 1181 (1973).

[52] P. Minnhagen, Rev. of Mod. Phys., **59**, 100, (1987).

[53] P. Minnhagen, *In Fluctuation phenomena in high temperature superconductors*, (ed. M.Ausloos and A.A.Varlamov), NATO-ASI Series, Kluwer, Dordrecht. (1997).

[54] A. Larkin and A. Varlamov, *Theory of fluctuations in superconductors*, Oxford University Press, Oxford (2005).

[55] T. I. Baturina, S. V. Postolova, A. Yu. Mironov, A. Glatz, M. R. Baklanov and V. M. Vinokur, EPL, **97** 17012 (2012).

[56] Minnhagen P., Phys. Rev. B, **23**, 5745, (1981).

[57] K. Epstein, A. M. Goldman and A. M. Kadin, Phys. Rev. Lett., **47**, 534, (1981).

[58] S. A. Wolf, D. U. Gubser, W. W. Fuller, J. C. Garland and R. S. Newrock, Phys. Rev. Lett., **47**, 1071, (1981).

[59] A. M. Kadin, K. Epstein and A. M. Goldman, Phys. Rev. B, **27**, 6691, (1983).

[60] A. F. Hebard and A. T. Fiory, Phys. Rev. Lett., **50**, 1603, (1983).

[61] A. T. Fiory, A. F. Hebard and W. I. Glaberson, Phys. Rev. B, **28**, 5075, (1983).

[62] A. F. Hebard and M. A. Paalanen, Phys. Rev. Lett., **54**, 2155, (1985) .

[63] R. W. Simon, B. J. Dalrymple, D. Van Vechten, W. W. Fuller, and S. A. Wolf, Phys. Rev. B, **36**, 1962, (1987).

[64] J. S. Langer and T. Neal, Phys. Rev. Lett., **16**, 984 (1966).

[65] L. G. Aslamasov and A. I. Larkin, Phys. Lett. A, **26**, 238 (1968).

[66] M. Strongin, O. F. Kammerer, J. Crow, R. S. Thompson and H. L. Fine, Phys. Rev. Lett., **20**, 922 (1968).

[67] K. Maki, Prog. Theor. Phys., **39**, 897, (1968).

[68] R. S. Thompson, Phys. Rev. B, **1**, 327, (1970).

[69] L. P. Gorkov, A. I. Larkin and D. E. Khmelnitskii, JETP Lett., **30**, 228, (1979).

[70] L. G. Aslamasov and A. A. Varlamov, J. Low Temp. Phys., **38**, 223, (1980).

[71] A. I. Larkin, JETP Lett., **31**, 219, (1980).

[72] B. L. Altshuler, A. G. Aronov and P. A. Lee, Phys. Rev. Lett., **44**, 1288, (1980).

[73] B. L. Altshuler and A. G. Aronov, *Electron-Electron Interactions in Disordered Systems*, edited by Efros A. L. and Pollak M. (North-Holland, Amsterdam) 1985.

[74] K. v. Klitzing, G. Dorda and M. Pepper, Phys. Rev. Lett., **45**, 494 (1980).

[75] A. Glatz, A. A. Varlamov and V. M. Vinokur, EPL, **94**, 47005, (2011); Phys. Rev. B, **84**, 104510, (2011).

[76] Y. Bruynseraede, M. Gijs, C. Van Haesendonck and G. Deutscher, Phys. Rev. Lett., **50**, 277 (1983).

[77] M. E. Gershenzon, V. N. Gubankov and Yu. E. Zhuravlev, JETP, **58**, 167 (1983).

[78] H. Raffy, R. B. Laibowitz, P. Chaudhari, and S. Maekawa, Phys. Rev. B, **28**, 6607, (1983).

[79] P. Santhanam and D. E. Prober, Phys. Rev. B, **29**, 3733, (1984).

[80] G. Bergmann, Phys. Rev. B, **29**, 6114, (1984).

[81] J. M. Gordon, C. J. Lobb and M. Tinkham, Phys. Rev. B, **29**, 5232, (1984).

[82] J. M. Gordon and A. M. Goldman, Phys. Rev. B, **34**, 1500, (1986).

[83] W. Brenig, M. A. Paalanen, P. Wölfle and A. F. Hebard, Phys. Rev. B, **33**, 1691, (1986).

[84] C. Y. Wu and J. J. Lin, Phys. Rev. B, **50**, 385, (1994).

[85] Z. D. Kvon, T. I. Baturina, R. A. Donaton, M. R. Baklanova, M. N. Kostrikin, K. Maex, E. B. Olshanetsky, J. C. Portal, Physica B, **284-288**, 959 (2000).

[86] M. P. A. Fisher and D. H. Lee, Phys. Rev. B **39**, 2756 (1989).

[87] M. P. A. Fisher, G. Grinstein, and S. M. Girvin, Phys. Rev. Lett. **64**, 587 (1990).

[88] M. P. A. Fisher, Phys. Rev. Lett. **65**, 923 (1990).

[89] S. L. Sondhi, S. M. Girvin, J. P. Carini, and D. Shahar, Rev. Mod. Phys. **69**, 315 (1997).

[90] E. L. Shangina and V. T. Dolgopolov, Phys. Usp. **46**, 777 (2003).

[91] D. B. Haviland, Y. Liu, and A. M. Goldman, Phys. Rev. Lett. **62**, 2180 (1989).

[92] Y. Liu, D. B. Haviland, B. Nease, and A. M. Goldman, Phys. Rev. B **47**, 5931 (1993).

[93] A. F. Hebard and M. A. Paalanen, Phys. Rev. Lett. **65**, 927 (1990).

[94] G. Sambandamurthy, L. W. Engel, A. Johansson, and D. Shahar, Phys. Rev. Lett. **92**, 107005 (2004).

[95] V. F. Gantmakher, M. V. Golubkov, V. T. Dolgopolov, G. E. Tsydynzhapov, and A.A. Shashkin, JETP Lett. **68**, 363 (1998).

[96] N. Marcovic, C. Christiansen, A. M. Mack, W. H. Huber, and A. M. Goldman, Phys. Rev. B **60**, 4320 (1999).

[97] A. Yazdani and A. Kapitulnik, Phys. Rev. Lett. **74**, 3037 (1995).

[98] S. Okuma, T. Terashima, and N. Kokubo, Solid State Communications **106**, 529 (1998); S. Okuma, T. Terashima, and N. Kokubo, Phys. Rev. B **58**, 2816 (1998).

[99] V.F. Gantmakher, M.V. Golubkov, V.T. Dolgopolov, G.E. Tsydynzhapov, A.A. Shashkin, JETP Lett. **71**, 473 (2000).

[100] V. F. Gantmakher, S. N. Ermolov, G. E. Tsydynzhapov, A. A. Zhukov, T. I. Baturina, JETP Lett. **77**, 424 (2003).

[101] V. M. Galitski and A. I. Larkin, Phys. Rev. B **63**, 174506 (2001).

[102] S. Tanda, S. Ohzeki, and T. Nakayama, Phys. Rev. Lett. **69**, 530 (1992).

[103] M. V. Golubkov and G. E. Tsydynzhapov, JETP Letters, **71**, 516-519, (2000).

[104] M. Ovadia, B. Sacépé, and D. Shahar, Phys. Rev. Lett. **102**, 176802 (2009).

[105] Boris L. Altshuler, Vladimir E. Kravtsov, Igor V. Lerner, and Igor L. Aleiner, Phys. Rev. Lett. **102**, 176803 (2009).

[106] G. Sambandamurthy, L. Engel, A. Johansson, E. Peled, and D. Shahar, Phys. Rev. Lett. **94**, 017003 (2005).

[107] M. Roukes, M. Freeman, R. Germain, and R. Richardson, Phys. Rev. Lett. **55**, 422 (1985).

[108] M. Gershenson, D. Gong, T. Sato, B. Karasik, and A. Sergeev, Appl. Phys. Lett. **79**, 2049 (2001).

[109] K. A. Parendo, K. H. S. B. Tan, and A. M. Goldman, Phys. Rev. B **74**, 134517 (2006).

[110] A. F. Volkov and S. M. Kogan, Sov. Phys. Usp. **11**, 881 (1969).

[111] M. E. Gershenson et al., Phys. Rev. Lett. **85**, 1718 (2000).

[112] B. I. Shklovskii and A. L. Efros, *Electronic Properties of Doped Semiconductors* (Springer, Heidelberg, 1984).

[113] D. Kimhi, F. Leyvraz, and D. Airosa, Phys. Rev. B **29**, 1487 (1984).

[114] H.S.J. Van der Zant, M.N. Webster, J. Romijin, and J.E. Mooiji, Phys. Rev. B **50**, 340 (1994).

[115] T.I. Baturina, Tu. A. Tsaplin, A.E. Plotnikov and M.R. Baklamov, Physica B **378-380**, 1058 (2006).

[116] T. I. Baturina, D.W. Horsell, D. R. Islamov, I. V. Drebushchak, Yu. A. Tsaplin, A. A. Babenko, Z. D. Kvon, A. K. Savchenko and A. E. Plotnikov, Physica B **329**, 1496 (2003).

[117] M. Tinkham, D. W. Abraham, and C. J. Lobb, Phys. Rev. B **28**, 6578 (1983).

[118] M. Strongin, R. S. Thompson, O. F. Kammerer and J. E. Crow, Phys. Rev. B, **1**, 1078 (1970).

[119] A. M. Goldman and N. Marković, Phys. Today, **51**, issue No. 11, 39 (1998).

[120] E. Bielejec, J. Ruan and W. Wu, Phys. Rev. Lett., **87**, 036801 (2001).

[121] N. Hadacek, M. Sanquer and J.C. Villégier, Phys. Rev. B, **69**, 024505 (2004).

[122] Y. Qin, C. L. Vicente and J. Yoon, Phys. Rev. B, **73**, 100505(R) (2006).

[123] S. Maekawa and H. Fukuyama, J. Phys. Soc. Jpn., **51**, 1380 (1982).

[124] A. M. Finkelstein, JETP Lett., **45**, 46 (1987); Physica B, **197**, 636 (1994).

[125] T. Yamaguchi, R. Yagi, S. Kobayashi and Y. Ootuka, J. Phys. Soc. Jpn., **67**, 729 (1998).

[126] Z. Jiang, D. A. Dikin, V. V. Metlushko, V. V. Moshchalkov, and V. Chandrasekhar, Appl. Phys. Lett. **84**, 5371 (2004).

[127] A. D. Thakur, S. Ooi, S. P. Chockalingam, J. Jesudasan, P. Raychaudhuri, K. Hirata, Appl. Phys. Lett. **94**, 262501 (2009).

[128] T. I. Baturina, V. M. Vinokur, A. Yu. Mironov, N. M. Chtchelkatchev, D. A. Nasimov and A. V. Latyshev, EPL, **93**, 47002 (2011).

[129] B. Pannetier, J.Chaussy, R. Rammal and J. C. Villegier, Phys. Rev. Lett., **53**, 1845 (1984).

[130] R. S. Newrock, C. J. Lobb, U. Geigenmuller, and M. Octavio, Solid State Physics **54**, 263 (2000).

[131] L. Van Look, B. Y. Zhu, R. Jonckheere, B. R. Zhao, Z. X. Zhao, V. V. Moshchalkov, Phys. Rev. B, **66**, 214511 (2002).

[132] A. T. Fiory, A. F. Hebard and S. Somekh, Appl. Phys. Lett., **32**, 73 (1978).

[133] A. Hoffmann, P. Prieto and I. K. Schuller, Phys. Rev. B, **61**, 6958(R) (2000).

[134] U. Patel, Z. L. Xiao, J. Hua, T. Xu, D. Rosenmann, V. Novosad, J. Pearson, U. Welp, W. K. Kwok, G. W. Crabtree, Phys. Rev. B, **76**, 020508(R) (2007).

[135] S. Avci, Z. L. Xiao, J. Hua, A. Imre, R. Divan, J. Pearson, U. Welp, W. K. Kwok, and G. W. Crabtree., Appl. Phys. Lett., **97**, 042511 (2010).

[136] H. Q. Nguyen, S. M. Hollen, M. D. Stewart, Jr., J. Shainline, A. Yin, J. Xu, and J. M. Valles, Phys. Rev. Lett., **103**, 157001 (2009).

[137] S. Ooi, T. Mochiku, S. Yu, E. S. Sadki, and K. Hirata, Physica C, **426**, 113 (2005).

[138] T. I. Baturina, A. Yu. Mironov, V. M. Vinokur, N. M. Chtchelkatchev, A. Glatz, D. A. Nasimov and A. V. Latyshev, Physica C **470**, S810-S812 (2010).

[139] I. Sochnikov, A. Shaulov, Y. Yeshurun, G. Logvenov, and I. Bozović, Nat. Nanotechnol., **5**, 516 (2010); Phys. Rev. B, **82**, 094513 (2010).

[140] K. K. Likharev, Rev. Mod. Phys., **51**, 101, (1979).

[141] C. J. Lobb, D. W. Abraham and M. Tinkham, Phys. Rev. B, **27**, 150 (1983).

[142] A. Larkin, Ann. Phys., **8**, 785 (1999).

[143] A. Andreev, JETP **19**, 1228, (1964).

[144] G. E. Blonder, M. Tinkham, and T. M. Klapwijk, Phys. Rev. B **25**, 4515 (1982).

[145] A. V. Lopatin and V. M. Vinokur, Phys. Rev. B **75**, 092201 (2007).

[146] A. Widom and S. Badjou, Phys. Rev. B **37**, 7915 (1988).

[147] J. E. Mooij, B. J. van Wees, L. J. Geerligs, M. Peters, R. Fazio, and G. Schön , Phys. Rev. Lett. **65**, 645 (1990).

[148] T. I. Baturina, A. Bilusic, A. Yu. Mironov, V. M. Vinokur, M. R. Baklanov, and C. Strunk, Physica C **468**, 316 (2008).

[149] T. I. Baturina, Yu. A . Tsaplin, A. E. Plotnikov, and M. R. Baklanov, JETP Lett. **88**, 752 (2008).

[150] B. Sacépé, C. Chapelier, T. I. Baturina, V. M. Vinokur, M. R. Baklanov, and M. Sanquer, Phys. Rev. Lett. **101**, 157006 (2008).

[151] N. F. Mott and E. A. Davis, Philos. Mag. **17**, 1269 (1968).

[152] V. E. Dubrov, M. E. Levinshtein and M. S. Shur, JETP **43**, 1050 (1976).

[153] B. Pannetier and H. Courtois, J. Low Temp. Phys. **118**, 599 (2000).

[154] W. M. van Huffelen, T. M. Klapwijk, D. R. Heslinga, M. J. de Boer and N. Van der Post, Phys. Rev. B **47**, 5170 (1993).

[155] H. Courtois, Ph. Gandit, D. Mailly and B. Pannetier, Phys. Rev. Lett. **76**, 130 (1996).

[156] P. Charlat, H. Courtois, Ph. Gandit, D. Mailly, A. F. Volkov and B. Pannetier, Phys. Rev. Lett. **77**, 4950 (1996).

[157] J. Kutchinsky, R. Taboryski, T. Clausen, C. B. Sorensen, A. Kristensen, P. E. Lindelof, J. Bindslev Hansen, C. Schelde Jacobsen and J. L. Skov, Phys. Rev. Lett. **78**, 931 (1997).

[158] A. Frydman and R. C. Dynes, Phys. Rev. B **59**, 8432 (1999).

[159] T. Hoss, C. Strunk, T. Nussbaumer, R. Huber, U. Staufer, and C. Schönenberger, Phys. Rev. B **62**, 4079 (2000).

[160] T. I. Baturina, Z . D. Kvon, R. A. Donaton, M. R. Baklanov, E. B. Olshanetsky, K. Maex, A. E. Plotnikov and J. C. Portal, Physica B **284**, 1860 (2000).

[161] Z. D. Kvon, T. I. Baturina, R. A. Donaton, M. R. Baklanov, K. Maex, E. B. Olshanetsky, A. E. Plotnikov and J. C. Portal, Phys. Rev. B **61**, 11340 (2000).

[162] M. Octavio, M. Tinkham, G.E. Blonder and T.M. Klapwijk, Phys. Rev. B **27**, 6739 (1983).

[163] K. Flensberg, J. Bindslev Hansen and M. Octavio, Phys. Rev. B **38**, 8707 (1988).

[164] E. V. Bezuglyi, E. N. Bratus, V. S. Shumeiko, G. Wendin and H. Takayanagi, Phys. Rev. B **62**, 14439 (2000).

[165] T. I. Baturina, Z. D. Kvon, and A. E. Plotnikov, Phys. Rev. B **63**, 180503(R) (2001).

[166] T. I. Baturina, D. R. Islamov, and Z. D. Kvon, JETP Lett. **75**, 326 (2002).

[167] T. I. Baturina, Yu. A. Tsaplin, A. E. Plotnikov and M. R. Baklanov, JETP Lett. **81**, 10 (2005).

[168] N.M. Chtchelkatchev, JETP Lett. **83**, 250 (2005).

[169] T. I. Baturina, J. Bentner, C. Strunk, M. R. Baklanov, and A. Satta, Physica B **359**, 500 (2005).